

Advances in Meteorology

Earth Observations and Societal Impacts 2015

Guest Editors: Yuei-An Liou, Chung-Ru Ho, Yuriy Kuleshov,
and Jean-Pierre Barriot





Earth Observations and Societal Impacts 2015

Advances in Meteorology

Earth Observations and Societal Impacts 2015

Guest Editors: Yuei-An Liou, Chung-Ru Ho, Yuriy Kuleshov,
and Jean-Pierre Barriot



Copyright © 2016 Hindawi Publishing Corporation. All rights reserved.

This is a special issue published in "Advances in Meteorology." All articles are open access articles distributed under the Creative Commons Attribution License, which permits unrestricted use, distribution, and reproduction in any medium, provided the original work is properly cited.

Editorial Board

J. Antonio Adame, Spain
Cesar Azorin-Molina, Spain
Guillermo Baigorria, USA
Marina Baldi, Italy
Abderrahim Bentamy, France
Massimo A. Bollasina, UK
Stefania Bonafoni, Italy
Isabella Bordi, Italy
Alex Cannon, Canada
Claudio Carbone, Italy
Dominique Carrer, France
Charles Chemel, UK
Annalisa Cherchi, Italy
James Cleverly, Australia
Jill S. M. Coleman, USA
Gabriele Curci, Italy
M. Ćurić, Serbia
Maher A. Dayeh, USA
Klaus Dethloff, Germany
P. C. S. Devara, India
Julio Diaz, Spain
Arona Diedhiou, France
Stefano Dietrich, Italy
Eugenio D. Vilches, Spain
Antonio Donateo, Italy
Igor Esau, Norway
Stefano Federico, Italy
Enrico Ferrero, Italy
Rossella Ferretti, Italy
Roberto Fraile, Spain
Charmaine Franklin, Australia
Jan Friesen, Germany

M. Ángeles García, Spain
H. García Mozo, Spain
E. García-Ortega, Spain
Luis Gimeno, Spain
Jorge E. Gonzalez, USA
Ismail Gultepe, Canada
Rafiq Hamdi, Belgium
Adel Hanna, USA
Hiroyuki Hashiguchi, Japan
Tareq Hussein, Jordan
Bradley G. Illston, USA
Ivar S A Isaksen, Norway
Yasunobu Iwasaka, Japan
P. Jiménez-Guerrero, Spain
Kuruvilla John, USA
Charles Jones, USA
Hann-Ming H. Juang, USA
George Kallos, Greece
Harry D. Kambezidis, Greece
Nir Y. Krakauer, USA
Simon O. Krichak, Israel
Hisayuki Kubota, Japan
Haim Kutiel, Israel
Richard Leaitch, Canada
Monique Leclerc, USA
Ilan Levy, Israel
Gwo-Fong Lin, Taiwan
Anthony R. Lupo, USA
Paolo Madonia, Italy
A. Matzarakis, Germany
Samantha Melani, Italy
Nicholas Meskhidze, USA

Christophe Messenger, France
Mario M. Miglietta, Italy
Takashi Mochizuki, Japan
Goro Mouri, Japan
Brian R. Nelson, USA
E. I. Nikolopoulos, USA
Sandip Pal, USA
Giulia Panegrossi, Italy
Giulia Pavese, Italy
Kyaw T. Paw, USA
Olivier P. Prat, USA
Sara C. Pryor, USA
Philippe Ricaud, France
Tomeu Rigo, Spain
Filomena Romano, Italy
Jose A. Ruiz-Arias, Spain
Haydee Salmun, USA
Pedro Salvador, Spain
A. Sanchez-Lorenzo, Spain
Andres Schmidt, USA
Shraddhanand Shukla, USA
Fiona Smith, UK
Francisco J. Tapiador, Spain
Yoshihiro Tomikawa, Japan
Tomoo Ushio, Japan
R. Van Der Velde, Netherlands
S. M. Vicente-Serrano, Spain
Francesco Viola, Italy
Alastair Williams, Australia
Olga Zolina, France

Contents

Earth Observations and Societal Impacts 2015

Yuei-An Liou, Chung-Ru Ho, Yuriy Kuleshov, and Jean-Pierre Barriot
Volume 2016, Article ID 8517659, 3 pages

Time-Series Mapping of PM₁₀ Concentration Using Multi-Gaussian Space-Time Kriging: A Case Study in the Seoul Metropolitan Area, Korea

No-Wook Park
Volume 2016, Article ID 9452080, 10 pages

Association of Taiwan's Rainfall Patterns with Large-Scale Oceanic and Atmospheric Phenomena

Yi-Chun Kuo, Ming-An Lee, and Mong-Ming Lu
Volume 2016, Article ID 3102895, 11 pages

Analysis of Long-Term Meteorological Observation for Weather and Climate Fundamental Data over the Northern Tibetan Plateau

Fangfang Huang and Weiqiang Ma
Volume 2016, Article ID 4878353, 10 pages

Distribution of Atmospheric Aerosol over the South China Sea

Shih-Jen Huang and Chen-Chih Lin
Volume 2015, Article ID 692762, 7 pages

Impacts of Two-Type ENSO on Rainfall over Taiwan

Chen-Chih Lin, Yi-Jiun Liou, and Shih-Jen Huang
Volume 2015, Article ID 658347, 7 pages

Editorial

Earth Observations and Societal Impacts 2015

Yuei-An Liou,^{1,2} Chung-Ru Ho,^{2,3} Yuriy Kuleshov,⁴ and Jean-Pierre Barriot⁵

¹Center for Space and Remote Sensing Research (CSRSR), National Central University, Chungli 32001, Taiwan

²Taiwan Group on Earth Observations, Zhubei 30274, Taiwan

³Department of Marine Environmental Informatics, National Taiwan Ocean University, Keelung 20224, Taiwan

⁴Bureau of Meteorology, GPO Box 1289, Melbourne, VIC 3001, Australia

⁵Geodesy Observatory of Tahiti, University of French Polynesia, BP 6570, 98702 Faaa, Tahiti, French Polynesia

Correspondence should be addressed to Yuei-An Liou; yueian@csrsr.ncu.edu.tw

Received 25 August 2015; Accepted 26 August 2015

Copyright © 2016 Yuei-An Liou et al. This is an open access article distributed under the Creative Commons Attribution License, which permits unrestricted use, distribution, and reproduction in any medium, provided the original work is properly cited.

“Study links polluted air in China to 1.6 million deaths a year,” what a shocking news as reported by Dan Levin of The New York Times on August 13, 2015. The news was started with the fact that “outdoor air pollution contributes to the deaths of an estimated 1.6 million people in China every year, or about 4,400 people a day, according to a newly released scientific paper” (<http://nyti.ms/1TxzQD0>). Air pollution is an issue of global concern, not only because of impact on the health of the human beings, but also due to contribution to the climate change. However, some questions remain unanswered in the news report. The cited “a newly released scientific paper” is indeed a draft of a paper and has not yet passed the peer review of a journal. It was found that the number of the deaths was based on a theoretical calculation. Then, it raises a question, is the theoretically estimated number of deaths correct? The question can be answered by earth observation (EO), which has been recognized to play a vital role in the sustainable development of the globe. “EO involves the very close investigation and measurement on the Earth and the derived results from the direct or indirect observations and measurements are the crucial information used to construct the supporting policies for the environments, post-disaster managements, etc.” [1–5].

The International Conference on Earth Observations and Societal Impacts (ICEO&SI; <http://www.iceo-si.org.tw/>), hosted by Taiwan Group on Earth Observations (<http://tgeo.org.tw/>) in partnership with other academic institutions, provides a forum for international experts and scholars specialized in earth observations and social science to discuss

and communicate the topic of climate change, environmental disasters, and ecological impacts in order to bring up appropriate suggestions and corresponding strategies of human being. More than 200 papers were presented in the ICEO&SI 2014 and 2015. Five of them are turned into this special issue as one of the academic fruits and ordered according to topic: air pollution/aerosol, global warming, and global change. The main scientific findings are briefly introduced below.

The South China Sea, the largest marginal sea of the Pacific in Southeast Asia, is abundant with marine resources. A vast amount of aerosol, attributed to varied emissions (e.g., dust, anthropogenic, and biomass burning) from the Asian continent, has widely impacted on the ecosystem of the sea. Spatial and temporal analysis of distribution of atmospheric aerosol over the South China Sea has been investigated. Specifically, the satellite-derived aerosol optical depth data were used to investigate the distribution of coarse aerosol (e.g., dust or ocean spray) and fine aerosol (e.g., biomass burning or anthropogenic pollution) over the study area. Variation of coarse aerosol particles as derived from satellite remote sensing data was in agreement with *in situ* observations, with the high value occurring in spring. In addition, China and the Indo-China Peninsula are the probable source regions of coarse aerosol particles. Furthermore, temporal amplitudes of coarse aerosol particles modes show that the average amplitude during La Niña events is larger. The significant EOF modes of fine aerosol particles refer to the fact that the high value occurs annually and semiannually. The spatial distribution of each mode and other studies also

evidence the fact that the biomass burning, respectively, occurs in the Indo-China Peninsula during March and April, but from August to October in Sumatra and Borneo. The results also show that average amplitude of fine aerosol particles is larger during El Niño events.

Outdoor air pollution has been known as one of the risk factors that affect human health. PM_{10} , particulate matter less than $10\ \mu\text{m}$ in aerodynamic diameter, is one of the indicators to evaluate the air pollution. The authors used a geostatistical multi-Gaussian Kriging method for time-series mapping of PM_{10} concentrations. This method was applied to a case study in Seoul, Korea. The result indicates that the developing method is useful for interpretation of air pollution and can be used for decision-making. However, to enhance the major findings of this study, two issues should be addressed in future work. First, several auxiliary variables such as the proximity to major roads and weather data should be integrated within the framework of this study. This may generate more reliable PM_{10} concentration mapping results. Second, the multi-Gaussian approach may not be appropriate for datasets with a strong positively skewed distribution, which is often observed in air pollutant concentrations. Thus, the extension of the conventional spatial indicator approach to the space-time domain and the comparison with the multi-Gaussian approach should be included in future work.

One of the major issues of today's research on global warming is how (and when) the pattern of ocean circulation will evolve, with even catastrophic scenario of major changes in the near future. Global markers of this climate evolution are particularly useful, as local markers are often confusing or unreliable. The authors demonstrate in this special issue that the study of the evolution of rainfall is a reliable proxy at large temporal and spatial scales to follow this evolution. From 50 years of homogenised rainfall data (1960–2009) over the island of Taiwan, they are able to separate the spatial (topography induced) and temporal (atmosphere/ocean) forcing. By using Empirical Orthogonal Functions (EOF), they identify the signatures of the monsoon and ENSO events, and they demonstrate that the climate variability associated with ENSO is distinct from the climate variability over other regions of East Asia. They finally isolate in the rainfall data a north-south pattern approximately in phase with the Pacific Decadal Oscillation.

From climatological perspective the year 2015 is significant in terms of the development of a strong El Niño event. To describe the oscillation between the El Niño (warm) phase and the La Niña (cold) phase, the El Niño Southern Oscillation (ENSO) term is used. El Niño and La Niña events lead to a major shift in weather patterns across the Pacific and as a consequence often produce significant impacts on population, economy, and so forth. The impacts vary for different geographical regions. The 2015 El Niño event is already significant, and further strengthening of El Niño conditions later this year remains a possibility as indicated by climate models. Not surprisingly, numerous studies of ENSO impacts in different geographical regions have been conducted, highlighting importance of research efforts in

improving our understanding of ENSO and its variability. In this issue, impact of two types of ENSO, canonical ENSO and ENSO Modoki, on rainfall over Taiwan has been investigated, based on analysis of monthly mean rainfall data obtained from the Taiwan Central Weather Bureau. Correlations between rainfall data and values of Niño 3.4 and ENSO Modoki index are established and it is shown that the seasonal rainfall over various regions of Taiwan is different depending on the effects of two-type ENSO. In canonical El Niño episode, the rainfall increases in winter and spring while it reduces in summer and autumn. On the contrary, the rainfall increases in summer and autumn but reduces in winter and spring in El Niño Modoki episode. The rainfall variations in different types of ENSO are mainly caused by the monsoon and topography.

Climate change is a topic of interest for the scientific communities. Tibetan Plateau is one of the highest plateaus in the world. It plays an important role in East Asian and global climate because of its high elevation and complex surface conditions. Using the field stations at the Tibetan Plateau, the authors found that the diurnal variations of land surface temperature and air temperature are various in different seasons underlying surfaces. The diurnal variation is greater in spring but less in summer and autumn. Furthermore, the diurnal variation in the area with drier underlying surface is more obvious than that with moist surface. The variations of land surface temperature, air temperature, wind speed, and soil moisture are also related to ENSO events. The values of land surface temperature, air temperature, and wind speed are lower than the mean values, but the soil moisture values are greater than the averaged value in La Niña year, while they are converse in El Niño year. Besides the influence of ENSO events, the warming rate at the northern Tibetan Plateau is greater than that in the global areas.

In this special issue, the most recent developments and ideas in air pollution/aerosol, climate variability and change, and their impacts on different regions in the Asia-Pacific are presented. For scientists, engineers, and various end users of remote sensing and climate data as well as related products (including those derived using GIS), findings of the studies presented here could serve as valuable references. In context of providing solid solutions for the societal needs, our continuous efforts in delivering new scientific results in earth observations contribute to addressing various environmental issues and developing effective climate change adaptation strategies.

Acknowledgments

We are grateful to all the authors who contributed to this issue and to all the reviewers whose suggestions have helped improve the quality of the papers published in this issue.

*Yuei-An Liou
Chung-Ru Ho
Yuriy Kuleshov
Jean-Pierre Barriot*

References

- [1] S. K. Kar, Y. A. Liou, and K. J. Ha, “Aerosol effects on the enhancement of cloud-to-ground lightning over major urban areas of South Korea,” *Atmospheric Research*, vol. 92, no. 1, pp. 80–87, 2009.
- [2] Y. A. Liou, S. K. Kar, and L. Y. Chang, “Use of high-resolution formosat-2 satellite images for post-earthquake disaster assessment: a study following the 12 May 2008 Wenchuan earthquake,” *International Journal of Remote Sensing*, vol. 31, no. 13, pp. 3355–3368, 2010.
- [3] Y. A. Liou, H. C. Sha, T. M. Chen et al., “Assessment of disaster losses in rice paddy field and yield after tsunami induced by the 2011 Great East Japan earthquake,” *Journal of Marine Science and Technology*, vol. 20, no. 6, pp. 618–623, 2012.
- [4] F. C. Ming, C. Ibrahim, C. Barthe et al., “Observation and a numerical study of gravity waves during tropical cyclone Ivan (2008),” *Atmospheric Chemistry and Physics*, vol. 14, no. 2, pp. 641–658, 2014.
- [5] Y. A. Liou and S. K. Kar, “Evapotranspiration estimation with remote sensing and various surface energy balance algorithms—a review,” *Energies*, vol. 7, no. 5, pp. 2821–2849, 2014.

Research Article

Time-Series Mapping of PM₁₀ Concentration Using Multi-Gaussian Space-Time Kriging: A Case Study in the Seoul Metropolitan Area, Korea

No-Wook Park

Department of Geoinformatic Engineering, Inha University, Incheon 402-751, Republic of Korea

Correspondence should be addressed to No-Wook Park; nwpark@inha.ac.kr

Received 14 May 2015; Accepted 12 July 2015

Academic Editor: Chung-Ru Ho

Copyright © 2016 No-Wook Park. This is an open access article distributed under the Creative Commons Attribution License, which permits unrestricted use, distribution, and reproduction in any medium, provided the original work is properly cited.

This paper presents space-time kriging within a multi-Gaussian framework for time-series mapping of particulate matter less than 10 μm in aerodynamic diameter (PM₁₀) concentration. To account for the spatiotemporal autocorrelation structures of monitoring data and to model the uncertainties attached to the prediction, conventional multi-Gaussian kriging is extended to the space-time domain. Multi-Gaussian space-time kriging presented in this paper is based on decomposition of the PM₁₀ concentrations into deterministic trend and stochastic residual components. The deterministic trend component is modelled and regionalized using the temporal elementary functions. For the residual component which is the main target for space-time kriging, spatiotemporal autocorrelation information is modeled and used for space-time mapping of the residual. The conditional cumulative distribution functions (ccdfs) are constructed by using the trend and residual components and space-time kriging variance. Then, the PM₁₀ concentration estimate and conditional variance are empirically obtained from the ccdfs at all locations in the study area. A case study using the monthly PM₁₀ concentrations from 2007 to 2011 in the Seoul metropolitan area, Korea, illustrates the applicability of the presented method. The presented method generated time-series PM₁₀ concentration mapping results as well as supporting information for interpretations, and led to better prediction performance, compared to conventional spatial kriging.

1. Introduction

Outdoor air pollution has been known as one of the risk factors that affect human health directly and/or indirectly [1–4]. In Korea, it is reported that long-term exposure to ambient air pollution has a reasonable association with tuberculosis, cardiovascular diseases, and preterm delivery [5–7]. Thus, periodic monitoring and management of air pollution are required for exposure assessment for effective health management.

In Korea, several air pollutants including particulate matter less than 10 μm in aerodynamic diameter (PM₁₀), sulfur dioxide (SO₂), carbon monoxide (CO), nitrogen dioxide (NO₂), ozone (O₃), and particulate matter less than 2.5 μm in aerodynamic diameter (PM_{2.5}) have been periodically collected at several monitoring stations. Based on this real-time monitoring of air pollution, air quality levels are provided to the public domain [8]. Due to the few stations, however,

it is very difficult to analyze the spatial characteristics and spatiotemporal dynamics of air pollutants over a wide study area during the predefined time interval [9]. To overcome these difficulties, spatial interpolation or prediction is routinely applied to the sparse air pollutants observations to obtain exhaustive concentration values over the study area.

Among various spatial interpolation methods, geostatistical kriging has been widely applied to spatial interpolation tasks, due to its ability to account for spatial autocorrelation structures inherent to sample data and to integrate auxiliary data [10, 11]. When kriging is applied for spatial interpolation, spatial autocorrelation structures are quantified by variogram which denotes the spatial variability between samples as a function of distance [10]. If only sparsely sampled data are available, distinct spatial autocorrelation structures may not be captured from the sample data. As a result, spatial interpolation results would not show better prediction performance, compared to other deterministic interpolation

methods such as inverse distance weighting. If data are collected at a limited number of locations but continuously in a time domain such as air pollutants, temperature, and precipitation, temporal autocorrelation information may complement the lack of spatial autocorrelation information and improve the prediction performance for spatial interpolation tasks. Regarding the processing of this kind of space-poor but time-rich data, conventional geostatistical kriging, which was developed for considering spatial autocorrelation information only, can be extended to space-time kriging [12]. Space-time kriging or simulation has been applied to time-series mapping of various environmental variables such as air pollutants, temperature, and precipitation [13–16]. Despite its great potential for time-series mapping, however, uncertainties attached to the interpolation have not been fully accounted for. Most approaches have focused on the generation and interpretation of spatiotemporal mapping results. To the author’s knowledge, very few studies have been conducted using stochastic simulation [14] and local uncertainty assessment based on space-time kriging that does not require heavy computational cost is not fully considered. Recently, Park [17] presented a multi-Gaussian framework for time-series mapping of environmental variables. As the case study in [17] was carried out in the very small area, however, its applicability should be thoroughly investigated.

The main objective of this paper is to present space-time kriging capable of providing uncertainty assessment information and time-series mapping of PM_{10} concentrations. Within a spatial time-series framework [14, 17], conventional spatial multi-Gaussian kriging is extended to a space-time domain and its potential is illustrated via a case study of monthly PM_{10} concentration mapping in the Seoul metropolitan area, Korea.

2. Study Area and Data

A case study was conducted in the Seoul metropolitan area of Korea which includes 66 provincial districts in Seoul city, Incheon city, and Gyeonggi province (Figure 1). The metropolitan area covers approximately 11.78% of the entire land area of Korea and accounts for 49.07% of the entire population of Korea, as of 2014 and 2010, respectively [7, 18]. The study area comprised various types of land-covers, including the large urban areas of Seoul city and Incheon city located in the central and western parts of the study area, and the forests and agricultural lands (78.46% of the whole study area) located in the northern and eastern parts of the study area.

A monthly PM_{10} concentration dataset collected at 94 monitoring stations in the study area from January 2007 to December 2011 (60 months) was downloaded from the AirKorea website [8] and used for the case study. As shown in Figure 1, each district in the Seoul metropolitan city includes one station, but there are very few monitoring stations in other districts in Gyeonggi province, which comprised nearly half (47.74%) of the study area. This location information on the monitoring stations implies that relatively large uncertainties may be attached to the sparsely sampled locations. Within the administrative boundaries, 500 m interval grid

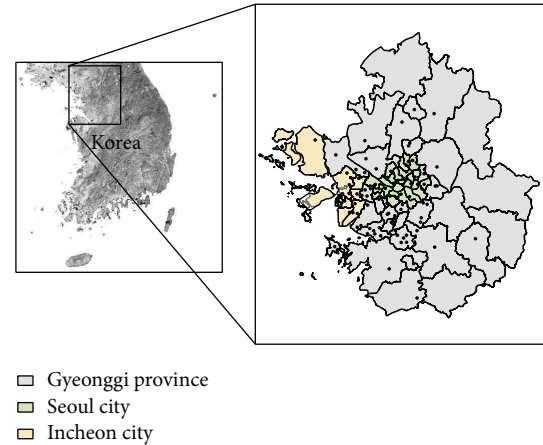


FIGURE 1: Locations of the study area and PM_{10} monitoring stations (black dots) with administrative boundaries.

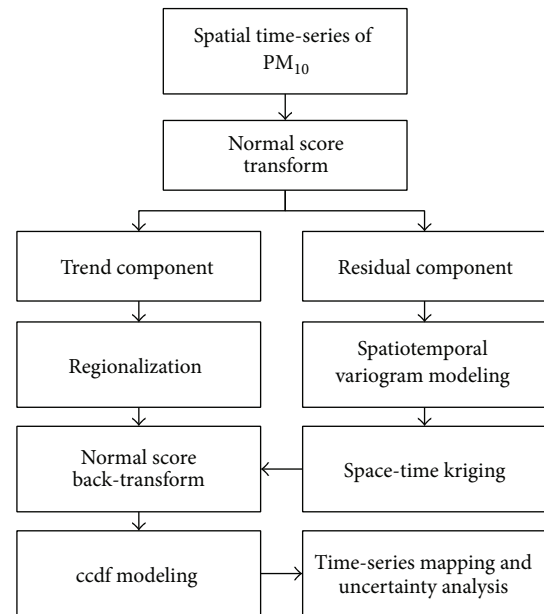


FIGURE 2: Work flows for multi-Gaussian space-time kriging presented in this study.

points were generated and PM_{10} concentrations were mapped at these points. It should be noted that the main purpose of this case study is to exemplify the analytical procedures and potential of the geostatistical approach presented in this paper, not to reveal detailed local characteristics of PM_{10} concentrations in the study area.

3. Method

Figure 2 illustrates the entire procedure for the multi-Gaussian spatial time-series approach presented in this paper.

3.1. Multi-Gaussian Spatial Time-Series Approach. The time-series PM_{10} concentration at each observation station was regarded as spatial time-series data and these spatial

time-series datasets were modelled as spatially correlated time-series random function models [14, 17]. Suppose that $\{Z(\mathbf{u}, t), t \in T, \mathbf{u} \in S\}$ denotes the spatially indexed time-series PM_{10} concentrations within the discrete time domain T and the continuous space domain S . In geostatistics, the uncertainty at any unmonitored location is usually modeled through the conditional cumulative distribution function (ccdf) which states the probability that the unknown attribute value does not exceed a certain threshold value z [10]. If this ccdf is extended to a space-time domain, the uncertainty at a certain location \mathbf{u} and time t is modeled via the following ccdf of $Z(\mathbf{u}, t)$:

$$F_Z(\mathbf{u}, t; z \mid (\text{info})) = \text{Prob}\{Z(\mathbf{u}, t) \leq z \mid (\text{info})\}, \quad (1)$$

where “ $\mid (\text{info})$ ” denotes conditioning to the local neighboring data both spatially and temporally.

In this study, multi-Gaussian space-time kriging was adopted for ccdf modeling as a parametric approach. Under the assumption that the ccdf at any location \mathbf{u} follows a Gaussian or normal distribution, the multi-Gaussian approach aims to predict the mean and variance, which are the two parameters that define the Gaussian ccdf [10]. To satisfy the assumption of a Gaussian ccdf, all monitoring data are transformed into a Gaussian space by normal score transform [11]. Then, the transformed spatial time-series dataset (Y) will follow a standard Gaussian distribution with a mean of 0 and a standard deviation of 1, and its ccdf is expressed as

$$F_Y(\mathbf{u}, t; y \mid (\text{info})) = G\left[\frac{y - E\{Y(\mathbf{u}, t) \mid (\text{info})\}}{\sqrt{\text{Var}\{Y(\mathbf{u}, t) \mid (\text{info})\}}}\right], \quad (2)$$

where $G[\cdot]$ is a standard Gaussian cumulative distribution function. $E\{Y(\mathbf{u}, t) \mid (\text{info})\}$ and $\text{Var}\{Y(\mathbf{u}, t) \mid (\text{info})\}$ are mean and variance values obtained by using the given neighboring data, respectively. These two values, which are required to define the Gaussian distribution, correspond to the simple kriging estimate and simple kriging variance, respectively.

To fully characterize the ccdf in (2), PM_{10} concentrations were modelled by decomposing the data into a deterministic trend component and a stochastic residual component [14, 17, 19]. The trend component is related to overall PM_{10} concentration patterns such as seasonal or regional variations. Meanwhile, the residual component, which is regarded as a second-order stationary random variable, includes local variations of PM_{10} concentration at a certain time and location and is the main target of geostatistical analysis. Since the multi-Gaussian approach was adopted in this study, this decomposition was applied to the normal score transformed dataset like

$$Y(\mathbf{u}, t) = m_G(\mathbf{u}, t) + R_G(\mathbf{u}, t), \quad (3)$$

where $m_G(\mathbf{u}, t)$ and $R_G(\mathbf{u}, t)$ denote the trend and residual components in a Gaussian space, respectively.

3.2. Trend Component Modeling. The trend component in (3) was modelled by weighted linear combination of elementary

temporal profile functions presented in [14]. Suppose that $Y(\mathbf{u}_\alpha, t_\beta)$ is a normal score transformed PM_{10} concentration at a certain monitoring station during the time period of 60 months ($\alpha = 1, \dots, 94, \beta = 1, \dots, 60$). The trend component at the α th monitoring station ($m_G(\mathbf{u}_\alpha, t_\beta)$) is expressed as a weighted sum of elementary temporal profile functions. Many elementary temporal profile functions can be applied for trend modeling. For example, periodicity and linear trend can be accounted for by combining linear and trigonometric functions. In this study, a spatially averaged time-series set computed from 94 monitoring stations [14] was used as the elementary temporal profile function for its simplicity:

$$m_G(\mathbf{u}_\alpha, t_\beta) = a_0(\mathbf{u}_\alpha) + a_1(\mathbf{u}_\alpha) \left[\frac{1}{94} \sum_{\alpha=1}^{94} Y(\mathbf{u}_\alpha, t_\beta) \right], \quad (4)$$

$$\beta = 1, \dots, 60,$$

where a_0 and a_1 correspond to the intercept and slope, respectively, in linear regression and are related to the similarity between a normal score transformed time-series at a certain monitoring station and the spatially averaged time-series set.

The above two regression coefficients are only available at monitoring stations after linear regression. Thus, they should be interpolated at all grid points in the study area for all time intervals in order to obtain the trend component distributions. If reasonable correlations are observed between two coefficients, simple cokriging, which can account for both the autocorrelation structures of the two coefficients and the cross-correlation structure between them, can be applied for spatial interpolation. Otherwise, univariate kriging or another deterministic interpolation method is independently applied to each coefficient. After regionalization or interpolation of the two coefficients, a trend component over the study area at each month was obtained by combining the interpolated coefficients with the spatially averaged time-series set.

3.3. Residual Component Modeling. The residual components, which are regarded as the second-order stationary random variable and subject to the main geostatistical analysis, were modelled via space-time kriging.

Spatiotemporal correlation structures required for the application of space-time kriging were first quantified via variogram modeling. The experimental spatiotemporal variogram is defined as

$$\hat{\gamma}(\mathbf{h}_s, h_t) = \frac{1}{2N(\mathbf{h}_s, h_t)} \cdot \sum_{\alpha=1}^{N(\mathbf{h}_s, h_t)} [R(u_\alpha, t_\alpha) - R(u_\alpha + \mathbf{h}_s, t_\alpha + h_t)], \quad (5)$$

where \mathbf{h}_s and h_t denote spatial lag distance and temporal interval, respectively, and $N(\mathbf{h}_s, h_t)$ is the number of data pairs within the class of spatiotemporal lags.

Among various spatiotemporal variogram models, a product-sum variogram model in [20] was applied to model the experimental spatiotemporal variogram. The product-sum variogram model is expressed as the combination of

marginal spatial and temporal variograms (i.e., purely spatial variogram and purely temporal variogram) as [20]

$$\begin{aligned} \gamma(\mathbf{h}_s, h_t) &= (k_1 C_s(0) + k_3) \gamma_t(h_t) \\ &+ (k_1 C_t(0) + k_2) \gamma_s(\mathbf{h}_s) \\ &- k_1 \gamma_s(\mathbf{h}_s) \gamma_t(h_t), \end{aligned} \quad (6)$$

where γ_s is the marginal spatial variogram and γ_t the marginal temporal variogram. $C_s(0)$ and $C_t(0)$ are the sill values of γ_s and γ_t , respectively.

Some parameters in (6) are also defined as [21]

$$\begin{aligned} k_1 &= \frac{[C_s(0) + C_t(0) - C_{st}(0,0)]}{[C_s(0) C_t(0)]}, \\ k_2 &= \frac{[C_{st}(0,0) - C_t(0)]}{C_s(0)}, \\ k_3 &= \frac{[C_{st}(0,0) - C_s(0)]}{C_t(0)}, \end{aligned} \quad (7)$$

where $C_{st}(0,0)$ is a sill value of the spatiotemporal variogram model.

After completion of the spatiotemporal variogram modeling, the residual components at all grid points in the study area for all time intervals were obtained by a linear combination of neighboring sample residual values within the pre-defined spatiotemporal search window via simple space-time kriging. The simple space-time kriging estimate ($r_G^*(\mathbf{u}, t)$) and variance ($\sigma_G^{2*}(\mathbf{u}, t)$) were computed as

$$\begin{aligned} r_G^*(\mathbf{u}, t) &= \sum_{\alpha=1}^{n(\mathbf{u}, t)} \lambda_{\alpha}(\mathbf{u}, t) r_G(\mathbf{u}_{\alpha}, t_{\alpha}), \\ \sigma_G^{2*}(\mathbf{u}, t) &= C_{st}(0,0) \\ &- \sum_{\alpha=1}^{n(\mathbf{u}, t)} \lambda_{\alpha}(\mathbf{u}, t) C_{st}(\mathbf{u}_{\alpha} - \mathbf{u}, t_{\alpha} - t), \end{aligned} \quad (8)$$

where $\lambda_{\alpha}(\mathbf{u}, t)$ is a simple kriging weighting value assigned to the neighboring sample residuals and $C_{st}(\mathbf{u}_{\alpha} - \mathbf{u}, t_{\alpha} - t)$ is a spatiotemporal covariance value between the estimation grid and neighboring sample locations. Since the residuals have a zero mean value, a constant mean value required for simple kriging is set to 0 and does not appear in (8).

3.4. ccdf Modeling. The space-time kriging estimate and variance for the residuals were used for fully characterizing the ccdf in a Gaussian space in (2). More specifically, the residual estimate at any grid point was added to the trend component at the corresponding grid point and then used as a mean value of the ccdf. Since the trend component was assumed to be deterministic, the space-time kriging variance was directly used as the variance value of the ccdf.

The ccdfs at all grid points in the study area were already fully known after applying the normal score back-transform. Then, certain statistics could be used as PM₁₀ concentration

estimates and uncertainty measures. The PM₁₀ concentration value ($z^*(\mathbf{u}, t)$) was empirically estimated from the expected value of the corresponding normal score back-transformed quantiles in the original space after discretizing the ccdf with many p quantiles ($y_p(\mathbf{u}, t)$) in the Gaussian space, as presented in [22, 23]

$$\begin{aligned} z^*(\mathbf{u}, t) &= \frac{1}{100} \sum_{\alpha=1}^{100} F^{-1} [G(y_p(\mathbf{u}, t))], \\ \text{with } p &= \frac{k}{100} - \frac{0.5}{100}, \end{aligned} \quad (9)$$

where $F^{-1}[G(y_p(\mathbf{u}, t))]$ denotes the normal score back-transformed values of the p quantiles in the Gaussian space.

Like the computation of the expected value of the ccdf, conditional variance ($\sigma^{2*}(\mathbf{u}, t)$) was also computed using (10) [23] and used as a measure of uncertainty:

$$\begin{aligned} \sigma^{2*}(\mathbf{u}, t) &= \frac{1}{100} \sum_{\alpha=1}^{100} [F^{-1} [G(y_p(\mathbf{u}, t))] - z^*(\mathbf{u}, t)]^2, \\ \text{with } p &= \frac{k}{100} - \frac{0.5}{100}. \end{aligned} \quad (10)$$

Unlike kriging variance that provides only the proximity from the sample data, conditional variance can provide information on the spread of the conditional probability distribution function or the steepness of the ccdf and thus can be used as a quantitative measure of the uncertainty. The larger the conditional variance, the greater the uncertainty attached to the prediction.

In addition to the computation of PM₁₀ concentration estimates and uncertainty measures from the ccdf, a probability of exceeding a certain critical concentration level can be easily computed. Based on this probability and the PM₁₀ concentration estimates, misclassification risks, which are associated with the classification of the study areas into hazardous and safe classes, can be computed and then used for decision supporting information.

Two misclassification risks α and β were considered in this study. Risk α , which is the probability of wrongly classifying any location \mathbf{u} as hazardous (i.e., false positive), is defined as [10]

$$\begin{aligned} \alpha(\mathbf{u}, t) &= \text{Prob} \{Z(\mathbf{u}, t) \leq z_k \mid z^*(\mathbf{u}, t) > z_k\} \\ &= F_Z(\mathbf{u}, t; z_k \mid (\text{info})), \end{aligned} \quad (11)$$

where z_k is a critical PM₁₀ concentration level.

Risk β , which is a probability of wrongly classifying any location \mathbf{u} as safe (i.e., false negative), is given as [10]

$$\begin{aligned} \beta(\mathbf{u}, t) &= \text{Prob} \{Z(\mathbf{u}, t) > z_k \mid z^*(\mathbf{u}, t) \leq z_k\} \\ &= 1 - F_Z(\mathbf{u}, t; z_k \mid (\text{info})). \end{aligned} \quad (12)$$

3.5. Validation. The prediction performance of multi-Gaussian space-time kriging was quantitatively evaluated by leave-one-out cross validation since kriging is an exact interpolator.

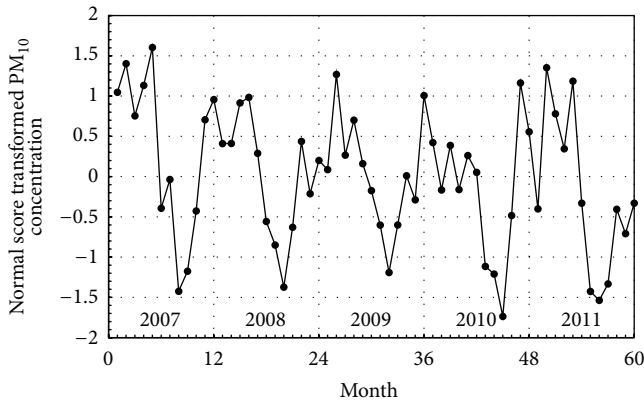


FIGURE 3: Spatially averaged time-series of normal score transformed monthly PM_{10} concentrations. Month 1 corresponds to January 2007 and Month 60 to December, 2011.

After one monitoring station was temporarily eliminated, kriging using the remaining stations was conducted to predict the PM_{10} concentration at the eliminated monitoring station. This procedure was repeated for all monitoring stations. Then the prediction performance was quantified using the linear correlation coefficient between the true PM_{10} concentration and the mean absolute error (MAE).

4. Results and Discussion

4.1. Trend Component Modeling Result. After preparing time-series PM_{10} concentration datasets, normal score transform was first applied using GSLIB [11]. Figure 3 shows a spatially averaged time-series that was computed from normal score transformed PM_{10} concentrations and used as the elementary temporal profile function. During the 5-year period from 2007 to 2011, a decreasing pattern was observed from April to August, but the increase in PM_{10} concentration commenced in fall and continued to winter. However, the winter PM_{10} concentration exhibited a different pattern each year. This overall pattern may be related to yellow dust in spring and meteorological factors such as wind, relative humidity, and precipitation. In winter and spring, the relatively stable atmospheric condition with high relative humidity and yellow dust contributes to the increase in PM_{10} concentration, respectively; meanwhile, the low PM_{10} concentration in summer is due to the washout effect by precipitation, as reported in previous studies [24, 25].

Regression between the spatially averaged time-series set and the time-series set at each monitoring station was conducted and two regression coefficients are presented in Figure 4. If the intercept and slope values approach zero and one, respectively, the time-series at the monitoring station is very similar to the spatially averaged time-series set. The different similarities at the monitoring stations led to differences of trend components, and hence the residual components, which are the main targets of space-time kriging, also varied across the study area.

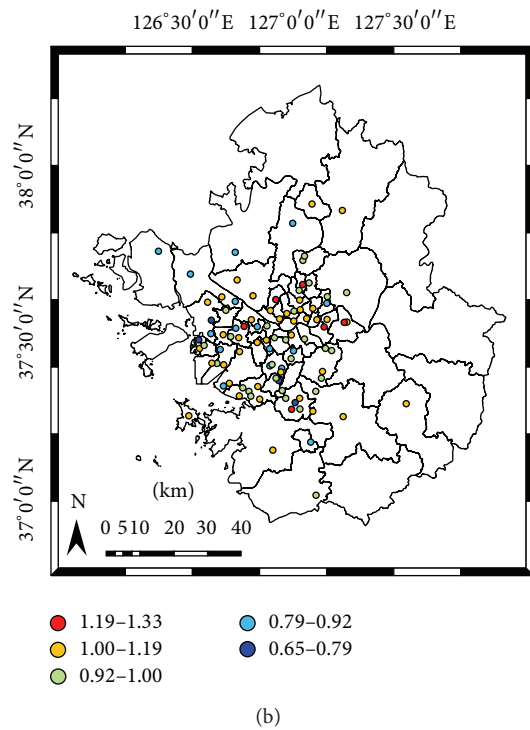
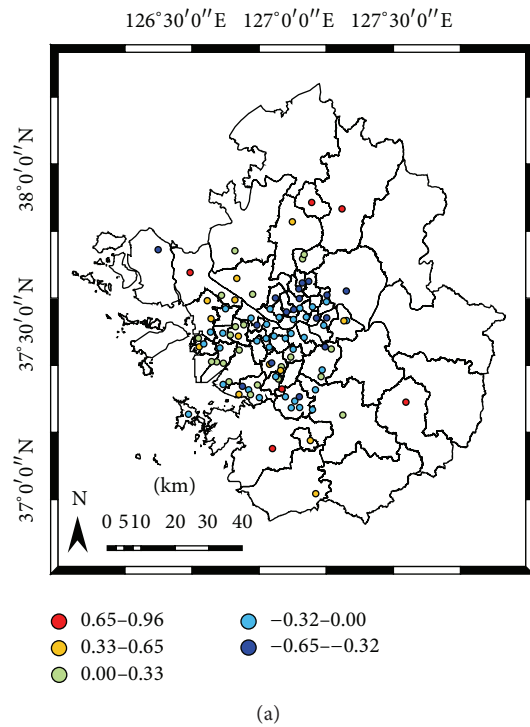


FIGURE 4: Two coefficients of local temporal trend components at monitoring stations: (a) intercept and (b) slope.

The next step for the regionalization or estimation of trend components at unmonitored locations was to interpolate the intercept and slope values in Figure 4. The linear correlation coefficient between the two coefficients at 94 monitoring stations was very low (-0.08), so an independent

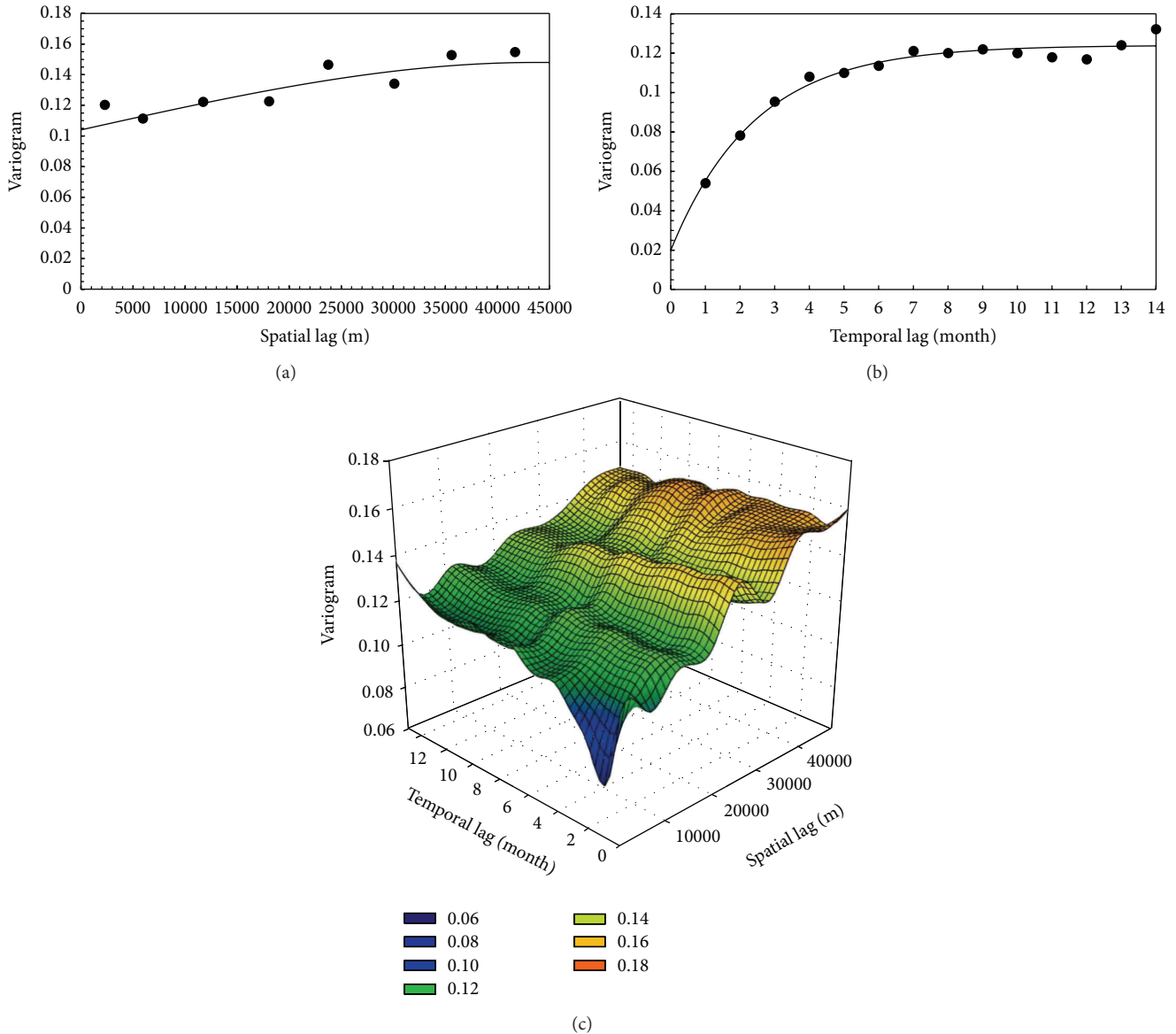


FIGURE 5: Marginal experimental variograms with the fitted model: (a) spatial variogram and (b) temporal variogram. Experimental spatiotemporal variogram surface of the residuals is shown in (c).

univariate ordinary kriging was applied to the two coefficients. By combining the interpolated regression coefficients with the spatially averaged time-series set in Figure 3, the trend components during the considered time period were retrieved and used for ccdf modeling.

4.2. Residual Component Modeling Result. After computing trend components at each monitoring station, the residual components that could not be explained by the trend components were computed at each monitoring station. The modified Fortran routines of De Cesare et al. [21] were used to compute the experimental spatiotemporal variogram. The marginal spatial and temporal experimental variograms of the residuals with the fitted models are given in Figures 5(a) and 5(b), respectively. The marginal spatial variogram

(Figure 5(a)) showed large relative nugget effects, but a reasonable temporal autocorrelation structure with an effective range of about 7 months was observed in the marginal temporal variogram (Figure 5(b)). This result implies that to account for temporal autocorrelation information during the interpolation could improve prediction performance, compared to the interpolation case with only spatial autocorrelation information. Figure 5(c) presents the experimental spatiotemporal variogram surface of the residuals. From this figure, the spatiotemporal variogram model, which satisfies the constraints in (8), was finally estimated and then used as an input variogram model for space-time kriging. Space-time kriging was applied to obtain the residuals at all grid points in the study area by using the spatiotemporal variogram model of the residuals. The Edinburgh space-time geostatistics

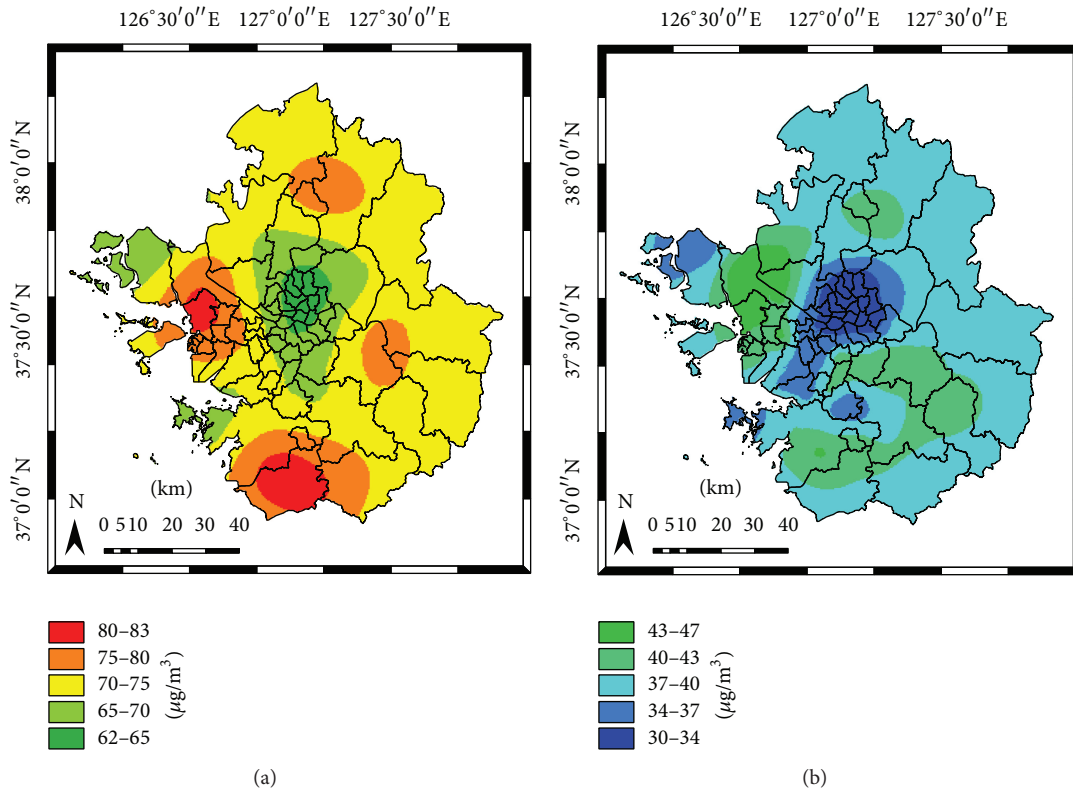


FIGURE 6: PM₁₀ concentration for (a) April 2009 and (b) August 2009.

Fortran program [26] was used to implement space-time kriging of the residuals.

4.3. PM₁₀ Concentration Mapping and Uncertainty Analysis Results. The simple space-time kriging estimate of the residuals was added to the interpolated trend components and then used as a mean value for the Gaussian ccdf at all locations. The simple space-time kriging variance was also used as the variance of the Gaussian ccdf, as in (2). After constructing ccdfs at all locations, the PM₁₀ concentration estimate and conditional variance were computed using (9) and (10), respectively. All postprocessing was implemented by Fortran programming and ArcGIS was used for visualization.

Only the PM₁₀ concentration mapping results for two months in 2011 are given in Figure 6, due to space limitation. The PM₁₀ concentration in April was much higher than that in August due to less precipitation and yellow dust transported to Korea by prevailing westerly winds in April. In April, relatively high PM₁₀ concentrations were observed in northern Incheon, Dongducheon, Pyeongtaek, and Gwangju due to the large concentrations either at the monitoring stations in those cities or at the nearby monitoring stations. The PM₁₀ concentration in August was relatively high in the northern Incheon, Gimpo, Dongducheon, Hwaseong, Seongnam, Gwangju, and northern Incheon. In both months, the northern Incheon, Dongducheon, and Gwangju showed relatively high concentrations, but low concentrations were observed in Seoul city.

The spatial distribution of conditional variance that measures the uncertainty for prediction is given in Figure 7. A large conditional variance was observed in some concentration areas (e.g., northern Incheon and Pyeongtaek in April and Gimpo in August, resp.) where the PM₁₀ concentration values at monitoring stations fluctuated greatly both temporally and spatially. Some areas with very few or even no monitoring showed relatively large conditional variance which is similar to conventional kriging variance. This uncertainty statistic revealed that the conditional variance, which provides information on both the sample variations and the sample configuration, can be used as supporting information to interpret the PM₁₀ concentration mapping result.

To generate misclassification risk maps, the probability of exceeding a certain threshold value was first mapped. The atmospheric environmental standard in Korea is defined only for an annual average ($25 \mu\text{g}/\text{m}^3$) or a 24-hour average ($100 \mu\text{g}/\text{m}^3$) [8]. Thus, it is not feasible to directly use the atmospheric environmental standard value as the threshold, since the monthly PM₁₀ concentration was considered in this study. Since the ccdfs were established at all locations in the study area, a variety of probability maps could easily be generated by applying different threshold values. For an illustration purpose, the PM₁₀ concentration of $80 \mu\text{g}/\text{m}^3$ was used as the threshold. By combining the classification result with the exceeding probability using a PM₁₀ concentration of $80 \mu\text{g}/\text{m}^3$ as the critical threshold, the risk α and risk β maps were generated, as shown in Figure 8. By definition, risk α is only mapped where the PM₁₀ concentration exceeds

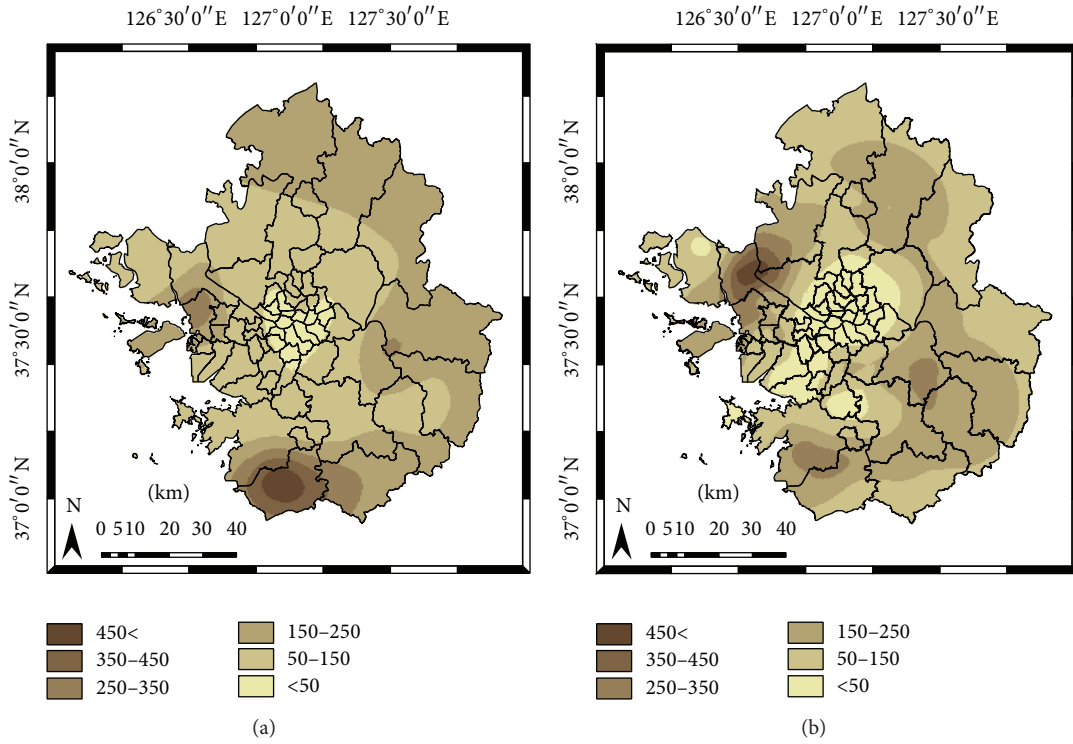


FIGURE 7: Conditional variance for (a) April 2009 and (b) August 2009.

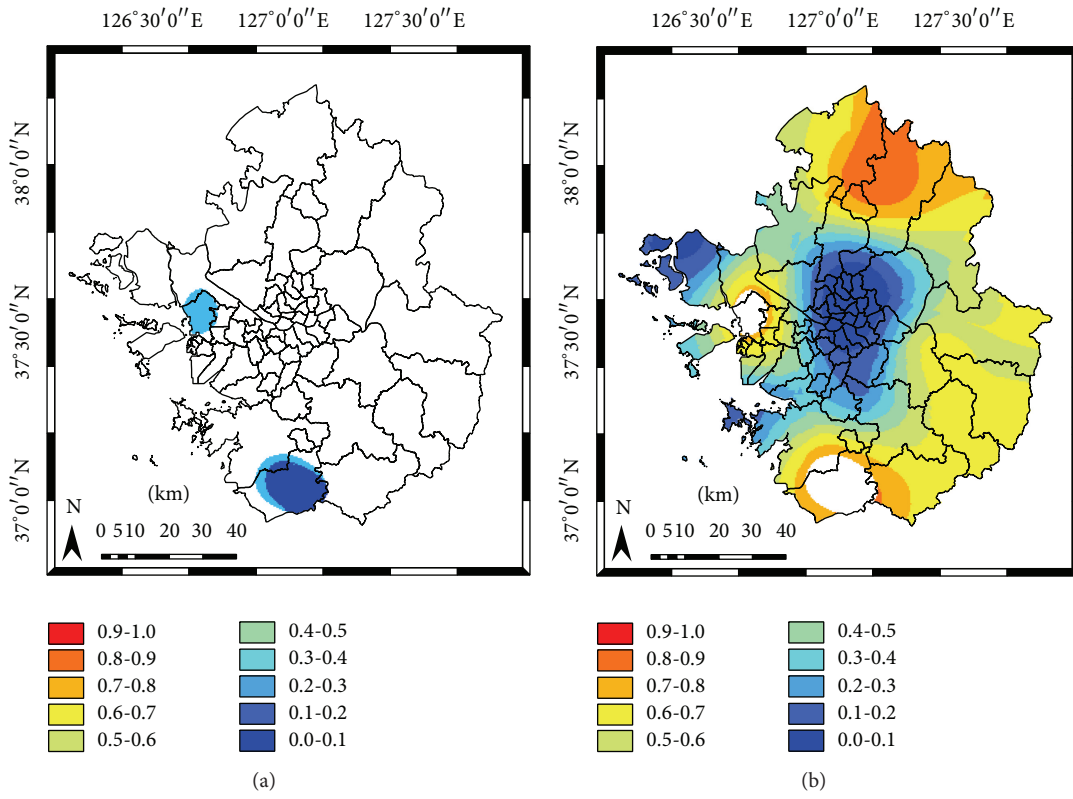


FIGURE 8: Risk associated with the classification of areas where the PM_{10} concentration exceeds $80 \mu g/m^3$ in April 2009: (a) risk α and (b) risk β .

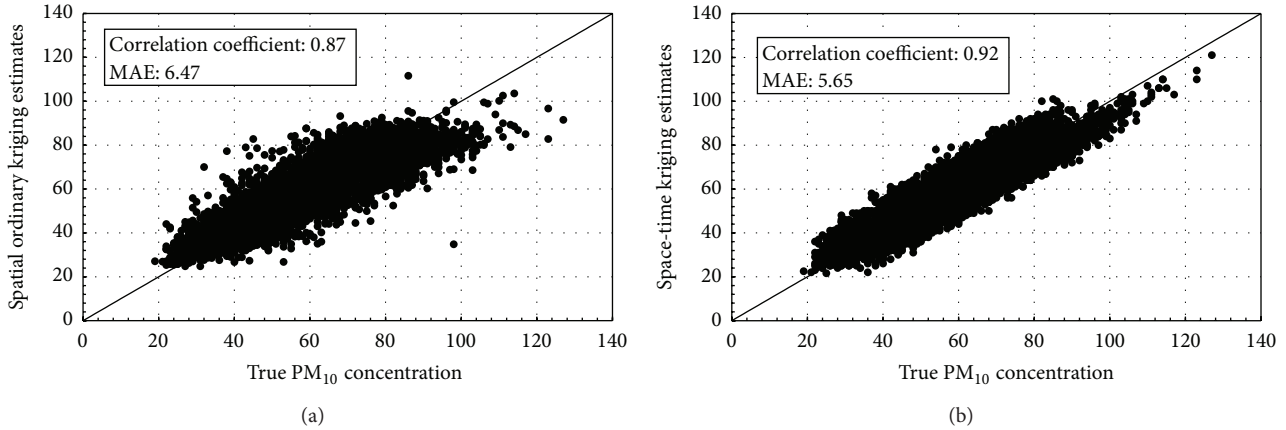


FIGURE 9: Scatter-plots with error statistics from leave-one-out cross validation: (a) spatial ordinary kriging and (b) space-time kriging.

the predefined threshold. On the contrary, risk β is defined where risk α is not mapped. In the risk α map in Figure 8(a), the false positive probability is relatively low (i.e., less than 0.3), but not negligible. The risk β map in Figure 8(b) shows very large variations of the false negative probability, which is greater than 0.7 in the northern part of the study area including Pocheon and Yeoncheon. A large misclassification risk β was also found around the areas that are classified as hazardous (i.e., exceeding the PM₁₀ concentration of 80 $\mu\text{m}/\text{m}^3$). Although choosing proper probability thresholds is difficult or subjective, these misclassification risk maps, which cannot be provided by deterministic interpolation methods or kriging algorithms without ccdf modeling, can be useful information for further decision-making or interpretations. For example, the areas showing high misclassification risk values can be considered as candidates for further monitoring or in-depth investigations.

4.4. Validation Results. To quantitatively evaluate the prediction performance of space-time kriging, leave-one-out cross validation was carried out and error statistics such as the linear correlation coefficient with the true values and MAE were computed. Spatial ordinary kriging, which considers only spatial autocorrelation information, was also applied for comparison purpose.

Figure 9 presents the scatter-plots with error statistics computed from leave-one-out cross validation. Although the underestimation of high values and overestimation of low values were observed in both results, this mismatch arising from the smoothing effects of kriging was relatively weakened in the validation result of space-time kriging. The linear correlation coefficients for space-time kriging and spatial ordinary kriging were 0.92 and 0.87, respectively. Space-time kriging also showed an improvement of 13.23% in MAE, compared to that of spatial ordinary kriging. Similar to the previous case study result in Park [17], these quantitative evaluation results confirmed that the incorporation of temporal autocorrelation information via space-time kriging improved the prediction performance and generated reliable mapping results for space-poor and time-rich data such as PM₁₀ concentrations.

5. Conclusions

A geostatistical approach based on spatiotemporal multi-Gaussian kriging was presented for time-series mapping of PM₁₀ concentrations. Unlike conventional space-time kriging and spatial kriging, which provide the estimate and kriging variance only, the presented approach generated rich interpretable by-products as well as the PM₁₀ estimates. From a case study in the Seoul metropolitan area of Korea, multi-Gaussian space-time kriging accounted for temporal autocorrelation information as well as spatial autocorrelation information and generated reliable mapping results that outperformed those of conventional spatial kriging. In addition, the presented approach produced uncertainty measures and misclassification risks from the ccdf modeling that are useful for interpretation or decision-making.

To strengthen the major findings of this study, several outstanding issues should be addressed in future work. First, several auxiliary variables such as the proximity to major roads and weather data will be integrated within the framework of the present study in order to generate much more reliable PM₁₀ concentration mapping results. In relation to uncertainty modeling, the multi-Gaussian approach adopted herein may not be appropriate for datasets with a strong positively skewed distribution which may be often observed in air pollutant concentrations. Thus, the extension of the conventional spatial indicator approach [10, 11] to the space-time domain and the comparison with the multi-Gaussian approach presented herein will also be included in future work.

Conflict of Interests

The author declares that there is no conflict of interests regarding the publication of this paper.

Acknowledgments

This research was supported by Basic Science Research Program through the National Research Foundation of Korea (NRF) funded by the Ministry of Science, ICT & Future Planning (NRF-2015R1A1A1A05000966). This work was also

supported by Inha University Research Grant. The author thanks Dr. L. Spadavecchia for providing the Edinburgh space-time geostatistics program.

References

- [1] J. Kaiser, "How dirty air hurts the heart," *Science*, vol. 307, no. 5717, pp. 1858–1859, 2005.
- [2] M. Medina-Ramón, A. Zanobetti, and J. Schwartz, "The effect of ozone and PM₁₀ on hospital admissions for pneumonia and chronic obstructive pulmonary disease: a national multicity study," *The American Journal of Epidemiology*, vol. 163, no. 6, pp. 579–588, 2006.
- [3] J. K. C. Ghosh, M. Wilhelm, J. Su et al., "Assessing the influence of traffic-related air pollution on risk of term low birth weight on the basis of land-use-based regression models and measures of air toxics," *American Journal of Epidemiology*, vol. 175, no. 12, pp. 1262–1274, 2012.
- [4] N. Carbajal, L. F. Pineda-Martinez, and F. B. Vicente, "Air quality deterioration of urban areas caused by wildfires in a natural reservoir forest of Mexico," *Advances in Meteorology*, vol. 2015, Article ID 912946, 13 pages, 2015.
- [5] S.-S. Hwang, S. Kang, J.-Y. Lee et al., "Impact of outdoor air pollution on the incidence of tuberculosis in the Seoul metropolitan area, South Korea," *Korean Journal of Internal Medicine*, vol. 29, no. 2, pp. 183–190, 2014.
- [6] J.-H. Leem, B. M. Kaplan, Y. K. Shim et al., "Exposures to air pollutants during pregnancy and preterm delivery," *Environmental Health Perspectives*, vol. 114, no. 6, pp. 905–910, 2006.
- [7] Y.-R. Lim, H.-J. Bae, Y.-H. Lim, S. Yu, G.-B. Kim, and Y.-S. Cho, "Spatial analysis of PM₁₀ and cardiovascular mortality in the Seoul metropolitan area," *Environmental Health and Toxicology*, vol. 29, Article ID e2014005, 2014.
- [8] AirKorea, <http://www.airkorea.or.kr/>.
- [9] B. Zou, Y. Luo, N. Wan, Z. Zheng, T. Sternberg, and Y. Liao, "Performance comparison of LUR and OK in PM_{2.5} concentration mapping: a multidimensional perspective," *Scientific Reports*, vol. 5, p. 8698, 2015.
- [10] P. Goovaerts, *Geostatistics for Natural Resources Evaluation*, Oxford University Press, New York, NY, USA, 1997.
- [11] C. V. Deutsch and A. G. Journel, *GSLIB: Geostatistical Software Library and User's Guide*, Oxford University Press, New York, NY, USA, 1998.
- [12] P. C. Kyriakidis and A. G. Journel, "Geostatistical space-time models: a review," *Mathematical Geology*, vol. 31, no. 6, pp. 651–684, 1999.
- [13] S. De Iaco, D. E. Myers, and D. Posa, "Space-time variograms and a functional form for total air pollution measurements," *Computational Statistics and Data Analysis*, vol. 41, no. 2, pp. 311–328, 2002.
- [14] P. C. Kyriakidis, N. L. Miller, and J. Kim, "A spatial time series framework for simulating daily precipitation at regional scales," *Journal of Hydrology*, vol. 297, no. 1–4, pp. 236–255, 2004.
- [15] A. Fernández-Cortés, J. M. Calaforra, R. Jiménez-Espinosa, and F. Sánchez-Martos, "Geostatistical spatiotemporal analysis of air temperature as an aid to delineating thermal stability zones in a potential show cave: implications for environmental management," *Journal of Environmental Management*, vol. 81, no. 4, pp. 371–383, 2006.
- [16] L. Spadavecchia and M. Williams, "Can spatio-temporal geostatistical methods improve high resolution regionalisation of meteorological variables?" *Agricultural and Forest Meteorology*, vol. 149, no. 6–7, pp. 1105–1117, 2009.
- [17] N.-W. Park, "Time-series mapping and uncertainty modeling of environmental variables: a case study of PM₁₀ concentration mapping," *Journal of the Korean Earth Science Society*, vol. 32, no. 3, pp. 249–264, 2011.
- [18] Korean Statistical Information Service (KOSIS), <http://kosis.kr/>.
- [19] P. J. Diggle and P. J. Ribeiro, *Model-Based Geostatistics*, Springer, New York, NY, USA, 1998.
- [20] L. De Cesare, D. Myers, and D. Posa, "Product–sum covariance for space–time modeling: an environmental application," *Environmetrics*, vol. 12, no. 1, pp. 11–23, 2001.
- [21] L. De Cesare, D. E. Myers, and D. Posa, "FORTRAN programs for space-time modeling," *Computers & Geosciences*, vol. 28, no. 2, pp. 205–212, 2002.
- [22] H. Saito and P. Goovaerts, "Geostatistical interpolation of positively skewed and censored data in a dioxin-contaminated site," *Environmental Science & Technology*, vol. 34, no. 19, pp. 4228–4235, 2000.
- [23] P. Goovaerts, G. Avruskin, J. Meliker, M. Slotnick, G. Jacquez, and J. Nriagu, "Geostatistical modeling of the spatial variability of arsenic in groundwater of southeast Michigan," *Water Resources Research*, vol. 41, Article ID W07013, 2005.
- [24] M.-K. Shin, C.-D. Lee, H.-S. Ha, C.-S. Choe, and Y.-H. Kim, "The influence of meteorological factors on PM₁₀ concentration in Incheon," *Journal of Korean Society for Atmospheric Environment*, vol. 23, no. 3, pp. 322–331, 2007 (Korean).
- [25] J.-Y. Lee, J.-S. Han, B.-J. Kong, Y.-D. Hong, J.-H. Lee, and I.-R. Chung, "Variation of PM₁₀ concentration in Seoul in association with synoptic meteorological conditions," *Journal of Environmental Impact Assessment*, vol. 16, no. 5, pp. 351–361, 2007 (Korean).
- [26] L. Spadavecchia, *Estimation of landscape carbon budgets: combining geostatistical and data assimilation approaches [Ph.D. thesis]*, University of Edinburgh, Edinburgh, Scotland, 2009.

Research Article

Association of Taiwan's Rainfall Patterns with Large-Scale Oceanic and Atmospheric Phenomena

Yi-Chun Kuo,^{1,2} Ming-An Lee,^{1,2,3} and Mong-Ming Lu⁴

¹Department of Environmental Biology and Fisheries Science, National Taiwan Ocean University, 2 Pei-Ning Road, Keelung 20224, Taiwan

²Center of Excellence for Oceans, National Taiwan Ocean University, 2 Pei-Ning Road, Keelung 20224, Taiwan

³Taiwan Group on Earth Observations, Zhubei, Hsinchu County 30274, Taiwan

⁴Research and Development Center, Central Weather Bureau, Taipei, Taiwan

Correspondence should be addressed to Ming-An Lee; malee@ntou.edu.tw

Received 30 January 2015; Revised 27 April 2015; Accepted 18 May 2015

Academic Editor: Jean-Pierre Barriot

Copyright © 2016 Yi-Chun Kuo et al. This is an open access article distributed under the Creative Commons Attribution License, which permits unrestricted use, distribution, and reproduction in any medium, provided the original work is properly cited.

A 50-year (1960–2009) monthly rainfall gridded dataset produced by the Taiwan Climate Change Projection and Information Platform Project was presented in this study. The gridded data (5×5 km) displayed influence of topography on spatial variability of rainfall, and the results of the empirical orthogonal functions (EOFs) analysis revealed the patterns associated with the large-scale sea surface temperature variability over Pacific. The first mode (65%) revealed the annual peaks of large rainfall in the southwestern mountainous area, which is associated with southwest monsoons and typhoons during summertime. The second temporal EOF mode (16%) revealed the rainfall variance associated with the monsoon and its interaction with the slopes of the mountain range. This pattern is the major contributor to spatial variance of rainfall in Taiwan, as indicated by the first mode (40%) of spatial variance EOF analysis. The second temporal EOF mode correlated with the El Niño Southern Oscillation (ENSO). In particular, during the autumn of the La Niña years following the strong El Niño years, the time-varying amplitude was substantially greater than that of normal years. The third temporal EOF mode (7%) revealed a north-south out-of-phase rainfall pattern, the slowly evolving variations of which were in phase with the Pacific Decadal Oscillation. Because of Taiwan's geographic location and the effect of local terrestrial structures, climate variability related to ENSO differed markedly from other regions in East Asia.

1. Introduction

Taiwan is located at the western edge of the Pacific Ocean with the Northern Tropic running through the island. Taiwan is one of the world's most mountainous islands and has five parallel mountain ranges that run roughly NNE–SSW. The Central Mountain Range (CMR) has five peaks with elevation above 3,500 m including Taiwan's highest peak Yu-Shan, 3,952 m (Figure 1). The climate of Taiwan is dominated by the East Asian monsoons, which bring northeasterly winds in winter and southwesterly winds in summer. The high mountain ranges make Taiwan's climate vary regionally, most notably in precipitation.

The southwesterly monsoon (from May to August) brings heavy rainfall to southwestern Taiwan, and the northeasterly monsoon (from September to April) causes rainfall over

the northeastern part of the island [1, 2]. Moreover, from mid-May to mid-June (Mei-Yu season), frontal systems from southern China and the convective systems embedded within the southwesterly monsoon flow frequently bring heavy rainfall [3]. From summer until fall, typhoons bring heavy rainfall to Taiwan. Wang et al. [4] divided the rainfall regimes in Taiwan into five categories: spring rain period (March and April), Mei-Yu period (May and June), summer rain period (July, August, and September), autumn rain period (October and November), and winter rain period (December, January, and February).

The rainfall pattern in Taiwan is complex because of the presence of the CMR. Yen and Chen [5] reported that, under the influence of the CMR, the basic seasonal variation of Taiwan rainfall between the southwesterly monsoon and the northeasterly monsoon is generated by a counterclockwise

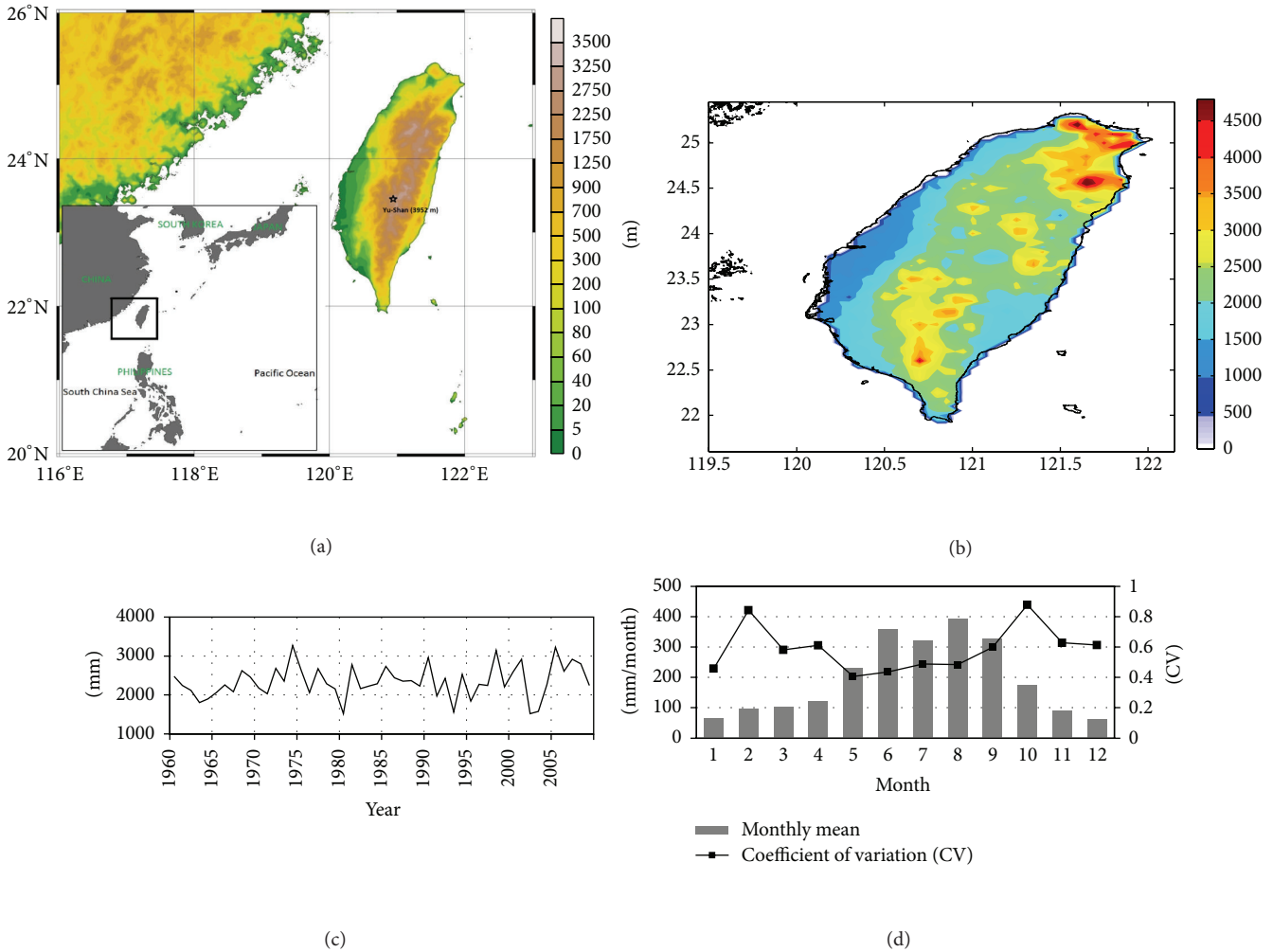


FIGURE 1: (a) The topography of Taiwan. (b) Distribution of annual rainfalls (mm/year) in Taiwan. (c) Variations in average annual rainfall over Taiwan during 1960–2009. (d) Variation in average monthly rainfall and the coefficient of variation (CV) of the averages over Taiwan during 1960–2009.

rotation of four rainfall regimes around Taiwan over a one-year cycle. Yeh [6] reported that typhoon rainfall in mountainous areas is enhanced as a result of the interaction of typhoons with the topography.

The large-scale variation of ocean-atmosphere interaction could be a remote driver of climate variability in Taiwan. Wang et al. [7] demonstrated that ENSO affects the climate in East Asia by causing an anomalous lower-tropospheric anticyclonic circulation around the Philippine Sea during the El Niño peak phase (from winter to ensuing spring). The anomalies sometimes persist into early summer and affect the rainfall in the East Asian subtropical front (the Mei-Yu season). Wang and Chan [8] compared tropical storm activity over the western North Pacific between La Niña and the stronger El Niño, suggesting a significant difference of life span and occurrence of TC in southeast and northwest quadrant of the western North Pacific. Jiang et al. [9] determined that rainfall during February–March is more and less than average following El Niño and La Niña

peak phases, respectively. On a decadal scale, the warm/cold phase of the PDO (Pacific Decadal Oscillation) enforces the southwesterly/northeasterly anomalous winds to the east of Taiwan during spring time (February–April) and this anomaly was related to spring rainfall variability in northern Taiwan [10]. J.-M. Chen and H.-S. Chen [11] observed a relationship between the PDO and interdecadal variability of summer rainfall in Taiwan. They suggested the large-scale SST anomalies associated with warm phase of PDO induced a low-level anomalous cyclonic circulation over the subtropical western Pacific. The northeasterly on the western edge of the anomalous cyclone reduced moisture transport from the South China Sea into Taiwan, resulting in less seasonal rainfall. However, because of the complex topography, the interannual and decadal variability in the rainfall pattern in Taiwan remain unclear.

A comprehensive understanding of the spatial and temporal variations in precipitation is required for improving the use of water resources and for planning diverse human

activities. In this study, we analyzed the gridded monthly precipitation data, obtained at a 5 km spatial resolution and collected from thousands of stations between 1960 and 2009, in order to comprehensively understand the spatial and temporal variations in rainfall and to reveal the long-term variation of rainfall in Taiwan. The results of our analyses identified the patterns associated with large-scale climate variability. In Section 2, we briefly describe the rainfall data and, in Section 3, we describe the results of empirical orthogonal function (EOF) analysis and their relationships with large-scale climatic variations. We discuss our findings and present our conclusions in Sections 4 and 5, respectively.

2. Data and Methods

The long-term gridded precipitation dataset was collected by the TCCIP (Taiwan Climate Change Projection and Information Platform Project; <http://tccip.ncdr.nat.gov.tw/NCDR/main/index.aspx>). The TCCIP has filtered observation data from more than 1,500 rain gauges through a homogeneous process, of which 1,187 are used to produce the gridded data. The original precipitation data were obtained from meteorological stations from the Central Weather Bureau, the Water Resources Agency, the Ministry of Economic Affairs, Irrigation Associations, and the Taiwan Power Company. Gaps in the data were filled with interpolated data by using the stations' spatial information to create a complete time series at each station. The weighting factors of station data are the functions of distance, elevation difference, and relative angular distribution with respect to the series under consideration [12]. To minimize errors caused by missing data, we included only the stations that have collected data over a period of longer than 20 days in one month. Monthly data were calculated as $(\sum_{i=1}^n X_i/n) * d$ (mm/month), where n is the total days of available data, X_1, X_2, \dots, X_n represent the daily precipitation data, and d is the total number of days in a month. The gridded method used here was based on Glasbey and Nevison [13], and the latent Gaussian variable (LGV) was used to avoid problems of singularity on days without rain and of a long upper tail in the case of daily rainfall data [14]. The final product featured a grid size of 5×5 km.

Figure 1(b), the distribution of annual rainfall averaged over 50 years, indicates that the rainfall is typically higher in mountain areas than in other parts of the island. Maximal rainfall occurs in the northeastern corner of Taiwan, reaching 4,000 mm annually, whereas the driest part is in the central west of the island, which receives roughly 1,000 mm of rain annually. The variation of annual rainfall is plotted in Figure 1(c). The annual accumulated-rainfall over the island varies substantially from year to year. It varies from 1600 to 3100 mm but the average is approximately 2,400 mm. The average annual variation and its coefficient of variation (CV) are plotted in Figure 1(d). The monthly rainfall peak is in August, and a second peak is in June. However, the variation is much larger in autumn and winter than in other seasons, as shown by the CV (Figure 1(d)). In order to identify the temporal variance that dominates the spatial structure, monthly rainfall variance during 1960–2009 was further investigated using the EOF method.

EOF analysis can help efficiently synthesize the information contained in physical quantities that vary spatially and temporally. In this approach, the data field is represented as the sum of a small number of orthogonal modes and the associated temporally varying amplitude (PCs). Temporal or spatial EOF analysis is performed by diagonalizing the covariance matrix to remove the spatial or temporal mean from the data. The amplitude function is calculated by projecting the data onto the orthogonal mode. Using this method facilitates the identification of physically and dynamically independent patterns. Temporal (spatial) EOF analysis generates a set of modes that explain fractions of temporal (spatial) variance. Thus, we can identify the temporal variance that dominates a spatial structure or the spatial variance that dominates the temporal variance of a spatial structure.

To detect the periodicity features of the PCs, the continuous wavelet transform (CWT) method was used in the current study. The Morlet wavelet, which provides a favorable balance between time and frequency localization, was applied. The cone of influence (COI) is the region of the wavelet spectrum in which edge effects become critical and is defined here as the e -folding time for the autocorrelation of wavelet power at each scale. A confidence level of 95% was adopted as the threshold at which to classify the significance of the wavelet power. Detailed information of the continuous wavelet transform used in the current study was introduced in-depth by Torrence and Compo [15].

To assess the association of the regional rainfall pattern with global SST changes, the gridded data ($1^\circ \times 1^\circ$) of monthly SSTs between 1960 and 2009 were retrieved from the UK Met Office Hadley Centre SST Climatology HadISST1 [16]. Monthly 850 mb winds data were obtained from the National Centers for Environmental Prediction (NCEP) reanalysis data, provided by NOAA/OAR/ESRL PSD (<http://www.esrl.noaa.gov/psd/data/gridded/data.ncep.reanalysis.html>).

The correlation coefficient between rainfall variance and the Nino 3.4 and PDO indices was computed in the study. Nino 3.4 (retrieved from <http://www.cpc.noaa.gov/data/indices/>) is the average sea surface temperature anomaly in the region bounded by 5°N to 5°S , from 170°W to 120°W . The US National Oceanic and Atmospheric Administration (NOAA) proposed an operational definition of El Niño that is based on a 3-month average of Niño 3.4 SST anomalies greater than or equal to 0.5°C . The PDO (Pacific Decadal Oscillation) index derived as the leading principal component of monthly SST anomalies in the North Pacific Ocean was downloaded from <http://research.jisao.washington.edu/pdo/PDO.latest>.

3. EOF Result

3.1. Temporal EOF Result. The first three modes of EOF that were applied to the monthly gridded data collected between 1961 and 2009 can explain up to 87% of the total variance. Figures 2 and 3 depict the modes and their corresponding temporally varying amplitudes (PCs). The fourth mode contributed to <3% of the total variance and was regarded as

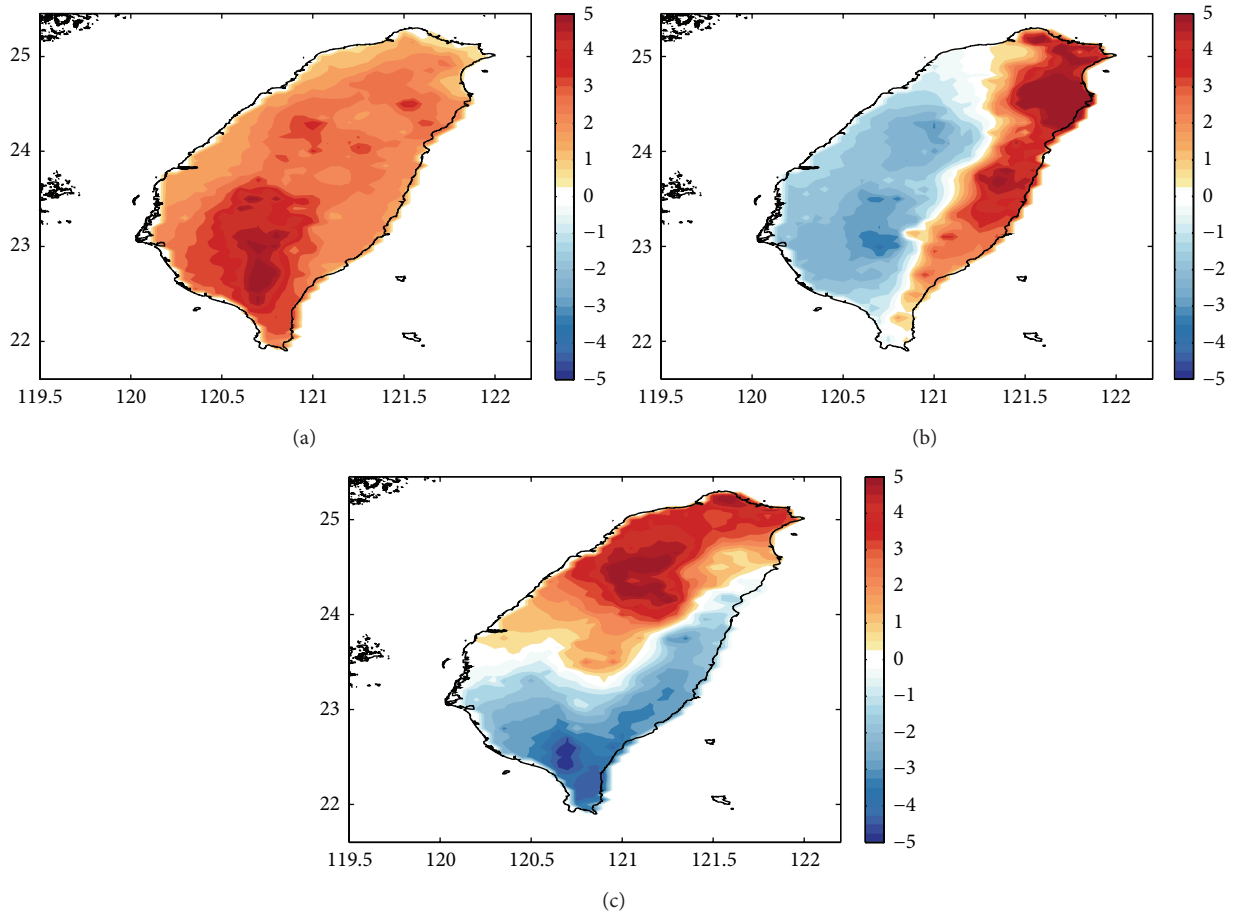


FIGURE 2: (a)–(c) Temporal EOF mode 1, mode 2, and mode 3 patterns.

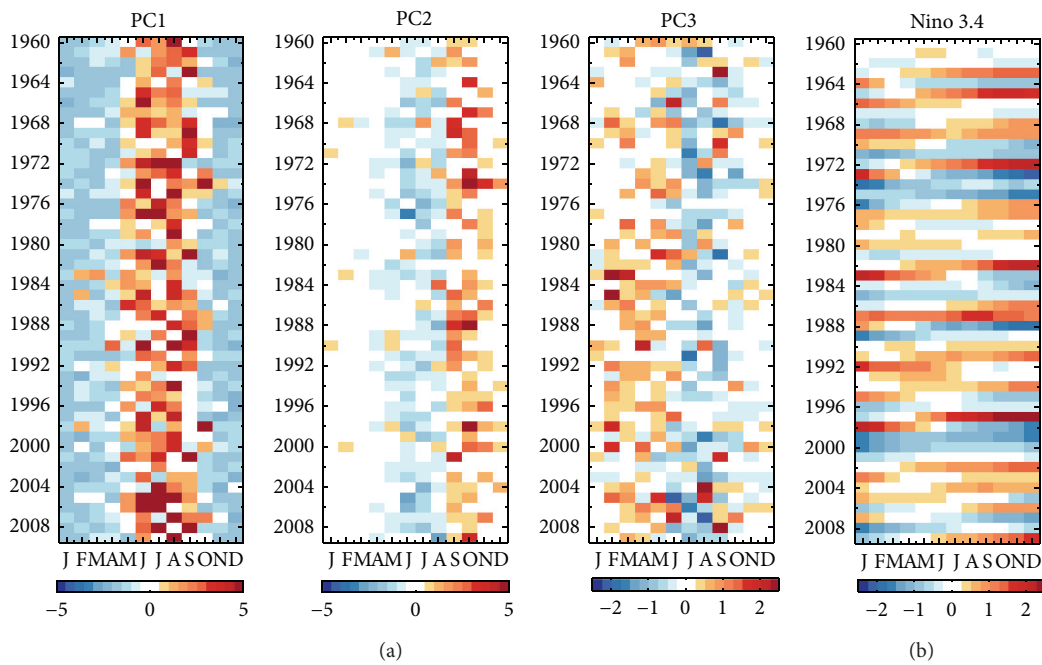


FIGURE 3: (a) The respective time-varying amplitude in the temporal EOF result. (b) Nino 3.4 index during 1960–2009. The Nino 3.4 index was retrieved from <http://www.cpc.noaa.gov/data/indices/>.

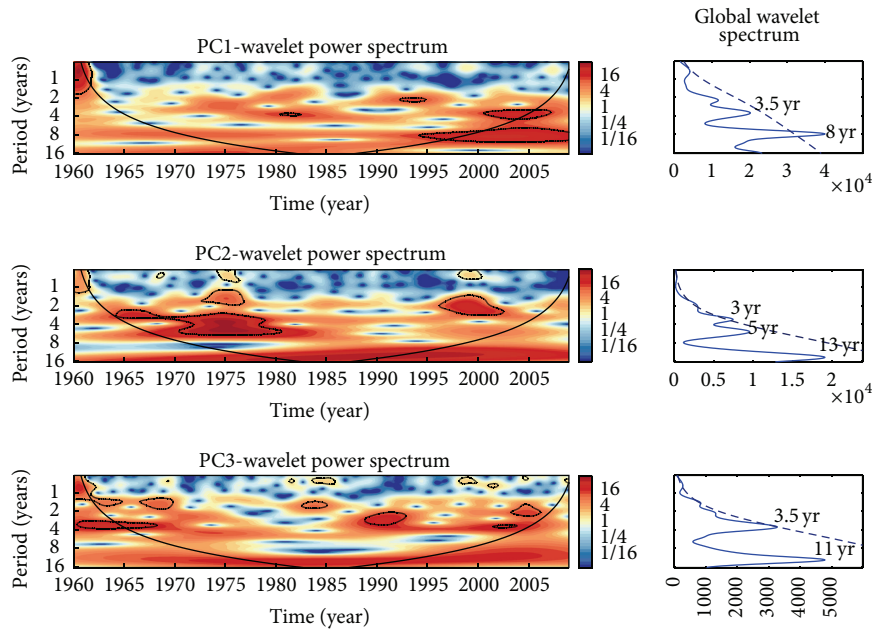


FIGURE 4: Results of wavelet analyses for PC1–PC3. The solid black contours show regions of greater than 95% confidence. The bowl-shaped line constitutes the cone of influence. For the global wavelet spectrum, periods corresponding to the peaks are indicated.

noise. The first mode, which accounted for 65% of the total variance, exhibited a spatially coherent in-phase pattern, with the highest rainfall values concentrated in the southwestern mountain area. The similarity between Figures 1(b) and 2(a) suggests that EOF1 captures the areas with large annual rainfalls except the northeastern part of the island which receives the largest amount of annual rainfall totals. The dissimilarity over the northeastern part of the island can be explained by EOF2 which shows that a substantial portion of the rainfall variance over northeast Taiwan is negatively correlated with the rains over the southern range of the CMR. In other words, the annual rainfall totals over the northeast and southwest Taiwan do not always vary coherently. The loading amplitudes of these two modes (Figure 3) clearly show the difference in their seasonality. EOF1 mainly captures the variations of the rainfall amount accumulated during the wet season from May to September, associated with southwesterly monsoons and typhoons during Mei-Yu and summer period. Because Figure 1 (annual mean) and Figure 2(a) (first EOF) are similar, the seasonal cycle is mainly a variation around the annual mean. In addition, EOF1 contains interannual variation. EOF2 captures the contrast variations of the rainfall amount accumulated during September–November (positive loading amplitude) and June–August (negative loading amplitude); EOF2 shows that northeast Taiwan receives more rainfall compared to southwest Taiwan during September–November and the contrast is opposite during June–August. Consequently, the annual mean and the seasonal cycle are mainly spatially controlled by mountains.

The interannual variation of the PC2 was strongest in autumn and it appeared to exhibit the signal of a strong ENSO (El Niño Southern Oscillation). Based on using the Niño 3.4 index (Figure 3(b)), we can conclude that the PC2

grew considerably during the La Niña years that followed strong El Niño years (1973–1974, 1988, and 1998). The third mode accounted for only 7% of the total variance and depicted a north-south out-of-phase pattern. The seasonal characteristics of the PC3 suggest that the contrast between north and south Taiwan is sharpest during the peak summer months. Sharp contrast can also be found during other time of a year, but the interannual variation is quite large. The PC3 typically showed positive values between February and May and negative ones during the other months. Decadal variation was observed in the positive phase of the third-mode time series and it increased around 1980.

To find periodicities greater than a year, the results of wavelet transform for the PCs are shown in Figure 4. A 12 m moving averaged was applied to remove the seasonal cycles. For PC1, higher power occurred in the 3.5 y and 8 y bands, although it was nonsignificant until 1995. Significant wavelet power can be observed in the 3–5 y band around 1965–1980 and 1995–2002 in PC2. A main periodicity of 11 y can also be observed in PC2. PC3 exhibited a 3.5 y cycle around 1990. Three main periodicities of 3.5 y and 11 y can be observed in the PC3.

3.2. The Relationship of the Leading Temporal EOF Modes with the SST and Low-Level Wind Field. In Figure 5(a), we plot the linear-regression map of global annual average SSTs against the annual average first-mode component of the EOF. The *F*-test was used to evaluate the significance of linear-regression coefficients. Because the seasonal variation was filtered out, the correlation between the first EOF and SSTs was not significant. Figure 5(b) is a plot of the linear-regression map of the global annual average SSTs against the annual average second-mode component of the EOF.

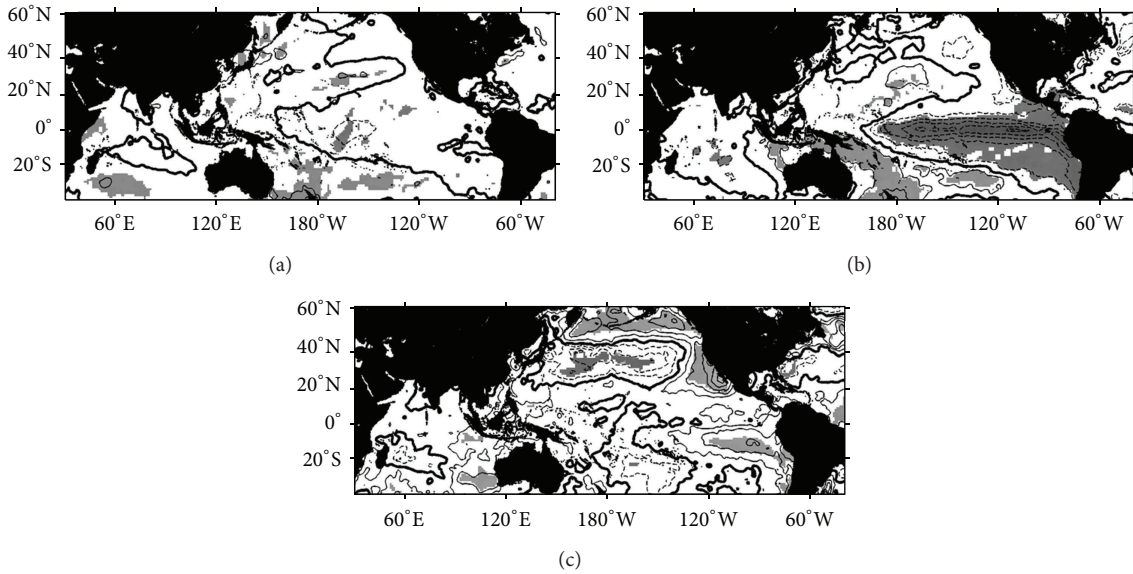


FIGURE 5: Regression maps of global annual average SST against (a) the first EOF, (b) the second EOF, and (c) the third EOF. The contour interval is 0.3°C . Shaded areas exceed the 90% confidence level. The solid lines and dashed lines are the positive and negative values, respectively. The thickened lines represent the value 0.

The overall pattern resembled the SSTA corresponding to ENSO events, revealing average SST warming and cooling across the central and eastern Pacific. Furthermore, the influence of the SST in the southern hemisphere was stronger than that in the northern hemisphere. The relationship between PC2 and ENSO is consistent with the wavelet analysis results (Figure 4), which demonstrated a 3–5 y cycle. Figure 5(c) shows a plot of the linear-regression map of the global annual average SSTs against the annual average third-mode component of the EOF. The pattern reveals a strong SST variation in the midlatitude region. This indicated a growing (decreasing) third-mode variance, representing a positive (negative) rainfall anomaly in northern Taiwan, which might be associated with a positive (negative) PDO phase. Studies have found that the variability of the Asian monsoon might play an active rather than passive role in tropical ENSO events. Conversely, ENSO events influence East Asian monsoons and have a systematic evolution associated with the annual cycle. To demonstrate the lead-lag relationship between EOF2 and ENSO, the lagged correlations of the PC2 with the Nino 3.4 index in the preceding and following months are plotted in Figure 6. A 2 mo running mean was applied to the EOF2 amplitude because the rainfall variations associated with large-scale phenomena typically have a time scale longer than 2 mo [17]. For the Nino 3.4 index, a 3 mo running mean is calculated to more effectively isolate variability closely related to the ENSO phenomenon. The most significant negative correlations were between mode 2 from October–November and the Nino 3.4 index obtained from the preceding June to the following May. The spatial pattern of mode 2 (Figure 2(b)) shows positive and negative values to the east and west of the CMR. The negative correlation between PC2 and Nino 3.4 means that it is wetter in eastern than in western Taiwan and drier in eastern than in western Taiwan during La Niña and El

Niño years, respectively. This observation indicates that after a mature phase of El Niño years, the western part of Taiwan is wetter than the eastern part is.

To demonstrate the wind variance associated with the most significant correlations between PC2 (October to November) and Nino 3.4 (from the preceding June to the following May, Figure 6(a)), Figure 6(b) shows the regression map of the second EOF averaged from October to November against an 850 mb wind stress averaged from September to November in the same year. The interannual variations of EOF2 were correlated with a cyclonic circulation anomaly over the South China Sea (SCS) and the anomalous easterly wind over the tropical western-central Pacific and westerly over the southern SCS and the Indian Ocean in the ongoing year. Figure 6(c) is the same as Figure 6(b), except that the wind speed is now a 3-month average, from December to February in the following year. The result indicates that a strong EOF2 during autumn was correlated with the enhanced anomalous winter northeasterly monsoon that is associated with an anticyclonic circulation anomaly over the Philippine Sea.

Figure 7(a) plots the correlation coefficients between the 2-month PC3 and the 3-month running mean PDO index obtained from the current year to the following year. The most significant positive correlations were between mode 3 from February–April and the Nino 3.4 index obtained from the preceding March to June. Figure 7(b) shows the regression map of the third mode averaged from February to March against the 850 mb wind stress averaged from January to March in the same year. The anticyclonic circulation anomaly over the Philippine Sea that is associated with the interannual variation of springtime rainfall in northern Taiwan agrees with the report of Hung et al. [10], who related this anomalous circulation to the PDO phase.

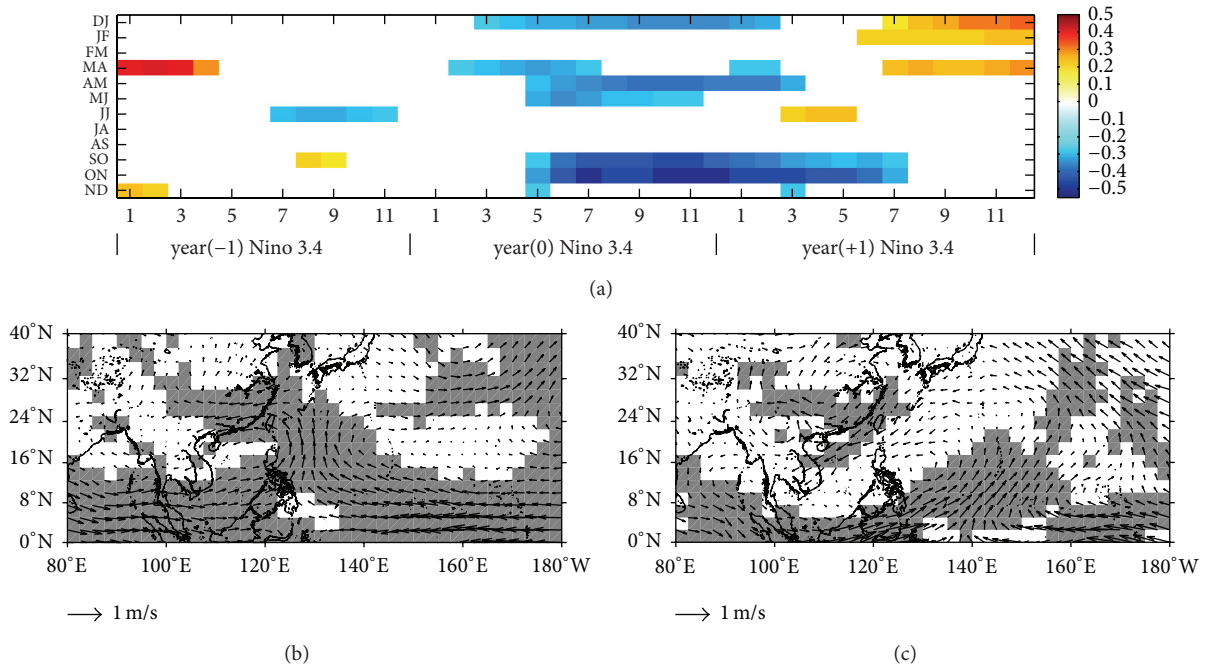


FIGURE 6: (a) Correlation map between 2-month mean EOF2 and Nino 3.4 index (significant at the 95% level). (b) Regression map of EOF2 averaged from October to November against 850 mb wind averaged from September to November in the concurrent years. (c) Regression map of EOF2 averaged from October to November against 850 mb wind averaged from December to February in the following years. Shaded areas exceed the 95% confidence level.

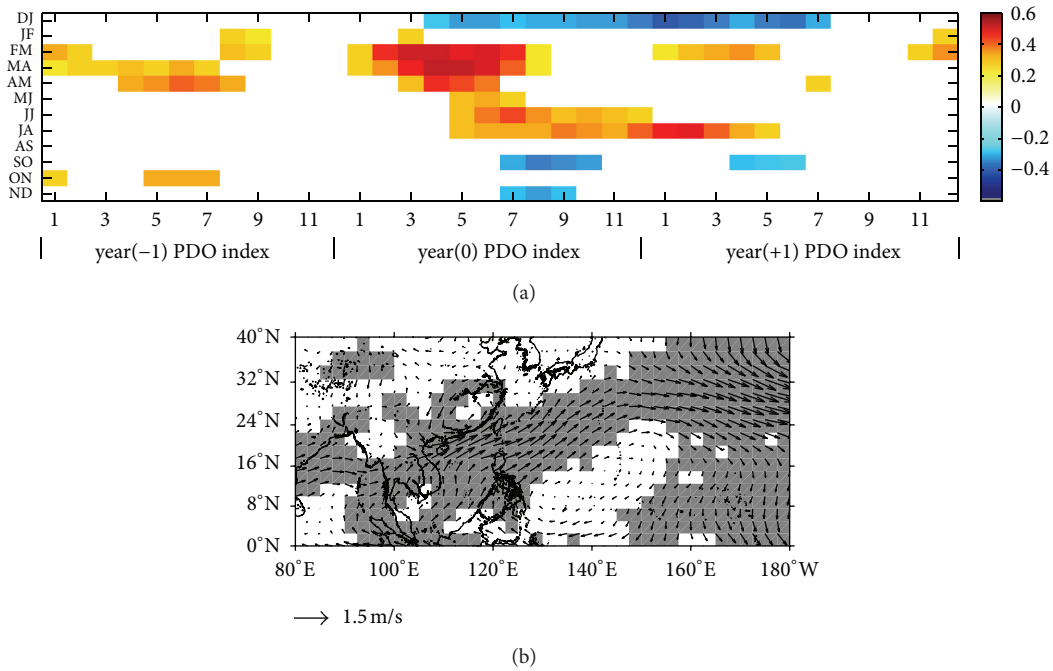


FIGURE 7: (a) Correlation map between 2-month mean EOF3 and PDO index (significant at the 95% level). (b) Regression map of EOF3 averaged from February to March against 850 mb wind speed averaged from January to March in the concurrent year. Shaded areas exceed the 95% confidence level.

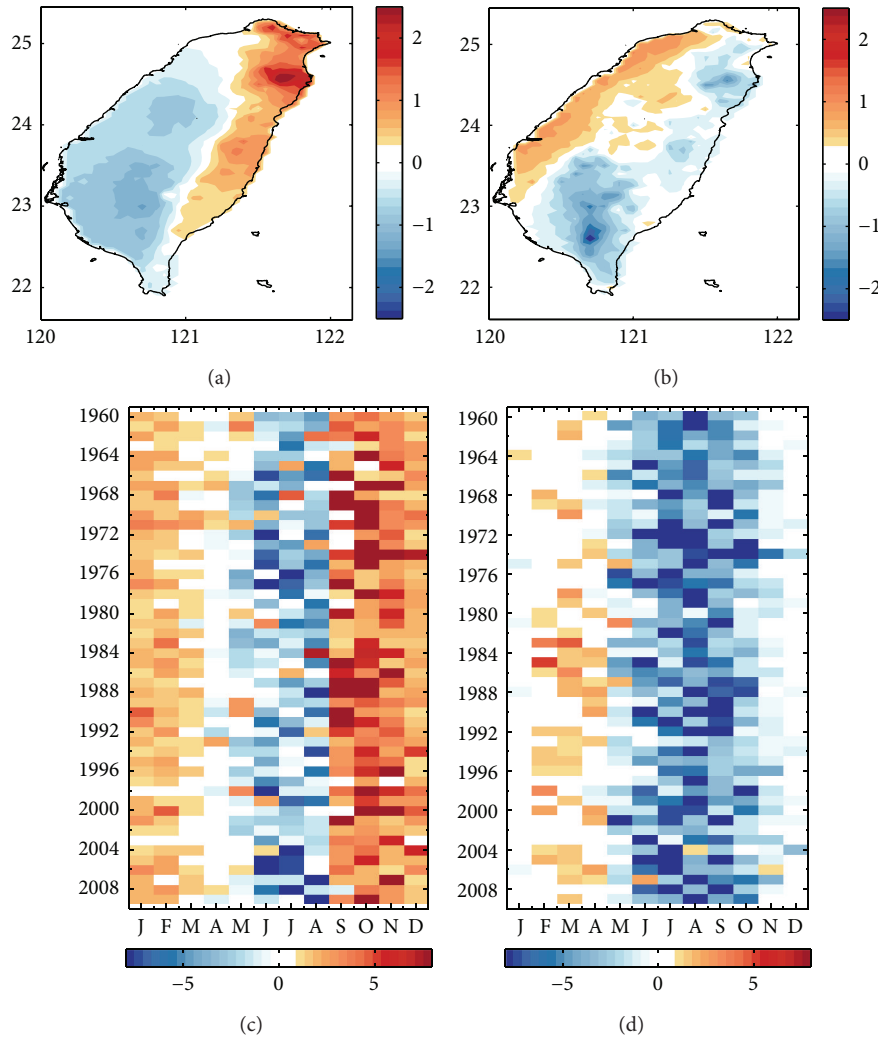


FIGURE 8: (a)-(b) Spatial EOF mode 1 and mode 2 patterns; (c)-(d) the corresponding amplitudes of the spatial EOF.

3.3. Spatial EOF Result. The results of spatial EOF analysis are presented in Figure 8. The first two modes can explain 61% of the total spatial variance, and the first mode (40%) showed a northeast-southwest out-of-phase pattern featuring the highest value in the northeastern region of Taiwan. This indicates that the largest spatial variance is associated with the seasonal monsoon transition and the interaction between monsoon and topography. A seasonal oscillation was detected in the time series of the first mode (Figure 8(b)). The amplitude was prominent during the three strong La Niña years (1974, 1989, and 1998), as it was in the time series of the temporal EOF second mode. In addition to exhibiting the peaks that might be associated with ENSO events, the magnitude has been increasing since 2005. The spatial EOF second mode (21%) reveals the difference in rainfall between the plain areas and windward mountain slopes. The seasonal variation of the second mode indicates higher rainfall in mountainous area than those in plain areas during summer to fall, which were associated with typhoons crossing the region. The critical role that the uplift of the extremely large moisture

flux plays in producing heavy rainfall is widely established [18–20]. However, the loading amplitude was the opposite during spring, indicating positive (negative) rainfall variance in the plain area (mountainous area).

Figure 9 plots the linear-regression map of the global annual average SSTs against the annual average of the first and second spatial EOF modes. The pattern of the first-mode regression map is similar to that shown in Figure 5(b), resembling the SSTA corresponding to ENSO events. The second-mode regression pattern showed that the relationship was significant in the midlatitude region, resembling a PDO positive phase pattern. This result seems consistent with J.-M. Chen and H.-S. Chen's [11] observation of similarities between the PDO index and typhoon rainfall in Taiwan from June to August. However the local rainfall variability associated with typhoons is not only modulated by the PDO on a decadal time scale and further study is required to explore the regulating processes relating to the large-scale ocean-atmosphere modes.

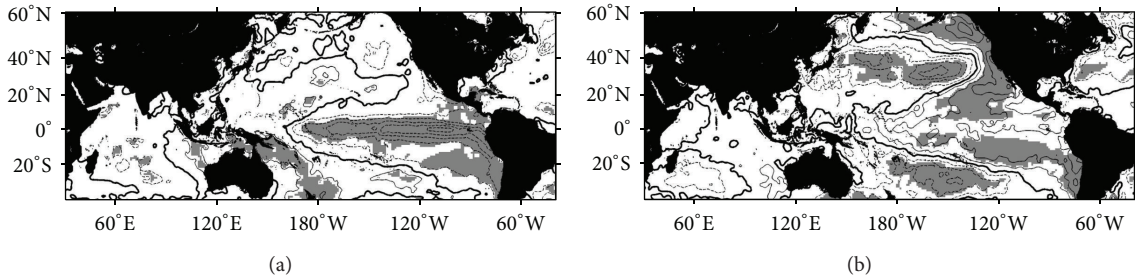


FIGURE 9: It is the same as Figure 5 but for (a) spatial EOF mode 1 and (b) spatial EOF mode 2.

4. Discussion

4.1. Comparison with Previous EOF Research. Yen and Chen [5] studied the seasonal transition of the rainfall pattern in Taiwan using the EOF method. In the present study, we collected monthly data from 15 coastal stations during the period of 1981 to 1997. We extracted the 1981–1997 data from our gridded data to compare the differences in the EOF result (not shown). Our results agree with those shown in Figure 2 in the report of Yen and Chen (2000). However, because more data were collected in our study than in the previous study, especially in the mountain areas, the contributions made by the first mode (78%) and the second mode (17%) in this report were higher and lower, respectively, than those (58% and 34%, resp.) of Yen and Chen [5]. Previous studies have demonstrated that the interactions between seasonal monsoons, tropical storms, and the topography of Taiwan could greatly amplify local rainfall [18–20]. Because the low-level circulation in Taiwan area is modified by large-scale climate variability, we can infer that the orography amplifies the rainfall response to large-scale phenomena variability.

4.2. Large-Scale Climate Variability. The East Asian monsoon and its interaction with the topography of Taiwan resulted in a rainfall anomaly pattern. The CMR played a critical role in the rainfall distribution. In addition, the rainfall pattern of the spatial EOF1 is similar to the temporal EOF2, indicating that the northeast-southwest out-of-phase pattern was the dominant spatial variance. In addition, the correlations between temporal EOF2 and SST resembled a pattern of the ENSO phenomenon.

The most significant correlation between EOF2 and the Niño 3.4 index was observed between the mean of EOF2 from October to November and the Niño 3.4 index from June in the ongoing year to April in the following year (Figure 6(a)). The anomalous easterly wind over the tropical western-central Pacific and the westerly over the tropical Indian Ocean during autumn (September to November) associated with the temporal EOF2 consisted of a wind circulation pattern typical of the developing La Niña period (Figure 6(b)). In addition, an anomalous cyclone also correlated with the temporal EOF2. The cyclonic circulation enhanced the moisture flux coming from the Pacific Ocean toward Taiwan. The southerly extending from the eastern flank of anomalous cyclones causes tropical cyclones to move northwestward toward the open oceans to the southwest of Taiwan.

The three peak values of the positive phase of the temporal EOF2 coincided with the La Niña years following an El Niño period. Chao et al. [21] found that, during a weaker northeasterly monsoon year such as an El Niño event, warm water tends to accumulate in the southern SCS. Thus, when northerly winds relax in spring, warm water returns northward, resulting in an enhanced spring warm pool (SWP) in the central SCS. Consequently, the anomalous cyclone shown in Figure 6(b) might be a regional atmospheric response to a local positive SST anomaly. The characteristics underlying this mechanism warrant further study. On the other hand, Kug and Kang [22] suggested a feedback process in which the warming in the Indian Ocean during the mature phase of an El Niño produces an anomalous easterly over the western edge of the Pacific, facilitating a fast transition to a La Niña.

As shown in Figure 6(c), during the developed La Niña winter, the response of the western Pacific to the SST anomaly over the tropical central-eastern Pacific is a cyclonic circulation anomaly over the Philippine Sea [7, 8]. This cyclonic circulation anomaly couples with the East Asia winter monsoon and further intensifies it. Wang et al. [7] used atmospheric general circulation models to demonstrate that, during El Niño years, an anomalous lower-tropospheric anticyclone located in the Philippine Sea formed as a result of a Rossby-wave response to suppressed convective heating, which is induced by both the in situ SST cooling and the subsidence forced remotely by the central Pacific warming. This anomalous anticyclone reduced the strength of the East Asia winter monsoon. By contrast, during the La Niña year, an anomalous lower-tropospheric cyclone located in the western North Pacific was observed [15].

Consequently, the autumn climate in Taiwan associated with ENSO exhibited substantial spatial variation because of the terrestrial effect. The climate variability associated with ENSO was distinct from that in other regions of East Asia. For example, Li et al. [23] used a gamma distribution function estimated from the historical sequence of daily precipitation and reported that extreme precipitation along the southeast coast of China in autumn occurred significantly more frequently in El Niño years than that in non-El Niño years. Wu et al. [17] documented the temporal evolution of ENSO-related seasonal rainfall anomalies in East Asia by using NCEP-NCAR reanalysis and station rainfall data (including 4 stations in Taiwan). They found positive correlations in southern China in fall during the onset of El Niño.

The anomalous low-level anticyclone developing over the SCS in fall and enhancing the moisture supply to southern China during the onset of El Niño was suggested to be responsible for the rainfall anomaly. By contrast, an anomalous cyclone during the onset of La Niña (Figure 6(b)) enhanced the moisture flux from the tropical western Pacific to the east of Taiwan.

PDOs are related to the rainfall variance presented by the third mode. According to the analyses of the third mode of the temporal EOF, rainfall increased in northern Taiwan and decreased in southern Taiwan in years where the PDO index was positive, and this trend was reversed in the years with a negative PDO index. Hung et al. [10] proposed that, during the warm PDO phase, the positive SSTAs over the tropical central-eastern Pacific that accompanied the enhanced Aleutian low and low SSTs in the extratropical North Pacific can induce a low-level anticyclonic anomalous flow over the Philippine Sea, resulting in the southwesterly anomalous winds toward the east of Taiwan and enhancing the trough extending southwestward from southern Japan to northern Taiwan.

5. Conclusion

In this paper, we describe the major decadal variations of rainfall in Taiwan between 1960 and 2009 based on the gridded monthly data produced by the TCCIP. The gridded data provided a clear view of the EOF pattern associated with the rainfall variance in Taiwan. The first mode of temporal EOF (65%) revealed that the annual peaks of large rainfalls in the southwestern mountain area of Taiwan are associated with southwesterly monsoons and typhoons during summer. The second mode of temporal EOF (16%) revealed a northeast-to-southwest out-of-phase distribution, roughly separated by the CMR, demonstrating the association of rainfall with the monsoon and its interaction with the CMR slope. The rainfall pattern of the spatial EOF1 is similar to the temporal EOF2, indicating that the pattern was the dominant spatial variance. The interannual variation of the second mode indicated the influence of ENSO events. The climate variability associated with ENSO was distinct from that in other regions of East Asia. The third mode of temporal EOF (7%) depicted a north-south out-of-phase pattern with slowly evolving variations that were approximately in phase with the PDO. These climate variations related to the anomalies of large-scale air-sea interaction in the Pacific might cause a substantial change in the low-level pressure field in East Asia. The regional topography further redistributes the rainfall.

Conflict of Interests

The authors declare that there is no conflict of interests regarding the publication of this paper.

Acknowledgments

This study was part of Taiwan Integrated Research Program on Climate Change Adaptation Technology (TaiCCAT), sponsored by the grants from the National Science

Council of Taiwan, NSC101-2625-M-019-006 and 102-2811-M-019-001. A special note of thanks is due to Dr. C. T. Shih for generous guidance through the revision process. The rainfall data were provided by the TCCIP (Taiwan Climate Change Projection and Information Platform Project; <http://tccip.ncdr.nat.gov.tw/NCDR/main/index.aspx>).

References

- [1] C.-S. Chen and J.-M. Huang, "A numerical study of precipitation characteristics over Taiwan island during the winter season," *Meteorology and Atmospheric Physics*, vol. 70, no. 3-4, pp. 167-183, 1999.
- [2] C.-S. Chen and Y.-L. Chen, "The rainfall characteristics of Taiwan," *Monthly Weather Review*, vol. 131, no. 7, pp. 1323-1341, 2003.
- [3] G. T.-J. Chen, "Mesoscale features observed in the Taiwan Mei-Yu season," *Journal of the Meteorological Society of Japan*, vol. 70, pp. 497-516, 1992.
- [4] C. H. Wang, L. A. Li, and W. C. Liu, "Some characteristics of the precipitation in Taiwan," in *Biodiversity and Terrestrial Ecosystem*, C. I. Peng and C. H. Chou, Eds., Academia Sinica Monograph Series no. 14, pp. 343-354, Institute of Botany, 1994.
- [5] M.-C. Yen and T.-C. Chen, "Seasonal variation of the rainfall over Taiwan," *International Journal of Climatology*, vol. 20, no. 7, pp. 803-809, 2000.
- [6] T.-C. Yeh, "Typhoon rainfall over Taiwan area: the empirical orthogonal function modes and their applications on the rainfall forecasting," *Terrestrial, Atmospheric and Oceanic Sciences*, vol. 13, no. 4, pp. 449-468, 2002.
- [7] B. Wang, R. Wu, and X. Fu, "Pacific-East Asian teleconnection: how does ENSO affect East Asian climate?" *Journal of Climate*, vol. 13, no. 9, pp. 1517-1536, 2000.
- [8] B. Wang and J. C. L. Chan, "How strong ENSO events affect tropical storm activity over the western North Pacific," *Journal of Climate*, vol. 15, no. 13, pp. 1643-1658, 2002.
- [9] Z. Jiang, G. T.-J. Chen, and M.-C. Wu, "Large-scale circulation patterns associated with heavy spring rain events over Taiwan in strong ENSO and Non-ENSO years," *Monthly Weather Review*, vol. 131, no. 8, pp. 1769-1782, 2003.
- [10] C.-W. Hung, H.-H. Hsu, and M.-M. Lu, "Decadal oscillation of spring rain in northern Taiwan," *Geophysical Research Letters*, vol. 31, no. 22, Article ID L22206, 4 pages, 2004.
- [11] J.-M. Chen and H.-S. Chen, "Interdecadal variability of summer rainfall in Taiwan associated with tropical cyclones and monsoon," *Journal of Climate*, vol. 24, no. 22, pp. 5786-5798, 2011.
- [12] C. Simolo, M. Brunetti, M. Maugeri, and T. Nanni, "Improving estimation of missing values in daily precipitation series by a probability density function-preserving approach," *International Journal of Climatology*, vol. 30, no. 10, pp. 1564-1576, 2010.
- [13] C. A. Glasbey and I. M. Nevison, "Rainfall modelling using a latent gaussian variable," in *Modelling Longitudinal and Spatially Correlated Data*, vol. 122 of *Lecture Notes in Statistics*, pp. 233-242, Springer, 1997.
- [14] S.-P. Weng and C.-T. Yang, "The construction of monthly rainfall and temperature datasets with 1 km gridded resolution over Taiwan Area (1960-2009) and its application to climate projection in the near future (2015-2039)," *Atmospheric Sciences*, vol. 40, pp. 349-370, 2012 (Chinese).

- [15] C. Torrence and G. P. Compo, "A practical guide to wavelet analysis," *Bulletin of the American Meteorological Society*, vol. 79, no. 1, pp. 61–78, 1998.
- [16] N. A. Rayner, D. E. Parker, E. B. Horton et al., "Global analyses of sea surface temperature, sea ice, and night marine air temperature since the late nineteenth century," *Journal of Geophysical Research*, vol. 108, no. 14, p. 4407, 2003.
- [17] R. Wu, Z.-Z. Hu, and B. P. Kirtman, "Evolution of ENSO-related rainfall anomalies in East Asia," *Journal of Climate*, vol. 16, no. 22, pp. 3742–3758, 2003.
- [18] X. Ge, T. Li, S. Zhang, and M. Peng, "What causes the extremely heavy rainfall in Taiwan during Typhoon Morakot (2009)?" *Atmospheric Science Letters*, vol. 11, no. 1, pp. 46–50, 2010.
- [19] M. S. Peng and S. W. Chang, "Numerical forecasting experiments on Typhoon Herb (1996)," *Journal of the Meteorological Society of Japan*, vol. 80, no. 6, pp. 1325–1338, 2002.
- [20] C.-C. Wu and Y.-H. Kuo, "Typhoons affecting Taiwan—Current understanding and future challenges," *Bulletin of the American Meteorological Society*, vol. 80, no. 1, pp. 67–80, 1999.
- [21] S.-Y. Chao, P.-T. Shaw, and S. Y. Wu, "Deep water ventilation in the South China Sea," *Deep Sea Research Part I: Oceanographic Research Papers*, vol. 43, no. 4, pp. 445–466, 1996.
- [22] J. S. Kug and I. S. Kang, "Interactive feedback between ENSO and the Indian Ocean," *Journal of Climate*, vol. 19, no. 9, pp. 1784–1801, 2006.
- [23] W. Li, P. Zhai, and J. Kai, "Research on the relationship of ENSO and the frequency of extreme precipitation events in China," *Advances in Climate Change Research*, vol. 2, no. 2, pp. 101–107, 2011.

Research Article

Analysis of Long-Term Meteorological Observation for Weather and Climate Fundamental Data over the Northern Tibetan Plateau

Fangfang Huang^{1,2} and Weiqiang Ma^{1,3,4}

¹Key Laboratory for Land Process and Climate Change in Cold and Arid Regions, Cold and Arid Region Environmental and Engineering Research Institute, Chinese Academy of Sciences, Lanzhou 730000, China

²University of Chinese Academy of Sciences, Beijing 100049, China

³A Key Laboratory of Tibetan Environment Changes and Land Surface Processes, Institute of Tibetan Plateau Research, Chinese Academy of Sciences, Beijing 100101, China

⁴CAS Center for Excellence in Tibetan Plateau Earth Sciences, Beijing 100101, China

Correspondence should be addressed to Weiqiang Ma; wqma@itpcas.ac.cn

Received 9 April 2015; Accepted 3 June 2015

Academic Editor: Chung-Ru Ho

Copyright © 2016 F. Huang and W. Ma. This is an open access article distributed under the Creative Commons Attribution License, which permits unrestricted use, distribution, and reproduction in any medium, provided the original work is properly cited.

Meteorological observation plays a critical role in climatic study, and in situ measurements are the foundation of meteorological observation, especially in the Tibetan Plateau, the surface of which is fairly complex. Several field stations in the Northern Tibetan Plateau, which features relatively homogeneous surface, were selected as the study area. A detailed description on the significance of site observation for climate prediction was given in this paper. Data from weather stations can be used to verify satellite data and provide parameters for initial mode field in the study of weather and climate changes. The field observation data in the Northern Tibetan Plateau from 2001 to 2013 is analyzed. The results show that in El Nino year, values of land surface temperature (T_s), air temperature (T_a) and wind speed are all greater than their mean values and that soil moisture values are lower than the averaged, while the opposite is the case in La Nina year. The warming rate in the Northern Tibetan Plateau is greater than that in global areas. The diurnal variations of T_s and T_a are various in different seasons and underlying surfaces, with the diurnal variations greater in spring, and less in summer and autumn. Furthermore, the diurnal variation in the area with drier underlying surface is more obvious than that in area with moist surface.

1. Introduction

It is well recognized that the Tibetan Plateau plays an important role in the East Asian and global climate because of its high elevation and complex surface conditions. The land surface of the Tibetan Plateau reaches elevations of greater than 4000 m above sea level, which is about a third of the height of the troposphere. It interacts with the atmosphere through radiation, sensible heat flux, and latent heat flux, and because of its topographic condition, the Tibetan Plateau exerts profound dynamical and thermal influences on Asian monsoon, the atmospheric circulation, and global climate change [1–3]. The huge heat source certainly has an effect on the vertical circulation over the plateau and its surrounding areas. The heat source can impact Chinese precipitation in

summer by changing the intensity of the East Asian monsoon [4].

Decades of research on the Tibetan Plateau indicates that the plateau plays a vital part in the East Asian and global weather and climate prediction. Then the long-term meteorological observation in the plateau is essential and crucial for the research. Scientists have started to observe the atmospheric condition over the Tibetan Plateau systematically since 1970s. The first atmospheric science experiment on the Tibetan Plateau in 1979 (QXPME-1979) was performed by Ye and Gao. In that field experiment, the variation and distribution characteristics of each component in the land surface radiation balance and heat balance were analyzed, and the changing process of the heat source has been well understood [5–9]. Afterwards, the second atmospheric

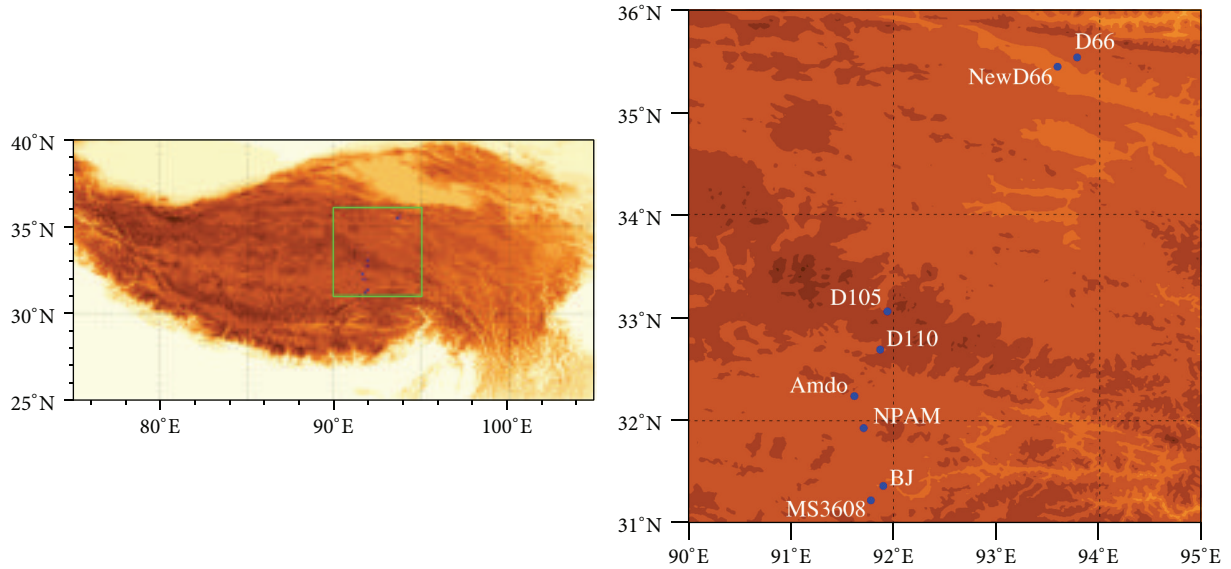


FIGURE 1: Map for the observation area and locations of stations in the Northern Tibetan Plateau.

science experiment on the Tibetan Plateau (TIPEX) was started in 1998. With the attention for the influence of the atmospheric hydrological process on the Asian monsoon increasing, the global energy and water cycle experiment (GEWEX) included the experiments called “GAME/Tibet” and “CAMP/Tibet,” which mainly aimed for researching the energy exchange between land and atmosphere in the Tibetan Plateau [10]. And in order to recognize the interaction between land and atmosphere further and quantitatively, these experiments covered the observation for the solar radiation, soil temperature and soil moisture, air temperature and pressure, soil heat flux, sensible and latent heat flux, and so on. Moreover, radiosonde observation has provided amount of data for the meteorological observation. The wind speed and direction, air temperature, moisture, and pressure data in the upper air are used to judge the atmospheric stratification and circulation situation [11].

However, the Tibetan Plateau covers a vast geographic area with various landforms, and the research is largely deficient only by a few of weather stations. But the remote sensing observation features large coverage and can obtain different surface parameters simultaneously, and it makes up the deficiency for the conventional observation data. With the developing of the satellite remote sensing, using satellite data to research various weather systems over the plateau has been a popular way. Meanwhile, an important method of estimating the air temperature by satellite data has been put forward, and it benefits the research on the land-atmosphere interaction [12, 13]. In addition, the essential data for the weather forecast and climate modeling and prediction are the land surface parameters, such as the soil temperature and moisture, reflectivity, emissivity, and roughness. Since the values of underlying surface are generally constant in current numerical models, the models are hard to reflect the reality of climate change [14, 15]. On the other hand, the satellite remote sensing plays a unique role in terms of

TABLE 1: The basic information of all sites.

Stations	Longitude and latitude	Elevation	Underlying surface
NewD66	35.43°N, 93.59°E	4465 m	Alpine sparse grassland
D105	33.06°N, 91.94°E	5039 m	Alpine meadow
NPAM	31.93°N, 91.71°E	4620 m	Alpine meadow
BJ	31.37°N, 91.90°E	4509 m	Alpine meadow
MS3608	31.23°N, 91.78°E	4589 m	Alpine grassland

achieving the parameters on inhomogeneous surface in the plateau. The surface parameters can be retrieved by satellite data, and the new parameterization scheme from those data can be introduced in the numerical models [13]. Therefore, the accuracy of the prediction can be improved. Nevertheless, the data from satellites and models are all needed to be verified by the in situ observation data, so the meteorological observation stations on the Tibetan Plateau are essential for the weather and climate prediction.

2. Materials and Methods

2.1. Materials. As is shown in Figure 1, eight field weather stations [11, 16] spread along Qinghai-Tibet Railway and six of them are used in this paper. The characteristics of all stations are shown in Table 1 and the surface feature of the Northern Tibetan Plateau can be represented by the stations [16]. The elevations of these stations are all above 4500 meters; D66 and NewD66 stations are covered by alpine sparse grassland, located in north of the Northern Tibetan Plateau. The elevation of D105 station which is above 5000 m is the highest station among these stations. The experiment field in D105 station, covered by alpine meadows, is flat and wide, and some hills stand at the east of the field. Similarly,

the experiment field in NPAM station, covered by alpine meadows, which are 15 centimeters tall, is flat and wide, and there are hills that are 100–200 meters tall that are around the field. The experiment field in BJ station, covered by alpine meadows, is flat and broad. MS3608 station, located in south of the area and covered by alpine grassland, is relatively moist.

Data applied in this study come from the observational data of the six stations, D66, NewD66, DI05, NPAM, BJ, and MS3608. Daily meteorological data were obtained from the six stations and all these stations had complete records of meteorological factors from 2001 to 2013. The daily meteorological data included air temperature, land surface temperature, soil moisture, wind speed, and long-wave radiation. A few missing data (mainly in 2004, 2005 at BJ station) were estimated by averaging the value of other years observed at the same station.

2.2. Methods. Because of the poor quality data of land surface temperature observed, long-wave radiation data were used to calculate land surface temperature, and the formula is as follows:

$$R_{lw}^{\uparrow} = (1 - \varepsilon_s) R_{lw}^{\downarrow} + \varepsilon_s \sigma T_s^4, \quad (1)$$

where R_{lw}^{\uparrow} is the upward long-wave radiation, R_{lw}^{\downarrow} is the downward long-wave radiation, T_s is the land surface temperature, $\sigma = 5.67 \times 10^{-8} \text{ W} \cdot \text{m}^{-2} \text{ K}^{-4}$ is Boltzmann constant, and ε_s is land emissivity. From (1) we can see that T_s is affected by the upward long-wave radiation (R_{lw}^{\uparrow}), the downward long-wave radiation (R_{lw}^{\downarrow}), and land emissivity (ε_s). The influences of these three factors on T_s have been discussed in some researches [17, 18]. The upward and downward long-wave radiation in this study were measured by radiation instruments in all stations. ε_s of each station changes along with seasons. The influence of ε_s was considered in this study. Normalized differential vegetation index (NDVI) was applied to calculate ε_s in all sites, and the values were fluctuant from 0.92 to 0.98. This result is consistent with the conclusion drawn by He et al. [19]. The formula used for calculating ε_s was proposed by Van De Griend and Owe in 1993 [20]:

$$\varepsilon_s = 1.0094 + 0.047 \ln(\text{NDVI}). \quad (2)$$

In addition, the data quality of other factors was proved to be good for the study, so the observed data were used to analyze the long-term changes and climate prediction.

3. Results

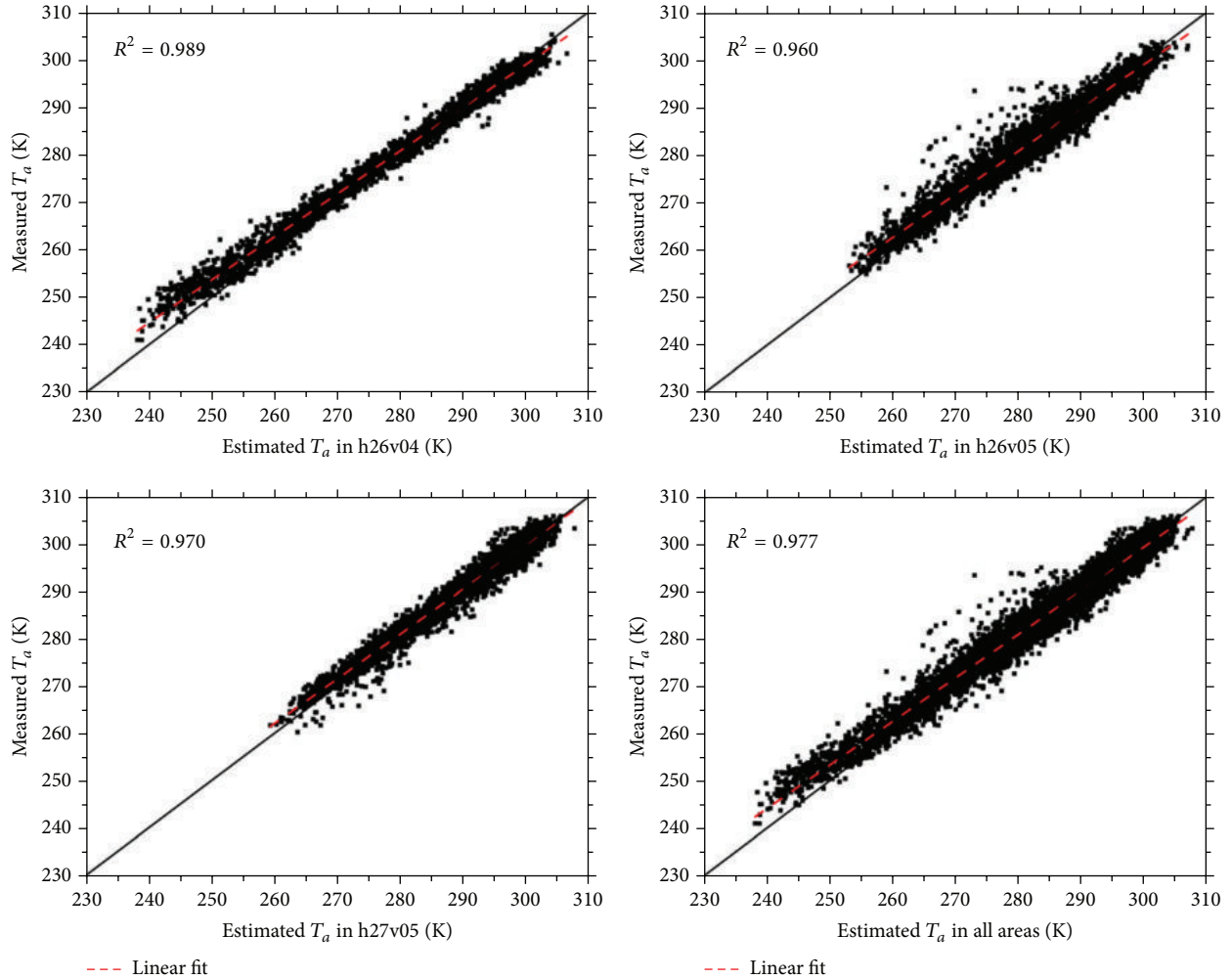
3.1. In Situ Measurements. Generally, the first-hand data for meteorology are provided by in situ measurements, and these data are widely used to validate the satellite data and model data for studying climate changes. For example, in situ measurements are compared with air temperature data estimated from the MODIS land surface data to verify the use of MODIS data for studying the spatial distribution of the air temperature by Sun et al. [21]. Three land areas covered by MODIS sinusoidal tile h26v04 (mountain area, average elevation 500–2000 meters), h26v05 (high mountain area, average elevation

2000–5000 meters), and h27v05 (plain area, average elevation 0–500 meters) were selected. Figure 2 shows the correlation of the estimated and measured air temperature. The in situ observations of air temperature are in good agreement with the estimated values from MODIS, with R^2 greater than 0.95 in all areas. In addition, the Mean Absolute Deviation (MAD) values of the estimated air temperature on the three areas are all lower than 2 K, and the Root-Mean-Square Error (RMSE) value in h27v05 area (1.84 K) is the lowest. According to Sun, the fact that the terrain in this area is relatively flat is the possible reason. This example has excellently shown that in situ measurements play a significant role in the validation of remote sensing data. And then, another example will prove the importance of weather station measurements for the weather and climate prediction. In recent years, it has been in the spotlight that numerical models are widely introduced to study the climate change, and hypotheses in models are based on observational facts. Radiosonde data can reflect the thermodynamic structure in the upper air. For example, Boos and Kuang [22] considered that the dominant control of the South Asian monsoon was the orographic insulation, and they demonstrated the hypothesis using numerical models. Before building the hypothesis and testing the models, radiosonde data were used to analyze the thermodynamic structure in the upper air. As is shown in Figure 3, the thermodynamic structure over Indian and Tibetan stations was accurately analyzed. Figure 3(a) shows the equivalent potential temperature within 25 hPa of the surface at radiosonde sites over and around the Tibetan Plateau. Figure 3(b) presents the daily mean profiles of temperature. Dashed lines are dry adiabats from the lowest sounding level up to the lifted condensation level and moist pseudoadiabats thereafter. Figure 3(c) represents the mean temperature difference between the Indian and Tibetan Plateau sites, with positive values denoting air that is warmer over Indian sites. The atmospheric conditions in the upper air were accurately analyzed by observational data, and reasonable hypotheses could be proposed. Based on the meteorological observation, the numerical simulated results are more dependable and accurate for the weather forecasting and climate prediction.

3.2. Long-Term Meteorological Observations. As shown in Table 2, the land surface temperature (T_s) and air temperature (T_a) in all stations show uptrend along with time, except for T_s in NPAM in autumn, which show a decreasing trend with the seasonal rate 0.07°C . In NewD66 and DI05, the annual increase rates of T_s are greater than that of T_a , and it means that the uptrend of T_s is more obvious than that of T_a in the north part of the Northern Tibetan Plateau. In spring and winter, the increasing trends of T_s are more obvious, while, in summer and autumn, the rising trends of T_a are greater than that of T_s . In BJ and MS3608, which are located in the south part of the Northern Tibetan Plateau, the annual increase rates of T_a are greater than that of T_s . The uptrends of T_a are remarkable in spring and summer, and the rising tendency of T_s and T_a in BJ is more apparent than that in MS3608. However, in NPAM, the annual increasing rates of T_s and T_a are both $0.01^\circ\text{C}/\text{a}$, and the warming trend

TABLE 2: The annual and seasonal linear trend of T_s and T_a in all sites.

	Annual		Spring		Summer		Autumn		Winter	
	T_s	T_a								
NewD66	0.12	0.03	0.11	0.04	0.02	0.08	0.01	0.08	0.09	0.03
D105	0.12	0.02	0.04	0.02	0.02	0.09	0.07	0.09	0.05	0.01
NPAM	0.01	0.01	0.01	0.02	0.01	0.07	-0.07	0.05	0.01	0.01
BJ	0.07	0.10	0.07	0.14	0.03	0.13	0.002	0.07	0.11	0.07
MS3608	0.01	0.03	0.02	0.06	0.06	0.10	0.03	0.01	0.01	0.01

FIGURE 2: Comparisons between the estimated and measured T_a values in three case study areas covered by the MODIS tiles h26v04, h26v05, and h27v05. (The figure is cited from Sun et al. [21].)

is not obvious compared with other stations. According to IPCC5 and some studies [23–25], the global averaged surface temperature shows a warming of 0.85°C over the period 1880–2012, and over the past 60 years the rate of warming is $0.12^\circ\text{C}/10\text{a}$. Since 2001, the increasing rate of T_a in these stations is between $0.1^\circ\text{C}/10\text{a}$ and $1.0^\circ\text{C}/10\text{a}$, which means that the warming rate in the Northern Tibetan Plateau is greater than that in global areas.

Take BJ station as an example. Figure 4 shows the interannual variations of annual mean T_s and T_a in different seasons.

As shown in the figure, the annual increasing rates of T_s and T_a are $0.07^\circ\text{C}/\text{a}$ and $0.10^\circ\text{C}/\text{a}$, separately. T_s and T_a have been climbing since 2001, and the change trend of T_a always keeps pace with that of T_s , but the uptrend of T_a is more obvious than that of T_s . The warming rate of BJ is $1.0^\circ\text{C}/10\text{a}$ since 2001, which is almost ten times compared to that in global range. The seasonal rising rates of T_s are 0.07°C , 0.03°C , 0.002°C , and 0.11°C , respectively, in spring, summer, autumn, and winter, while those of T_a are 0.14°C , 0.13°C , 0.07°C , and 0.07°C . The air temperatures show warming trend in all seasons,

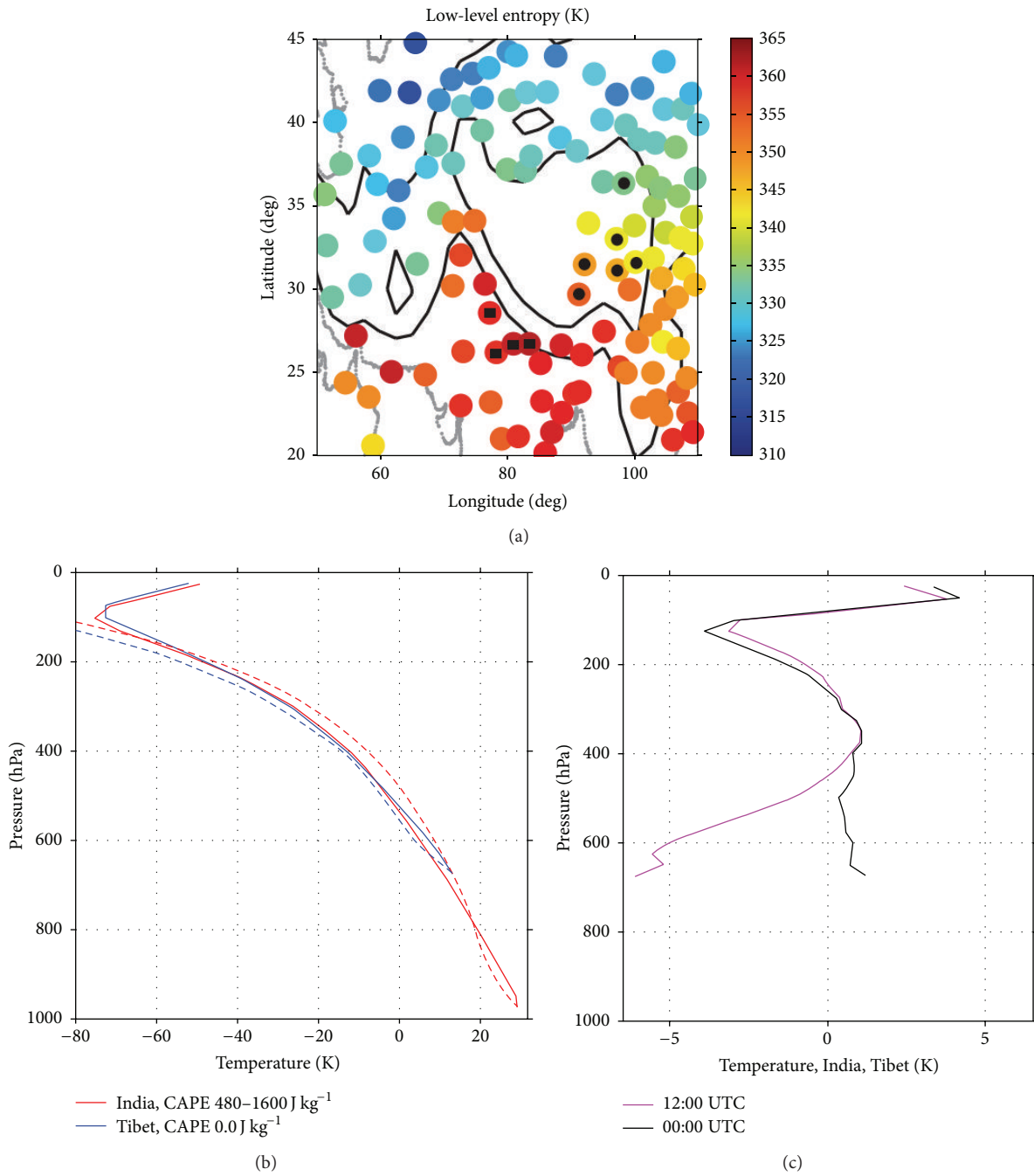


FIGURE 3: Thermodynamic structure from balloon soundings for June–August. (The figure is cited from Boos and Kuang [22].)

especially in spring and summer, while the land surface temperatures are rising in spring, summer, and winter, and T_s in autumn remains unchanged. Moreover, the rising trend of T_s is more obvious in winter. The increasing rate of T_s in winter is greater than that in summer, while the rising trend of T_a in summer is more remarkable than that in winter. On the other hand, the values of T_s are always greater than that of T_a , except for several winters. It indicates that the land surface is a long-term heat source for the atmosphere. Similarly, Figure 5 shows the interannual variations of annual mean

wind speed and soil moisture in each season. By comparing Figures 4 and 5, the impacts of wind speed and soil moisture on temperatures are revealed. In the winter of 2006, both T_s and T_a reached their maximum values -7.38°C and -8.13°C , while the value of wind speed was the greatest and the soil moisture value was the lowest. In 2008, the values of T_s and T_a were down to the bottom, especially in summer and autumn. Meanwhile, the value of wind speed was lower than the average value and the soil moisture value was greater than its mean value. It can be seen from the analysis that the changes

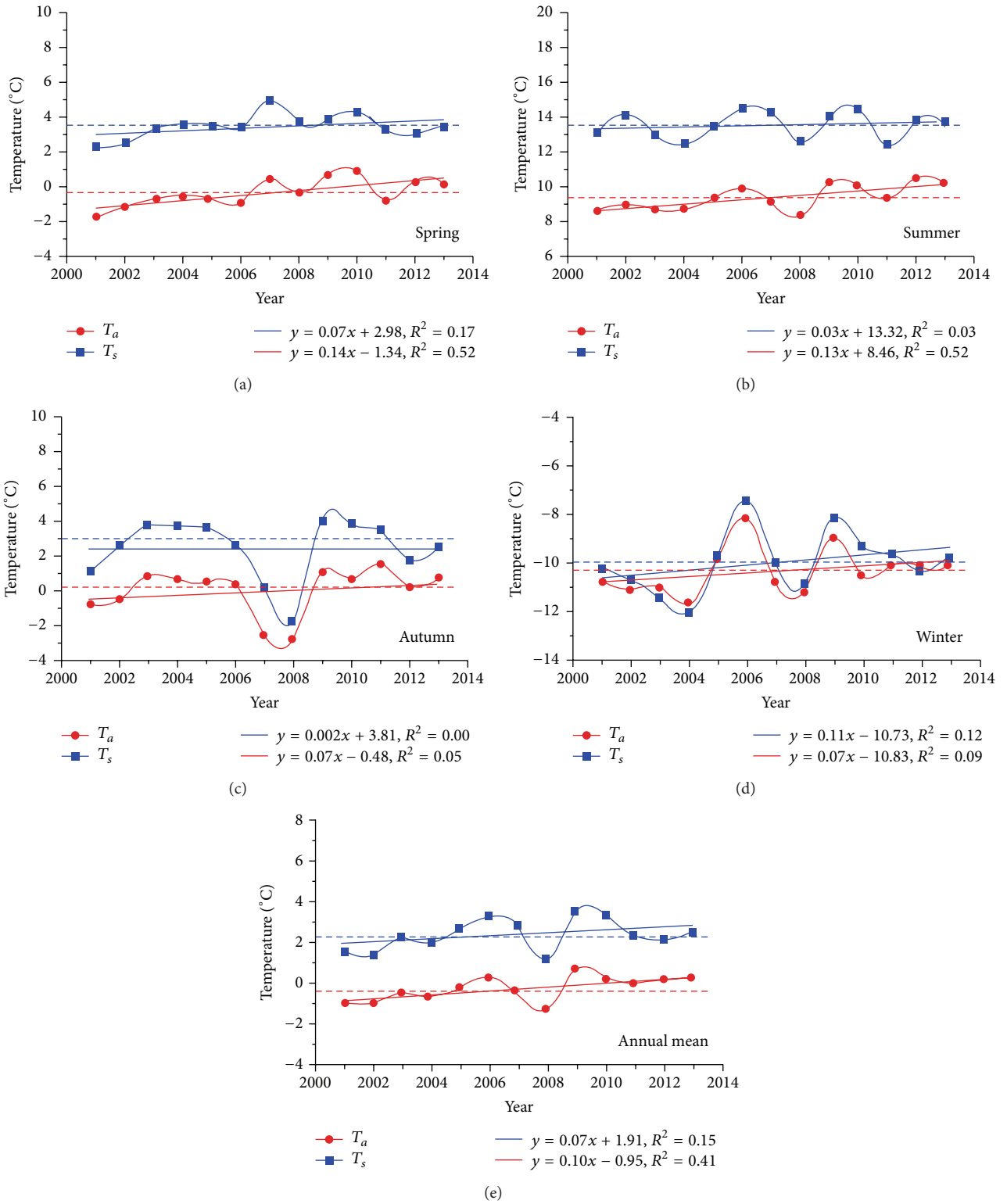


FIGURE 4: Averaged land surface temperature and air temperature change curves for seasons and years at BJ (curved lines are observed values, and straight lines are liner trend).

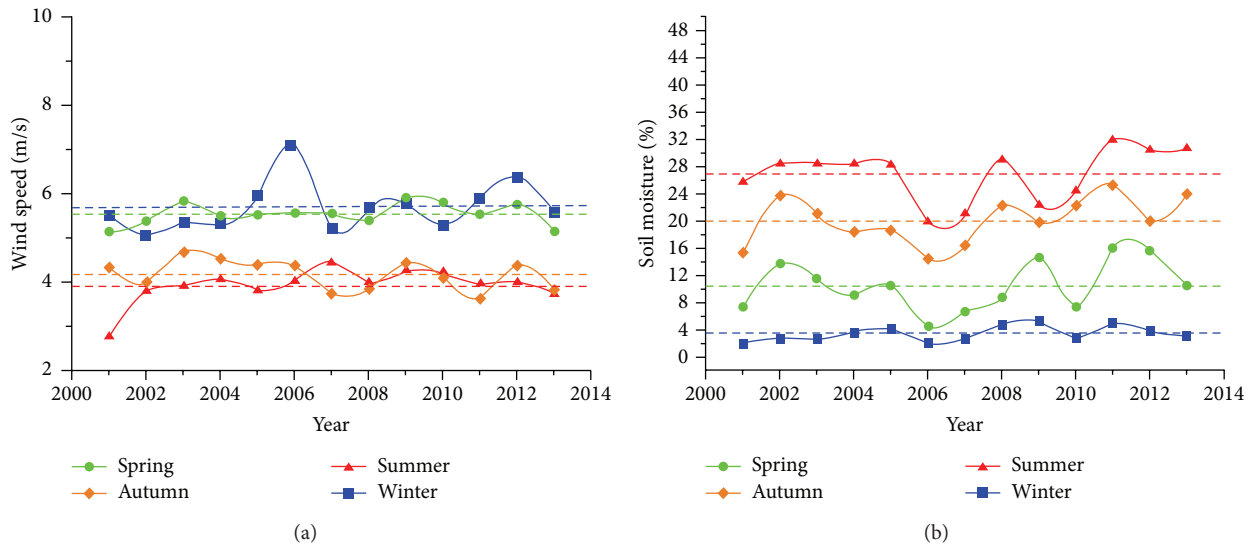


FIGURE 5: The interannual variation of wind speed and soil moisture in each season at BJ.

of wind speed and soil moisture make the difference to the temperatures on the Tibetan Plateau.

In addition, according to some researches [26, 27], El Nino and La Nina phenomenon separately occurred in 2006 and 2008. Based on some analysis [28], the surface heating field in the Tibetan Plateau has an increasing trend in El Nino year and weakens in La Nina year. Based on the above analysis, in El Nino year, the values of T_s , T_a and wind speed are greater than the averaged values, and the soil moisture values are lower than the averaged, while in La Nina year, the values of T_s , T_a and wind speed are less than the averaged values, and the soil moisture values are greater than the averaged. The variation of the previous surface heating field is a strong signal for the prediction of summer drought-flood anomalies at the east side of the Tibetan Plateau [29, 30]. It is thus clear that long-term observations in the Tibetan Plateau exert an important influence on the regional and global climate prediction.

3.3. Daily Observations at Different Sites. For the sake of monitoring the weather changes, a number of autoweather stations (AWSs) were set up in the Tibetan Plateau. Figure 6 shows the diurnal variations of T_s and T_a in D105, NPAM, and BJ stations mentioned in part 2, three stations in the Northern Tibetan Plateau. As can be seen from the figure, the variation trends are similar at all sites. T_s and T_a change significantly from daytime to nighttime; the fluctuation is larger in daytime than that in nighttime. Averagely, T_s reaches the peak value at 14:00, while T_a gets the maximum at 16:00–18:00. Obviously, the T_a diurnal variation falls behind T_s , and it is closely bound up with the solar radiation. Furthermore, the diurnal variation is various in different seasons, and what causes the differences may be the East and South Asian monsoon. The land surface in the plateau is relatively dry with less cloud cover and increasing solar radiation in spring, which is before the summer monsoon onset, so the surface

is cooled rapidly during the night and heated fast during the day. It can explain why the temperatures get the greatest diurnal change in spring. With precipitation increasing more, the soil moisture is growing in summer and autumn, which are after the monsoon onset, and the temperatures diurnal variation is the lowest. Besides, the changes are different in different latitudes and underlying surfaces. The diurnal variation and difference of T_s and T_a in D105, which is mainly covered by marsh, are less than that of NPAM and BJ with grassy marshland. The effect of T_a lagging behind T_s can give some information for the daily maximum air temperature forecast.

The process of making weather forecast consists of observation, data acquisition, data processing, data analysis, and forecast. All of them are based on the observation, and surface observation is absolutely necessary and it provides initial and reference value for the numerical forecasting. It is obvious that daily observation has an effect on weather forecast in the Northern Tibetan Plateau.

4. Conclusions

The underlying surface in the Tibetan Plateau is complex and heterogeneous, and it makes all the difference to the East Asian and even global climate change. So based on the in situ measurements, weather and climate prediction is dependable and convincing. As the first-hand data, data from weather stations are widely used to validate the satellite data and model data for studying climate changes. And in situ measurements are essential to the climate and weather forecast.

Long-term observations in the Tibetan Plateau exert an important influence on the regional and global climate prediction. In the Northern Tibetan Plateau, T_s and T_a have been climbing since 2001, and the change trend of T_a always keeps pace with that of T_s , but the uptrend of T_a is more obvious than that of T_s , especially in spring. Compared with

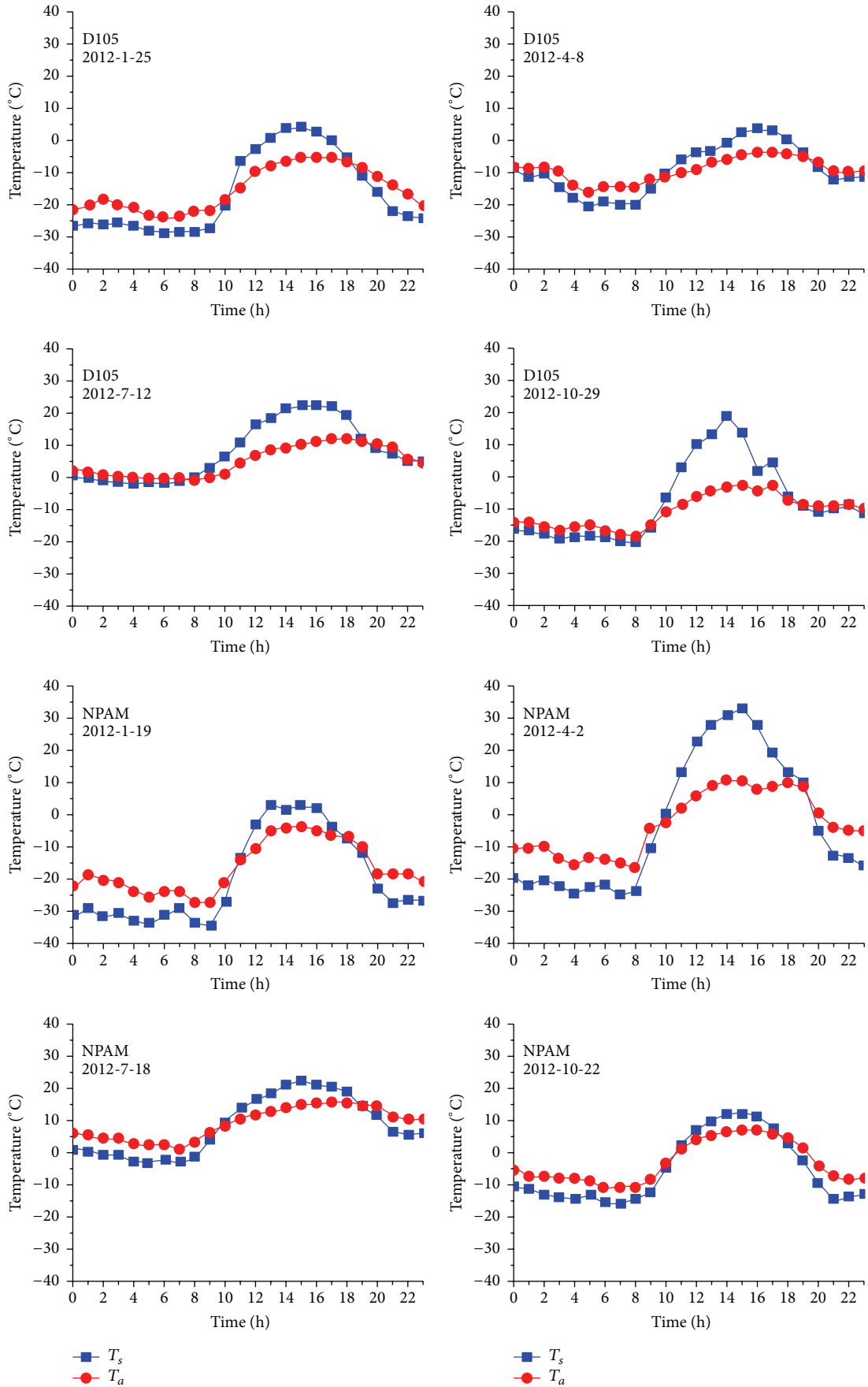


FIGURE 6: Continued.

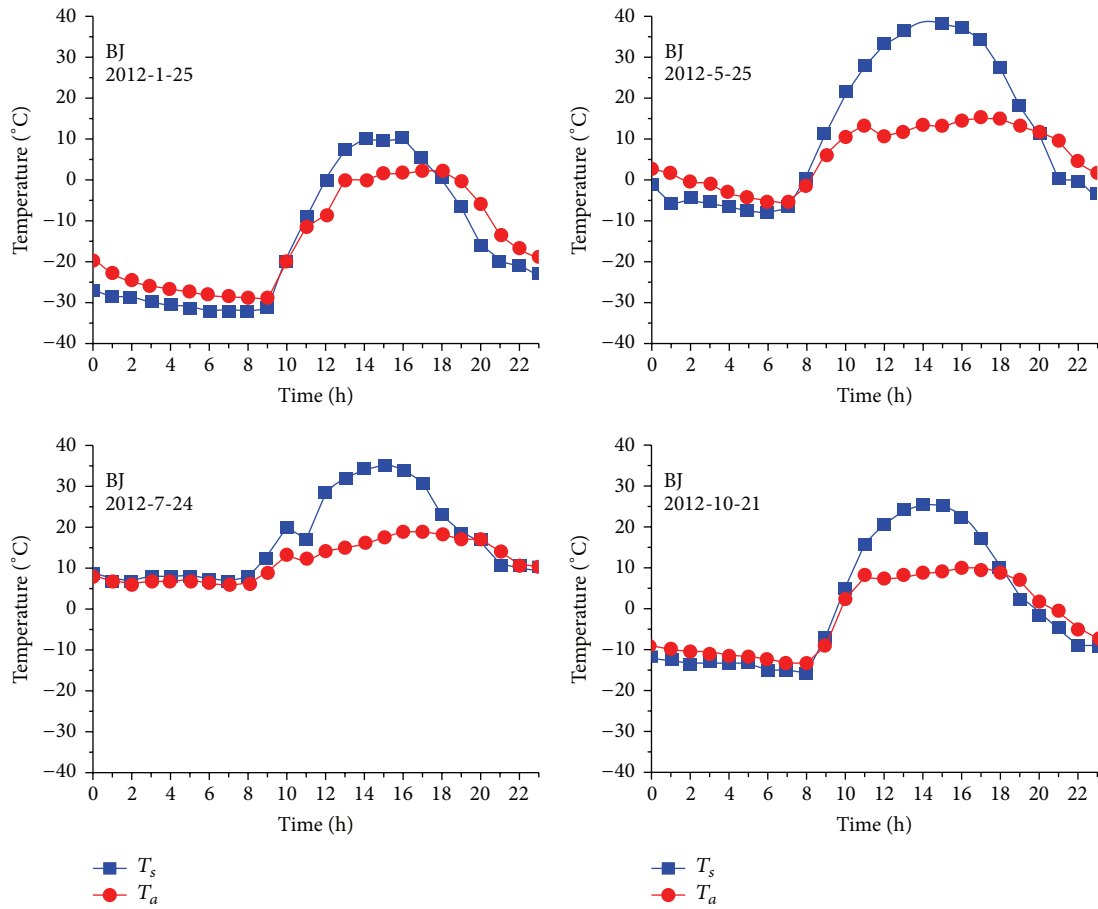


FIGURE 6: The diurnal variation of land surface temperature (T_s) and air temperature (T_a) in typical clear days in different seasons at D105/NPAM/BJ.

the global warming rate with $0.12^{\circ}\text{C}/10\text{a}$ over the past 60 years, the warming rate in the Northern Tibetan Plateau over the past ten years is greater than that in global areas. In El Nino year, the values of T_s , T_a and wind speed are greater than the averaged values, and the soil moisture values are lower than the averaged, while the contrary is the case in La Nina year.

The daily variations of T_s and T_a at all sites have similar trend, with obvious changes in the daytime and no significant changes in the nighttime. T_a changes lag behind that of T_s . The diurnal variations of T_s and T_a are the greatest in spring and are less in summer and autumn. The diurnal variation in the area with drier underlying surface is more obvious than that in the area with moist surface.

According to these observations, amount of weather and climate research in the plateau can be done continuously. As the foundation of climate prediction, long-term meteorological observations are worthy to be paid more attention.

Conflict of Interests

The authors declare no conflict of interests.

Acknowledgments

This study was funded by CAS “Hundred Talent” program (Dr. Weiqiang Ma), National Natural Science Foundation of China (NSFC) (41375009, 91337212, 41275010, and 41275028). Special thanks are given to the anonymous reviewers and the editor for very constructive comments. The authors also thank all the participations for their very hard field work during the field observations in Tibetan Plateau.

References

- [1] D. Ye and Y. Gao, *Meteorology of Qinghai-Xizang Plateau*, Chinese Science Press, Beijing, China, 1979.
- [2] Y. Duzheng, “The progress of atmosphere science research in China in recent years,” *Scientia Atmospherica Sinica*, vol. 3, no. 3, pp. 195–202, 1979.
- [3] G. Wu and Y. Zhang, “Tibetan Plateau forcing and the timing of the monsoon onset over South Asia and the South China Sea,” *Monthly Weather Review*, vol. 126, no. 4, pp. 913–927, 1998.
- [4] P. Zhao and L. Chen, “Climatic features of atmospheric heat source/sink over the Qinghai-Xizang Plateau in 35 years and its

- relation to rainfall in China,” *Science in China, Series D: Earth Sciences*, vol. 44, no. 9, pp. 858–864, 2001.
- [5] Z. Jijia, Z. Baozhen, Z. Fukang et al., *Advances on Qinghai-Xizang Plateau Meteorology Research*, Chinese Science Press, Beijing, China, 1988.
 - [6] Z. Qian and Y. Jiao, “Advances and problems on Qinghai-Xizang plateau meteorology research,” *Advances in Earth Sciences*, vol. 12, no. 3, pp. 207–216, 1996.
 - [7] G. Ji, L. Yao, F. Yuan et al., “The characteristics of the surface and atmospheric heating fields over the Qinghai-Xizang Plateau in winter of 1982,” *Chinese Sciences (B)*, no. 3, pp. 214–224, 1986.
 - [8] G. Ji, M. Pu, and Y. Xi, “The characteristics of the surface and atmospheric heating fields over the Qinghai-Xizang Plateau in summer of 1983,” *Plateau Meteorology*, vol. 5, no. 2, pp. 155–166, 1986.
 - [9] J. I. Guoliang, G. U. Benwen, and L. V. Lanzhi, “Characteristics of atmospheric heating field over Northern Qinghai-Xizang plateau,” *Plateau Meteorology*, vol. 21, no. 3, pp. 238–242, 2002.
 - [10] X. Xu and L. Chen, “Advances of the study on Tibetan Plateau experiment of atmosphere sciences,” *Journal of Applied Meteorology*, vol. 17, no. 6, pp. 758–772, 2006.
 - [11] Y. Ma, T. Yao, and J. Wang, “Experimental study of energy and water cycle in Tibetan Plateau—the progress introduction on the study of GAME/Tibet and CAMP/Tibet,” *Plateau Meteorology*, vol. 25, no. 2, pp. 344–351, 2006.
 - [12] Y. Ma, L. Zhong, Z. Su, H. Ishikawa, M. Menenti, and T. Koike, “Determination of regional distributions and seasonal variations of land surface heat fluxes from Landsat-7 Enhanced Thematic Mapper data over the central Tibetan Plateau area,” *Journal of Geophysical Research D: Atmospheres*, vol. 111, no. 10, Article ID D10305, 2006.
 - [13] M. Wenbin and L. Bin, “Review and prospect on the application of meteorological satellite data over Tibetan Plateau in the past 20 years,” *Plateau and Mountain Meteorology Research*, vol. 31, no. 3, pp. 83–88, 2011.
 - [14] M. Abe, A. Kitoh, and T. Yasunari, “An evolution of the Asian summer monsoon associated with Mountain uplift—simulation with the MRI atmosphere-ocean coupled GCM,” *Journal of the Meteorological Society of Japan*, vol. 81, no. 5, pp. 909–933, 2003.
 - [15] G. Wu, Y. Liu, B. He, Q. Bao, A. Duan, and F.-F. Jin, “Thermal controls on the Asian summer monsoon,” *Scientific Reports*, vol. 2, article 404, 2012.
 - [16] M. Weiqiang, M. Yaoming, L. Maoshan et al., “Seasonal variation on land surface energy budget and energy balance components in the Northern Tibetan Plateau,” *Journal of Glaciology and Geocryology*, vol. 27, no. 5, pp. 673–679, 2005.
 - [17] M.-F. Huang, X.-F. Xing, S.-H. Liu, and S.-M. Liu, “Study on the method obtaining the three elements for the retrieval of the surface temperature based on infrared radiometer,” *Arid Land Geography*, vol. 28, no. 4, pp. 541–547, 2005.
 - [18] L. Chao, W. Heli, L. Houtong et al., “Effect of downwelling atmospheric radiation on grass land surface temperature,” *Journal of Atmospheric and Environmental Optics*, vol. 3, no. 6, pp. 407–414, 2008.
 - [19] W. He, H. Chen, Q. Sun, and M. Wang, “The characteristics of microwave surface emissivity over Tibetan plateau,” *Remote Sensing Technology and Application*, vol. 26, no. 6, pp. 735–741, 2011.
 - [20] A. A. Van De Griend and M. Owe, “On the relationship between thermal emissivity and the normalized difference vegetation index for natural surfaces,” *International Journal of Remote Sensing*, vol. 14, no. 6, pp. 1119–1131, 1993.
 - [21] H. Sun, Y. Chen, A. Gong, X. Zhao, W. Zhan, and M. Wang, “Estimating mean air temperature using MODIS day and night land surface temperatures,” *Theoretical and Applied Climatology*, vol. 118, no. 1–2, pp. 81–92, 2014.
 - [22] W. R. Boos and Z. Kuang, “Dominant control of the South Asian monsoon by orographic insulation versus plateau heating,” *Nature*, vol. 463, no. 7278, pp. 218–222, 2010.
 - [23] IPCC, *Fifth Assessment Report, Climate Change 2013: The Physical Science Basis: Summary for Policymakers*, IPCC, 2013.
 - [24] Q. Dahe and T. Stocker, “Highlight of the IPCC working group I fifth assessment report,” *Progressus Inquisitiones de Mutatione Climatis*, vol. 10, no. 1, pp. 1–6, 2014.
 - [25] S. Yongping and W. Guoya, “Key findings and assessment results of IPCC WGI fifth assessment report,” *Journal of Glaciology and Geocryology*, vol. 35, no. 5, pp. 1068–1076, 2013.
 - [26] Y.-Y. Sun, J.-Y. Liu, H.-F. Tsai, C.-H. Lin, and Y.-H. Kuo, “The equatorial El Nino-Southern oscillation signatures observed by FORMOSAT-3/COSMIC from July 2006 to January 2012,” *Terrestrial, Atmospheric and Oceanic Sciences*, vol. 25, no. 4, pp. 545–558, 2014.
 - [27] F. Zheng and J. Zhu, “Roles of initial ocean surface and subsurface states on successfully predicting 2006–2007 El Niño with an intermediate coupled model,” *Ocean Science*, vol. 11, no. 1, pp. 187–194, 2015.
 - [28] L. Dongliang, H. Jinhai, T. Xu et al., “The relationship between the intensity of surface heating fields over the Qinghai-Xizang plateau and ENSO cycle,” *Plateau Meteorology*, vol. 26, no. 1, pp. 39–46, 2007.
 - [29] C. Wen, “Impacts of El Nino and La Nina on the cycle of the East Asian winter and summer monsoon,” *Chinese Journal of Atmospheric Sciences*, vol. 26, no. 5, pp. 595–610, 2002.
 - [30] C. Hongbin and F. Xuehua, “Some extreme events of weather, climate and related phenomena in 2008,” *Climatic and Environmental Research*, vol. 14, no. 3, pp. 329–340, 2009.

Research Article

Distribution of Atmospheric Aerosol over the South China Sea

Shih-Jen Huang and Chen-Chih Lin

Department of Marine Environmental Informatics, National Taiwan Ocean University, Keelung, Taiwan

Correspondence should be addressed to Shih-Jen Huang; huangsj@mail.ntou.edu.tw

Received 15 May 2015; Revised 27 June 2015; Accepted 5 July 2015

Academic Editor: Yuriy Kuleshov

Copyright © 2015 S.-J. Huang and C.-C. Lin. This is an open access article distributed under the Creative Commons Attribution License, which permits unrestricted use, distribution, and reproduction in any medium, provided the original work is properly cited.

The satellite-derived aerosol optical depth (AOD) data is used to investigate the distribution of aerosol over the South China Sea (SCS). High correlation coefficients are found between in situ AERONET data and satellite AOD measurements around the SCS with the highest coefficient of 0.9 on the Dongsha Island (i.e., Pratas Island). The empirical orthogonal function (EOF) analysis of AOD over the SCS shows that high AOD is always found around offshore areas of China, Indochina, Sumatra, and Borneo. Besides, spring is the major season of occurring coarse aerosol particles (AOT_C) but fine aerosol particles (AOT_F) occur yearly. The biomass burning is found in Indochina during March and April, and so it is in Sumatra and Borneo from August to October. The results also show that the AOT_F are higher during El Niño events, but higher AOT_C are found in La Niña years.

1. Introduction

The South China Sea (SCS) is not only the largest marginal sea of the Pacific in Southeast Asia but also abundant with marine resources. It covers an ocean area from the equator to 22°N and from 100°E to 121°E with a bathymetry deeper than 3000 m in the center and the north. It is also a major sea route connecting the Pacific Ocean to the Indian Ocean (Figure 1). The SCS, located within the East Asian monsoon region [1–4], confronts the prevailing northeaster carrying dust mixed with anthropogenic aerosols during the winter monsoon season from November to April. In the summer monsoon season from June to September, the smoke particles associated with biomass burning in Borneo and Sumatra are transported to the southern SCS [5].

Over the SCS, most of the aerosols come from Mainland China, Indochina Peninsula, and Luzon Island. Besides, the other origin of aerosols is the biomass burning from Sumatra and Borneo in Indonesia from August to October [6]. A vast amount of aerosol, attributed to varied emissions (e.g., dust, anthropogenic, and biomass burning) from the Asian continent, has widely impacted on the ecosystem [7]. On March 19–21, 2010, a significant Asian dust storm affected large areas from the Gobi deserts to the West Pacific Ocean and southern China [8]. The airborne dust over the Central Asia can be

identified by analyzing the satellite data due to the features of coarse and fine particles [9]. Wang et al. [10] measured the Asian dust and found that it can be further transported and sunk to the northern SCS during the springtime. Reid et al. [11] found that large aerosol events that happened in SCS are almost always associated with biomass burning. Indochina fire smoke is transported out over the Pacific Ocean and beyond during the winter monsoon period. The biomass-burning aerosols were transported over the northern and eastern Southeast Asia [12]. Atwood et al. [13] showed that the El Niño event enhanced tropical burning. The seasonal winds at 850 hpa transport the burning smoke from source regions (Maritime Continent) to the southwest of Singapore during the summer monsoon. Wang et al. [14] showed that the dry conditions associated with the El Niño event cause the largest regional biomass burning outbreak. The smoke was widely spread over the 5°S–5°N zone during the seasonal monsoonal transition period.

From previous studies above-mentioned, the aerosol variations over the SCS may be affected by monsoon and large scale atmospheric circulation. Therefore, to more understand the changes of spatial distribution and time series of aerosol over the SCS, the satellite base aerosol optical depth (AOD) data are analyzed thoroughly.

TABLE 1: The mean of Aeronet AOD, root-mean-square-error (RMSE), and correlation coefficient (R) between monthly MODIS AOD and Aeronet AOD 500 nm.

Aeronet St.	Location	Data period	Mean	RMSE	R
Dongsha	(116.729°E, 20.699°N)	2009/09~2010/05	0.286	0.078	0.91
Mukdahan	(104.676°E, 16.607°N)	2003/11~2009/12	0.360	0.157	0.70
Pimai	(102.564°E, 15.182°N)	2003/02~2008/04	0.355	0.116	0.81
Hong Kong	(114.180°E, 22.303°N)	2005/11~2010/01	0.528	0.153	0.70
Bac Lieu	(105.730°E, 9.280°N)	2006/05~2009/02	0.218	0.215	0.52
Singapore	(103.780°E, 1.298°N)	2006/11~2010/05	0.338	0.180	0.24

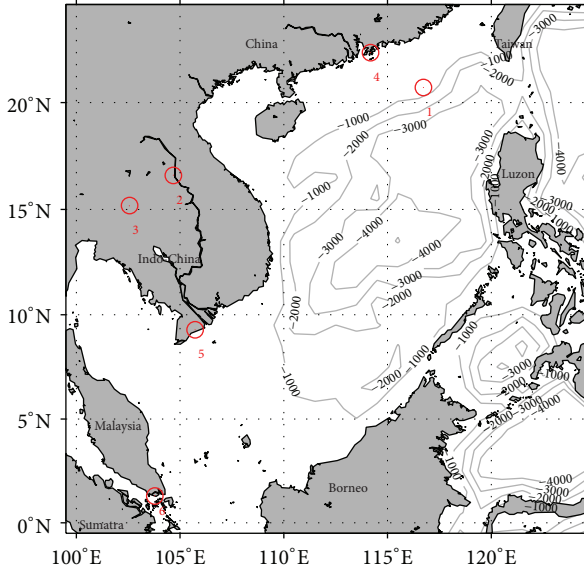


FIGURE 1: A map of SCS with isobaths. The circle represents Aeronet observation station, 1: Dongsha, 2: Mukdahan, 3: Pimai, 4: Hong Kong, 5: Bac Lieu, and 6: Singapore.

2. Data and Methodology

The AOD and fine mode fragment (FMF) at 500 nm, proved by the National Aeronautics and Space Administration (NASA) Terra Moderate Resolution Imaging Spectroradiometer (MODIS) Level 3 satellite data from January 2001 to December 2012, are used in this study. The MODIS AOT data are masked when there are clouds. Therefore, no AOT value can be used during overcast days. Those data are then monthly averaged and the spatial resolution is 1° latitude by 1° longitude. The study area is located from the equator to 25°N and from 100°E to 125°E (Figure 1). Besides, the monthly in situ data from Aeronet observation stations around the SCS is also used in this study. To examine the relationship between MODIS AOD data and in situ Aeronet measurements, the correlation coefficient (R) and root mean square error (RMSE) at each station are computed and presented in Table 1. Except Singapore and Bac Lieu of Vietnam stations, the stations have a higher correlation coefficient (larger than 0.7). The values of RMSE between MODIS AOD and Aeronet AOD at each station are smaller than the mean of those of Aeronet AOD implying that it

can be used for the study of analyzing temporal and spatial variations of aerosol over the SCS. The AOD data are further divided into coarse mode aerosol (AOT_C) and fine mode aerosol (AOT_F) by FMF data as

$$\begin{aligned} \text{AOT_F} &= \text{AOD} \times \text{FMF}, \\ \text{AOT_C} &= \text{AOD} \times (1 - \text{FMF}). \end{aligned} \quad (1)$$

In order to analyze the spatial and temporal variations of aerosol, the empirical orthogonal function (EOF) and the fast Fourier transform (FFT) analyses are used. The error of EOF analysis, e , is estimated by the method of North et al. [15] as

$$e = \lambda_k \sqrt{\frac{2}{N}}, \quad (2)$$

where λ_k is the eigenvalues of covariance matrix at the k th mode and N is the degree of freedom.

It is known that the activities of El Niño and La Niña may affect the atmospheric and oceanic environments; their effects are taken into account in this study. The Oceanic Niño Index (ONI) constructed with the SST anomalies in the Niño 3.4 region (5°N - 5°S , 120°W - 170°W) is used as the indicator in judging whether El Niño or La Niña phenomena are present. If the ONI value is larger than 0.5, it is categorized as an onset of El Niño. If the value is smaller than -0.5 , it is classified as the time of La Niña events. It is deemed to be normal year if the value is between -0.5 and 0.5.

3. Results and Discussion

3.1. Coarse Mode Aerosol Variation. The EOF analysis of AOT_C data has been performed. The contributions of eigenvalues and typical errors of first five modes are illustrated in Table 2. The errors of the EOF mode 4 and mode 5 overlap each other. Therefore, only the first three EOF modes with the cumulative variance over than 84% are discussed as follows.

The EOF mode 1 (EOF1) of the AOT_C is shown in Figure 2. Both the spatial distribution and the temporal amplitude are negative, which cause the result of positive sum. The higher negative value represents the higher AOT_C. Figure 2(a) shows a larger amount of AOT_C occurring in the coastal area of southern China and the Indochina Peninsula. On the temporal distribution of Figure 2(b), no periodic signal is found. In TEOF1 (Figure 2(b)), the larger amplitude appears in March or April normally, but not in every year. For example, in March 2006, April 2009, and

TABLE 2: The contribution of eigenvalue at each EOF mode of AOT_C.

EOF mode	Contributing to variance (typical errors) (%)	Cumulative variance (%)
1	79.42 (69.17~89.67)	79.42
2	3.82 (3.33~4.31)	82.24
3	1.97 (1.71~2.22)	84.21
4	1.05 (0.91~1.18)	85.26
5	0.94 (0.82~1.06)	86.20

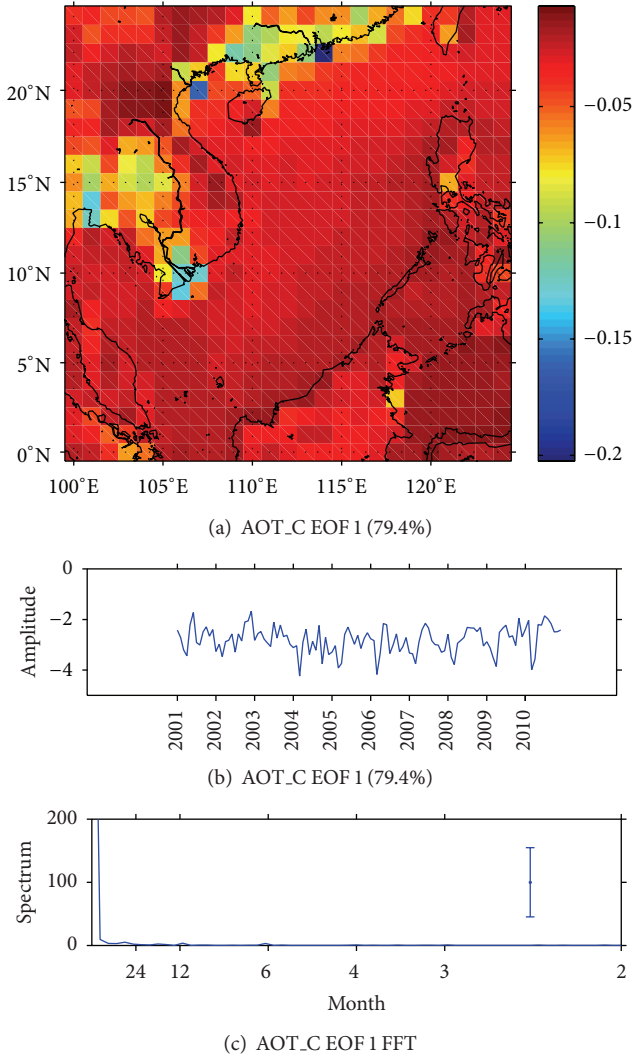


FIGURE 2: (a) The spatial distribution, (b) its corresponding time-varying amplitude for the vector EOF analysis mode 1 of the AOT_C in SCS during 2001/1–2010/12, and (c) the spectrum of (b) with FFT. The line segment represents the 95% confidence interval.

March 2010, the higher value of AOT_C was also obtained at Hong Kong AERONET station. Correspondingly, according to the studies of Tsay et al. [7] and Wang et al. [10], the Asia dust storms usually rage in spring, and the dust would be transported far to the SCS. This means that EOF1 displays

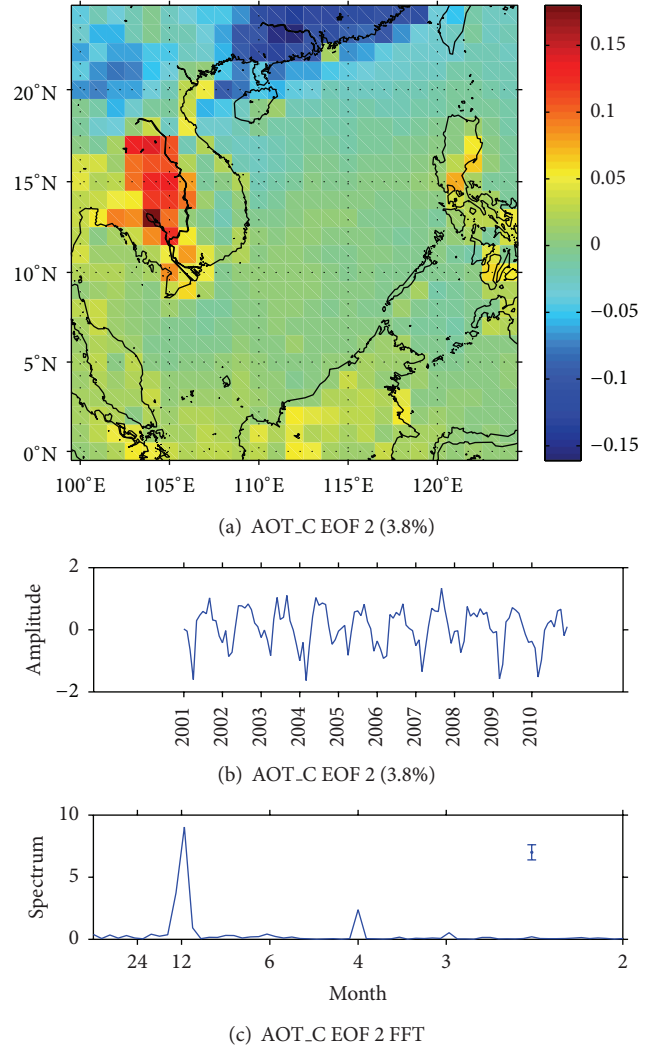


FIGURE 3: The same as Figure 2 but EOF mode 2 of AOT_C.

the random effect of whether accidental wildfires, sandstorm, or agricultural land development.

The result of EOF mode 2 (EOF2) of the AOT_C is shown in Figure 3. The spatial distribution in the Indochina Peninsula appears to have a positive value, but it is negative in southern China (Figure 3(a)). Meanwhile, the amplitude is positive from May to October with a maximum in September, while the negative amplitude appears from November to next April with a peak in January (Figure 3(b)). In other words, the AOT_C value in the Indochina Peninsula is higher than the average from May to October. Similarly, in southern China, the AOT_C value keeps higher during November and next April, and the maximum negative value appears in March.

The spatial distribution of EOF mode 3 (EOF3) displays that the positive value expands from the northwestern Indochina to its southeastern regions and the negative value is located in southern China (Figure 4(a)). The time series of EOF3 shows the positive value of amplitude from March to July, but the negative one from October to next February (Figure 4(b)). The spectrum analysis shows that the variation

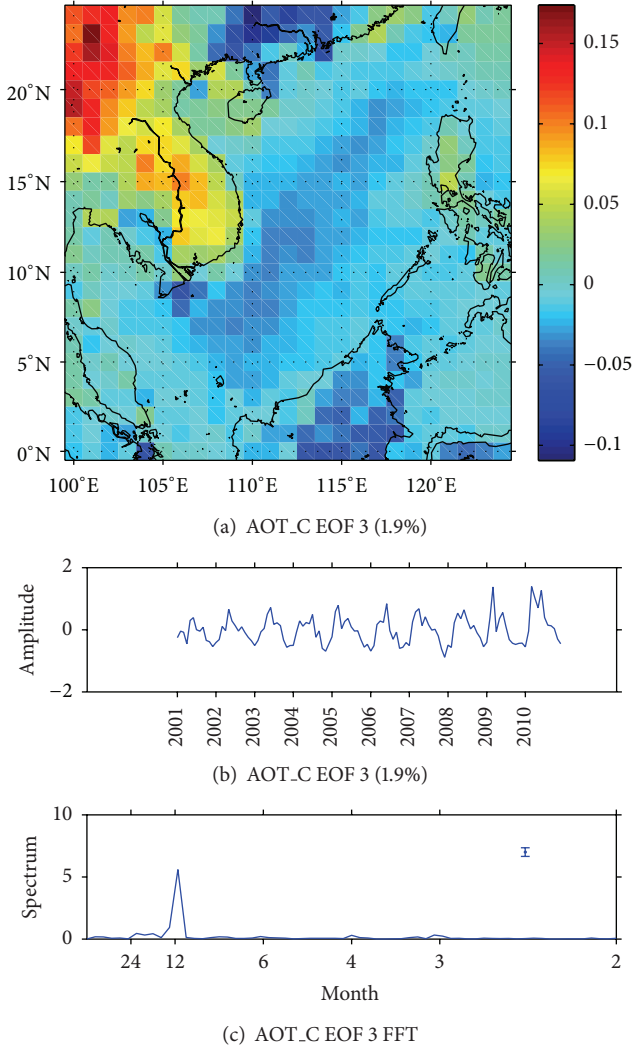


FIGURE 4: The same as Figure 2 but EOF mode 3 of AOT_C.

is yearly, but there is less energy than mode 1 and mode 2. As the result of mode 3, in the Indochina Peninsula, the AOT_C keeps higher during March and July. Figures 3(c) and 4(c) show the annual cycle regularly. Meanwhile, the coarse aerosol might erupt with the monsoon.

Consequently, there is a coincidence between the occurrence of high-value AOT_C and the high-value AOD observed at Aeronet observatories. The result indicates that the coarse aerosol particles mainly come from China and the Indochina Peninsula and occur annually. It corresponds to the previous studies [7, 8, 10].

3.2. Fine Mode Aerosol Variation. Through the EOF analysis, the first five modes of AOT_F data are dealt with through the typical error analysis and are shown in Table 3, which contains the contribution of eigenvalues and typical errors of each EOF mode of AOT_F. The fifth mode and the sixth one overlap each other in typical error range, and the fourth mode only accounts for the variance amount of 2.19% where only the first three modes are discussed.

TABLE 3: The contribution of eigenvalue at each EOF mode of AOT_F.

EOF mode	Contributing to variance (typical errors) (%)	Cumulative variance (%)
1	70.4 (61.32~79.49)	70.40
2	11.90 (10.37~13.44)	82.30
3	3.11 (2.71~3.51)	85.41
4	2.19 (1.90~2.47)	87.60
5	1.43 (1.24~1.61)	89.03
6	1.15 (1.00~1.29)	90.18

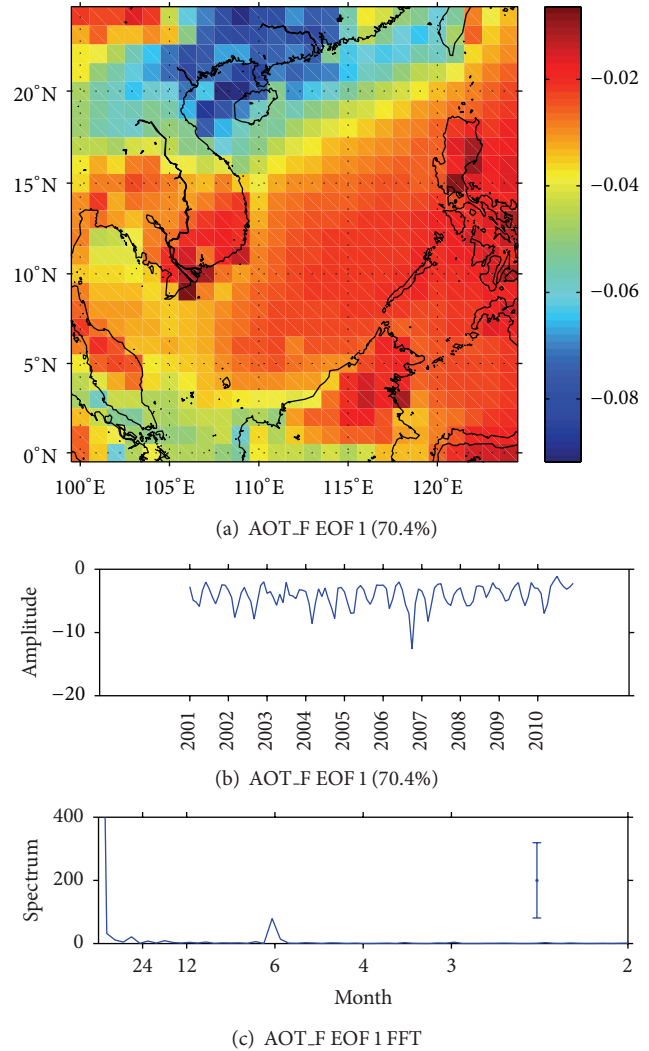


FIGURE 5: (a) The spatial distribution, (b) its corresponding time-varying amplitude for the vector EOF analysis mode 1 of the AOT_F in SCS during 2001/1–2010/12, and (c) the spectrum of (b) with FFT. The line segment represents the 95% confidence interval.

EOF1 of AOT_F shows that the largest variation area is in southern China, followed by Sumatra and Borneo in Indonesia (Figure 5(a)). The temporal amplitudes show two larger time phases from March to April and from August to October (Figure 5(b)). Meanwhile, the high-value fine aerosol particles were observed both at Aeronet observatories

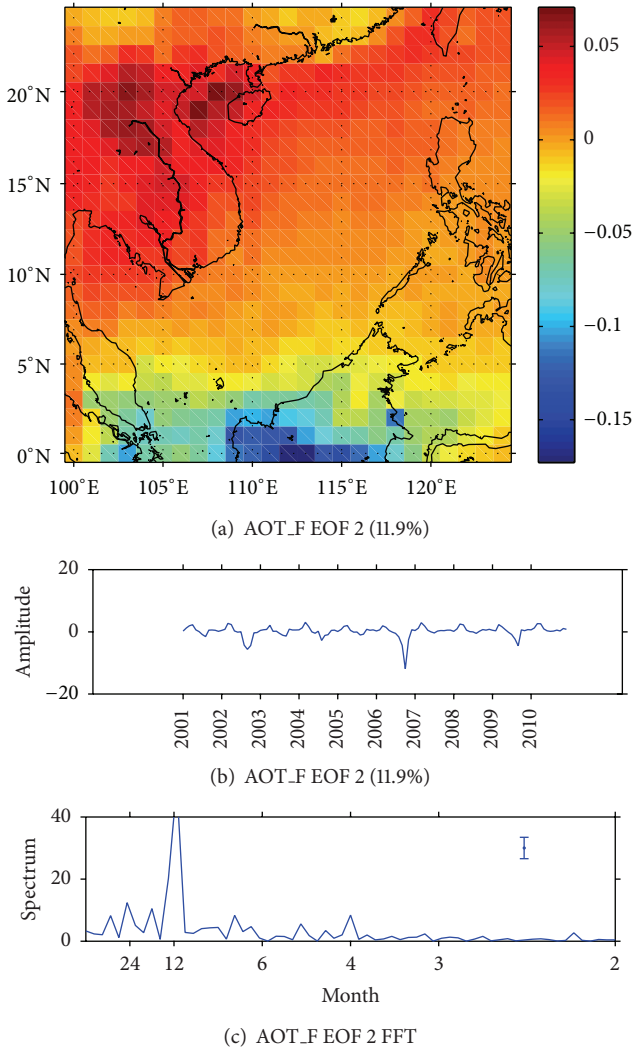


FIGURE 6: The same as Figure 5 but EOF mode 2 of AOT.F.

of Hong Kong and Bac Lieu. The two peaks appear every year probably due to the time different biomass burnings of these two regions.

Figure 6(a) shows the spatial distribution of EOF2 of AOT.F. The positive variation is in the Indochina Peninsula, while it is negative in Borneo. From the time series of amplitude (Figure 6(b)), the positive amplitude appears from November to next May, but the negative value is found during June and September. Therefore, the higher value of AOT.F is found in the Indochina Peninsula during March and April, and it also appears in Borneo and Sumatra during August and October. Two larger temporal amplitudes showed in October 2006 and September 2009. During these two months, the high value of fine aerosol particles was also found at the observatories of Hong Kong, Thailand, Dongsha, and Singapore. The spectrum analysis shows that the variation is an annual cycle which indicates that the fine aerosol particles are occurring in the abovementioned areas every year.

Figure 7(a) shows the spatial distribution of EOF3 of AOT.F. Positive values are in the Indochina Peninsula,

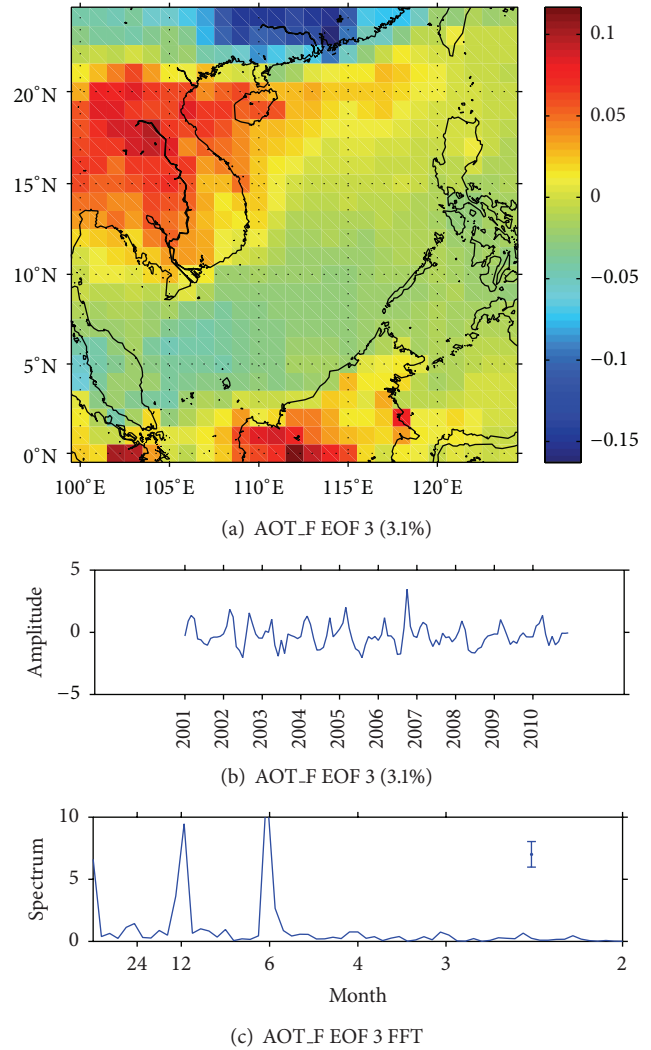


FIGURE 7: The same as Figure 5 but EOF mode 3 of AOT.F.

the Luzon Strait, and Borneo, but negative values are only found in China. Combining the time series of amplitude (Figure 7(b)) indicates that more AOT.F are found in the Indochina and Borneo from February to April and in China from May to August. The amplitude distribution also shows that the maximum positive amplitude is larger during El Niño period. Figure 7(c) shows the significant peak at annual cycle and semiannual cycle. It corresponds to the results of Lu et al. [16].

Previous results indicate that the higher AOT.F corresponds to the biomass burning around the SCS from March to April and from August to October [5, 6], which are similar to the result of this study. Moreover, the AOT is also affected by El Niño and La Niña events. Figure 8 shows the average AOT.C and AOT.F over the SCS during the normal, El Niño, and La Niña periods. The average AOT.C is smaller in El Niño period. On the contrary, the average AOT.F is larger in the El Niño events. Because during El Niño periods, the trade winds reverse direction, blowing from west to east (Asia towards Peru), the source of coarse particle (AOT.C) blown

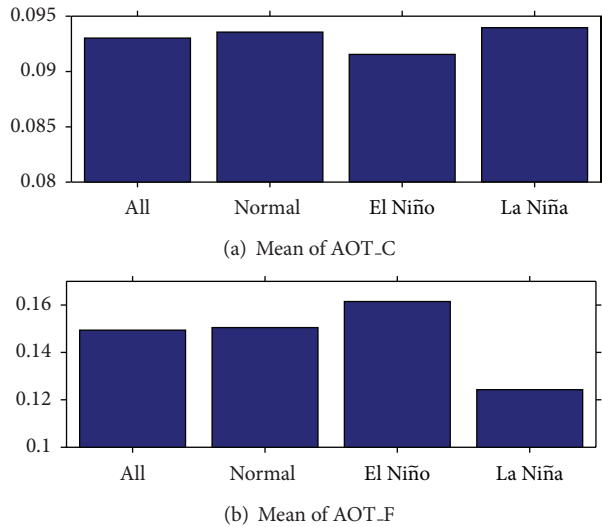


FIGURE 8: The average AOT over the SCS, (a) coarse mode aerosol, and (b) fine mode aerosol.

from the sea surface may be reduced, and the source of fine particle (AOT_F) generated by the biomass burning from the Indochina Peninsula may be increased.

4. Conclusions

In this study, we use coarse mode AOD and fine mode AOD derived from Terra MODIS at 550 nm from December 2001 to December 2010 to discuss the variation of coarse aerosol (e.g., dust or ocean spray) and fine mode aerosol (e.g., biomass burning or anthropogenic pollution) over the SCS. The variation of AOT_C is in high agreement with the measured coarse aerosol particles of Aeronet observatory. The high-value AOT_C occurs in spring. According to the spatial distribution and the results of this study, China and the Indochina Peninsula are the probable source regions of coarse aerosol particles. Besides, the temporal amplitudes of AOT_C modes show that the average amplitude during the La Niña period is larger.

The significant EOF modes of AOT_F indicate that the high value occurs annually and semiannually. The spatial distribution of each mode and other studies also evidence that the biomass burning, respectively, occurs in the Indochina Peninsula during March and April but occurs from August to October in Sumatra and Borneo. Besides, the results also show that the average amplitude of AOT_F is larger during the El Niño period. It can be concluded that the change of wind direction in the tropical area during the El Niño period may change the distribution of aerosols.

Conflict of Interests

The authors declare no conflict of interests.

Acknowledgments

The authors thank Shin-Jie Ho for processing satellite data. This work was supported by the National Science Council of Taiwan under Grants NSC 102-2611-M-019-016 and MOST 103-2611-M-019-006. The MODIS AOD data were from NASA/GSFC LAADS Web: <http://ladswb.nascom.nasa.gov/data/search.html>. The Aeronet data were obtained from NASA/GSFC Aerosol Robotic Network through website at <http://aeronet.gsfc.nasa.gov>. The Oceanic Niño Index was from NOAA National Weather Service Climate Prediction Center website at http://www.cpc.ncep.noaa.gov/products/analysis_monitoring/ensostuff/ensoyears.shtml.

References

- [1] K.-M. Lau and M. T. Li, "The monsoon of East Asia and its global associations—a Survey," *Bulletin of the American Meteorological Society*, vol. 65, no. 2, pp. 114–125, 1984.
- [2] C.-R. Ho, Q. Zheng, Y. S. Soong, N.-J. Kuo, and J.-H. Hu, "Seasonal variability of sea surface height in the South China Sea observed with TOPEX/Poseidon altimeter data," *Journal of Geophysical Research: Oceans*, vol. 105, no. 6, Article ID 2000JC900001, pp. 13981–13990, 2000.
- [3] C.-R. Ho, N.-J. Kuo, Q. Zheng, and Y. S. Soong, "Dynamically active areas in the South China Sea detected from TOPEX/POSEIDON satellite altimeter data," *Remote Sensing of Environment*, vol. 71, no. 3, pp. 320–328, 2000.
- [4] N.-J. Kuo, Q. Zheng, and C.-R. Ho, "Response of Vietnam coastal upwelling to the 1997-1998 ENSO event observed by multisensor data," *Remote Sensing of Environment*, vol. 89, no. 1, pp. 106–115, 2004.
- [5] I.-I. Lin, J.-P. Chen, G. T. F. Wong, C.-W. Huang, and C.-C. Lien, "Aerosol input to the South China Sea: results from the moderate resolution imaging spectro-radiometer, the quick scatterometer, and the measurements of pollution in the troposphere sensor," *Deep-Sea Research Part II: Topical Studies in Oceanography*, vol. 54, no. 14-15, pp. 1589–1601, 2007.
- [6] T. Holloway, H. Levy II, and G. Carmichael, "Transfer of reactive nitrogen in Asia: development and evaluation of a source-receptor model," *Atmospheric Environment*, vol. 36, no. 26, pp. 4251–4264, 2002.
- [7] S.-C. Tsay, G. Liu, N. Y. Hsu, and W. Sun, "Outbreaks of Asian dust storms: an overview from satellite and surface perspectives," in *Recent Progress in Atmospheric Sciences: Applications to the Asia Pacific Region*, K. N. Liou and M.-D. Chou, Eds., pp. 373–401, World Scientific Publishing, 2009.
- [8] J. Zhao, F. Zhang, Y. Xu et al., "Chemical characteristics of particulate matter during a heavy dust episode in a coastal city, Xiamen, 2010," *Aerosol and Air Quality Research*, vol. 11, no. 3, pp. 300–309, 2011.
- [9] T.-H. Lin, N. C. Hsu, S.-C. Tsay, and S.-J. Huang, "Asian dust weather categorization with satellite and surface observations," *International Journal of Remote Sensing*, vol. 32, no. 1, pp. 153–170, 2011.
- [10] S.-H. Wang, S.-C. Tsay, N.-H. Lin et al., "First detailed observations of long-range transported dust over the northern South China Sea," *Atmospheric Environment*, vol. 45, no. 27, pp. 4804–4808, 2011.
- [11] J. S. Reid, E. J. Hyer, R. S. Johnson et al., "Observing and understanding the Southeast Asian aerosol system by remote

- sensing: an initial review and analysis for the Seven Southeast Asian Studies (7SEAS) program,” *Atmospheric Research*, vol. 122, pp. 403–468, 2013.
- [12] N.-H. Lin, S.-C. Tsay, H. B. Maring et al., “An overview of regional experiments on biomass burning aerosols and related pollutants in Southeast Asia: from BASE-ASIA and the Dongsha Experiment to 7-SEAS,” *Atmospheric Environment*, vol. 78, pp. 1–19, 2013.
- [13] S. A. Atwood, J. S. Reid, S. M. Kreidenweis et al., “Analysis of source regions for smoke events in Singapore for the 2009 El Nino burning season,” *Atmospheric Environment*, vol. 78, pp. 219–230, 2013.
- [14] J. Wang, C. Ge, Z. Yang et al., “Mesoscale modeling of smoke transport over the Southeast Asian Maritime Continent: Interplay of sea breeze, trade wind, typhoon, and topography,” *Atmospheric Research*, vol. 122, pp. 486–503, 2013.
- [15] G. R. North, T. L. Bell, R. F. Cahalan, and F. J. Moeng, “Sampling error in the estimation of empirical orthogonal function,” *Monthly Weather Review*, vol. 110, no. 7, pp. 699–706, 1982.
- [16] K.-W. Lu, J.-Y. Hu, and X.-Y. Yang, “Spatial patterns in seasonal variability of sea surface wind over the South China Sea and its adjacent ocean,” *Journal of Tropical Oceanography*, vol. 31, pp. 41–47, 2012.

Research Article

Impacts of Two-Type ENSO on Rainfall over Taiwan

Chen-Chih Lin, Yi-Jiun Liou, and Shih-Jen Huang

Department of Marine Environmental Informatics, National Taiwan Ocean University, Keelung 20224, Taiwan

Correspondence should be addressed to Chen-Chih Lin; mikania.lin@gmail.com

Received 14 October 2014; Revised 13 January 2015; Accepted 13 January 2015

Academic Editor: Yuri Kuleshov

Copyright © 2015 Chen-Chih Lin et al. This is an open access article distributed under the Creative Commons Attribution License, which permits unrestricted use, distribution, and reproduction in any medium, provided the original work is properly cited.

Impacts of two-type ENSO (El Niño/Southern Oscillation), canonical ENSO and ENSO Modoki, on rainfall over Taiwan are investigated by the monthly mean rainfall data accessed from Taiwan Central Weather Bureau. The periods of the two-type ENSO are distinguished by Niño 3.4 index and ENSO Modoki index (EMI). The rainfall data in variously geographical regions are analyzed with the values of Niño 3.4 and EMI by correlation method. Results show that the seasonal rainfalls over Taiwan are different depending on the effects of two-type ENSO. In canonical El Niño episode, the rainfall increases in winter and spring while it reduces in summer and autumn. On the contrary, the rainfall increases in summer and autumn but reduces in winter and spring in El Niño Modoki episode. Nevertheless, two types of La Niña cause similar effects on the rainfall over Taiwan. It increases in autumn only. The rainfall variations in different types of ENSO are mainly caused by the monsoon and topography.

1. Introduction

El Niño and La Niña events are the phenomenon of inter-annual scale interactions between atmosphere and ocean [1]. During El Niño episodes, lower than normal pressure is over the eastern tropical Pacific and higher than normal pressure is over Indonesia and northern Australia. The air-pressure oscillation swings between east and west getting associated with the weaker than normal near-surface equatorial easterly winds. The normal patterns of tropical precipitation and atmospheric circulation become disrupted. The abnormally warm waters rise up and aggregate cloudiness to cause rainfall in the eastern and equatorial central Pacific [2, 3]. Meanwhile, rainfall has diminished over Indonesia, Malaysia, and northern Australia. Sometimes a totally reversed phenomenon can be observed after El Niño episode, that is, La Niña episode. The phenomenon caused by the atmospheric pressure oscillation between the east and west tropical South Pacific is called El Niño/Southern Oscillation (ENSO) [4].

Recent studies have shown the distinct warming and cooling patterns different from those of canonical El Niño events. A warm anomaly arises in the central Pacific whereas cold anomalies are on both flanks of the basin. The new phenomenon is of interest to the climate community which is called El Niño Modoki [5, 6]. It is also known as central Pacific

El Niño [7] or warm pool El Niño [8]. La Niña Modoki is named as colder central Pacific is flanked by warmer eastern and western Pacific [9]. Both phenomena are referred to as ENSO Modoki. Compared to canonical ENSO, ENSO Modoki has become more prominent in recent times, thereby changing the teleconnection pattern arising from the tropical Pacific [10]. The occurrences of anomalous warm water may cause changes in air pressure, precipitation, and wind field [7, 11, 12]. The generation mechanism may significantly be affected by atmospheric forcing rather than by basin-wide thermocline variations [8, 13].

In response to rainfall variation, ENSO episodes have been detected in numerous studies. Trenberth and Caron [14] described the decrease of rainfall over the northeast coast of Brazil but increase over the southern Brazil and the Indian Ocean. During the mature period of El Niño, the anticyclone runs over the East Asia and enhances the rainfall in southern China [15]. Weng et al. [16] pointed out that El Niño Modoki and its climate impacts are very different from those of canonical El Niño. During the El Niño Modoki episode, a wet region is in the central Pacific where it is dry during the El Niño episode. An El Niño Modoki may also cause a shorter and more intense Australian monsoon precipitation [17]. Cai and Cowan [18] demonstrated that the La Niña Modoki is effective in causing an autumn rainfall increase

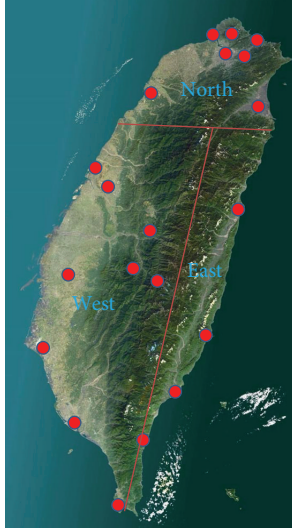


FIGURE 1: Points indicate the rain stations over Taiwan used in this study. The study area is separated into 3 regions: north, west, and east.

over northwestern Australia rather than over the east as in a canonical La Niña because convection shifts westward. Feng and Li [19] also mentioned that the precipitation increases in spring over the southern China during the canonical El Niño, while it decreases during the El Niño Modoki. A similar feature is also found in southwest America. The precipitation increases in autumn during the canonical El Niño, but it decreases during the El Niño Modoki [20]. The canonical ENSO and ENSO Modoki may affect the rainfall in the Pacific but also telecommunicate to other areas. Somehow, the effects of two-type ENSO on rainfall over Taiwan are not clearly analyzed. Thus, it is necessary to document systematically how they affect Taiwan.

2. Materials and Methods

Taiwan is a subtropical island located in the latitudes between 22°N and 26°N to the southeast of China. The Central Mountain Range with an average elevation of 2000 m runs from the north to the south and separates east and west to two different ecoregions. Yen and Chen [21] pointed out that the rainfall over Taiwan is mainly dominated by the seasonal monsoon, northeasterly in winter and southwesterly in summer, as well as modified by the local topography. To study the effect of ENSO on rainfall over Taiwan, we accessed the data from the Data Bank for Atmospheric Research, Taiwan Typhoon and Flood Research Institute, collected by Taiwan Central Weather Bureau. The rainfall data span from 1980 to 2011 at 20 stations in Taiwan as shown in Figure 1 has been employed in this study. Because the topography is very complicated in Taiwan, the weather stations distribute from 5 m elevation to over than 3000 m. Therefore, rainfall amount is localized. To avoid the local effect, we grouped the weather stations and then divided them into six subareas according to the terrain of Taiwan. The subareas include north, west, and east regions. Each region is further separated into plain

and mountain. Because there is no rain station on the eastern mountain subarea that we have a total of five subareas for this study. Table 1 presents the rain stations in each subarea.

Since the rainfall over Taiwan is mostly affected by monsoon, we ignore the regular season division of four seasons: spring from March to May, summer from June to August, autumn from September to November, and winter from December to February in most previous studies [5, 18, 19, 22, 23]. Instead, we consider monsoon gradually increases from November to December, while stands in January and February. Therefore, we divide the rainy periods with bimonthly as spring rain from March to April, Meiyu from May to June, summer rain from July to August, autumn rain from September to October, early winter rain from November to December, and winter rain from January to February. This division of rainy season is similar to Wang et al. [24] classifying the whole year to five periods: spring rain period (March and April), Meiyu period (May and June), summer rain period (July, August, and September), autumn rain period (October and November), and winter rain period (December, January, and February). Here, we consider the rainy season classified in more detail. In data process, the rainfall data in each station is subtracted by its mean value from 1980 to 2011, as anomaly data. A 3-month running mean filter is then applied to remove high frequent variability.

To distinguish the years of El Niño, La Niña, El Niño Modoki, and La Niña Modoki, the Niño 3.4 index and the El Niño Modoki index (EMI) are applied to this study. A 3-month running mean of sea surface temperature anomaly (SSTA) at the region of 5°S–5°N, 170°W–120°W has been characterized as the Niño 3.4 index. The EMI is the combination of area average of SSTA at regions A (10°S–10°N, 165°E–140°W), B (15°S–5°N, 110°W–70°W), and C (10°S–20°N, 125°E–145°E), respectively, as shown in Figure 2 and is defined as [5]

$$EMI = [SSTA]_A - 0.5 \times [SSTA]_B - 0.5 \times [SSTA]_C. \quad (1)$$

The value of Niño 3.4 larger than or equal to 0.45 is considered as the canonical El Niño episode, while the value smaller than or equal to -0.45 is considered as the canonical La Niña episode. The same value is applied to EMI. The EMI value larger than or equal to 0.45 is considered as the El Niño Modoki, while smaller than or equal to -0.45 is considered as the La Niña Modoki. We compute the correlation coefficient between rainfall anomaly and both ENSO indices. The positive correlation coefficient means rainfall increasing associates with positive ENSO indices (i.e., El Niño event), or the decreasing rainfall associates with negative ENSO indices (i.e., La Niña event). On the contrary, the negative correlation coefficient means rainfall decreasing associates with positive ENSO indices, or rainfall increasing associates with negative ENSO indices.

3. Results and Discussion

3.1. Influences during Canonical El Niño Episode. Figure 4 shows correlation coefficients between rainfall anomaly and Niño 3.4 at five subareas in different rainy periods. In spring

TABLE I: Information of rain stations in this study.

Subarea	Station name	Height above sea level (m)	Latitude	Longitude	
North	Plain	Tamsui	19.0	121°26'24" E	25°09'56" N
		Taipei	5.3	121°30'24" E	25°02'23" N
		Keelung	26.7	121°43'56" E	25°08'05" N
		Yilan	7.2	121°44'53" E	24°45'56" N
	Mountain	Hsinchu	26.9	121°00'22" E	24°49'48" N
		Anbu	825.8	121°31'12" E	25°11'11" N
		Zhuzihu	607.1	121°32'11" E	25°09'54" N
West	Plain	Tainan	40.8	120°12'17" E	22°59'36" N
		Hengchun	22.1	120°44'17" E	22°00'20" N
		Kaohsiung	2.3	120°18'29" E	22°34'04" N
		Chiayi	26.9	120°25'28" E	23°29'52" N
		Taichung	84.1	120°40'33" E	24°08'51" N
	Mountain	Wuqi	31.73	120°30'54" E	24°15'31" N
		Sun Moon Lake	1017.5	120°54'29" E	23°52'53" N
		Yushan	3844.8	120°57'06" E	23°29'21" N
East	Plain	Alishan	2413.4	120°48'18" E	23°30'37" N
		Dawu	8.1	120°53'44" E	22°21'27" N
		Chenggong	33.5	121°21'55" E	23°05'57" N
		Hualien	16.0	121°36'18" E	23°58'37" N
		Taitung	9.0	121°08'48" E	22°45'15" N

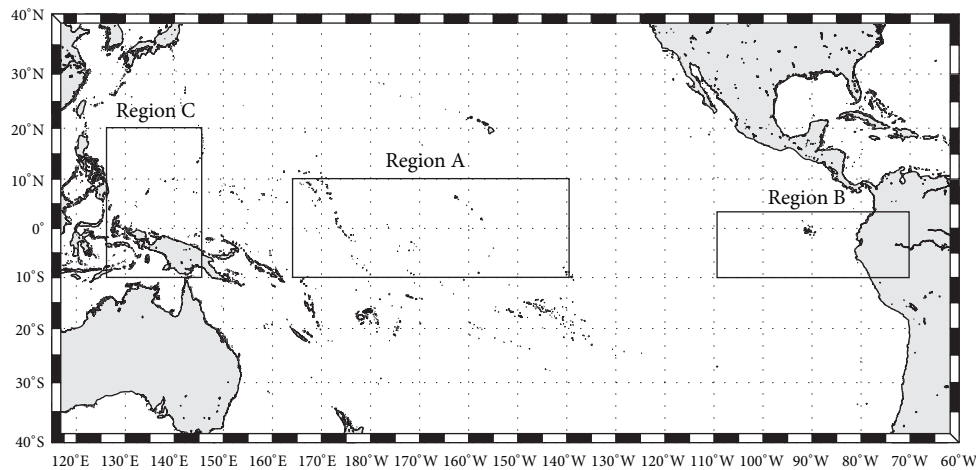


FIGURE 2: The regions for the definition of EMI.

rain period, one can see that correlation coefficients at all subareas are positive and higher than 0.7 during the canonical El Niño episode. Furthermore, the maximum correlation coefficient can be reached to 0.91 at western mountain subarea. The result is similar to that of Feng and Li [19] that the canonical El Niño enhances spring rainfall in Taiwan area.

Meiyu period, mostly cloudy to rainy, happens in May and June in Taiwan. The equilibrium strength forms a stationary front between the continental cold air mass and the Pacific warm air mass in southern China, Taiwan, and the Okinawa region. Low pressure disturbances often take place in these areas and bring abundant rainfall in Taiwan. In Figure 3, one

can see that correlation coefficients at all subareas are positive and higher than 0.5. We consider the effects of Taiwan topography on this convective line intercept rainfall and enhance subsequent rainfall at western mountain subarea.

For summer rain period, the correlation coefficients are not significant at all subareas except for the eastern plain with the correlation coefficient of -0.62 . Since the summer rain in Taiwan is mainly affected by southwesterly monsoon and typhoon, the leeward side of monsoon, eastern plain, apparently has less rainfall related to the Niño 3.4 index. Less typhoon attacks Taiwan in El Niño episode also need to be considered.

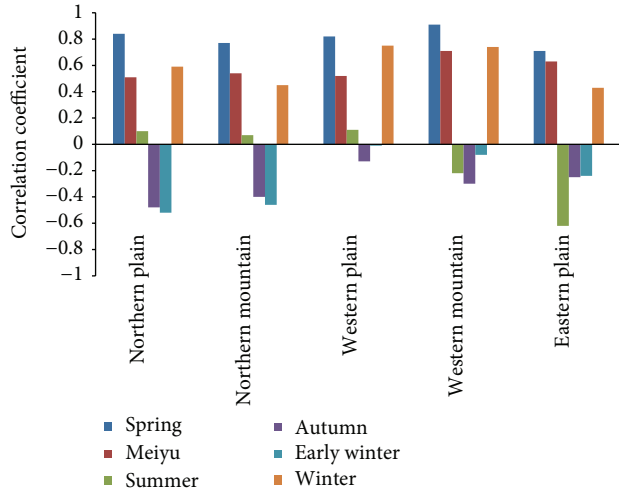


FIGURE 3: Correlation coefficients between rainfall anomaly and Niño 3.4 at five subareas during canonical El Niño episode.

In general, autumn climate resembles the early winter in northern Taiwan. During autumn and early winter, the rainfall is negative correlation with the intensity of El Niño at all subareas. However, only north area is significant where the correlation coefficient is -0.48 at plain subarea and -0.40 at mountain subarea in autumn rain period as well as -0.52 and -0.46 at plain and mountain subareas, respectively, in early winter rain period. The negative correlation coefficient displayed the negative relation between El Niño 3.4 index and rainfall anomaly. The intensity of El Niño enhances but rainfall diminishes more than others. Zhang et al. [25] noted the formation of time and location of the anticyclone near the Philippine Sea may affect the autumn rainfall over South China. The concept has the same idea by coincidence as Wang et al. [26] proposed that the canonical El Niño event may weaken the winter monsoon in East Asia, which responds to the graph shown in the early winter.

As shown in Figure 3, the winter rain period has positive correlation coefficients between rainfall anomaly and Niño 3.4 index at all subareas, especially in west region. At the moment, west region has been less affected by monsoon but more by the convergent cyclone. The correlation coefficient of 0.74 in the western plain during the El Niño episode displays the influence of El Niño starts from winter and then matures in the coming spring and summer.

To further explain possible processes of changing the rainfall, the wind field anomaly over the western Pacific associated with canonical El Niño is shown in Figure 4 which is sketched based on Figure 9 in Feng and Li [19]. During the canonical El Niño episodes, the warming sea surface water in the eastern Pacific results in asymmetric cyclonic anomalies on both sides of equator, with strong equatorial westerly anomalies. The southwesterly strengthens the moist transport to Taiwan from the South China Sea (SCS) and enhances the rainfalls in winter, spring, and Meiyu periods.

3.2. Influences during El Niño Modoki Episode. Figure 5 demonstrates correlation coefficients between rainfall anomaly and EMI at five subareas at six rain periods. Different

from the canonical El Niño, El Niño Modoki is associated with strong anomalous warming in the central tropical Pacific and cooling in the eastern and western tropical Pacific. Associated with this distinct warming and cooling patterns, the teleconnections are very different from the canonical El Niño episode.

At the formation of El Niño Modoki, the Walker Circulation runs over the tropical Pacific and converges in East Asia. The relative cold sea surface temperature produces higher air pressure, and down-welling air produces sunny and less rainfall.

The influences of El Niño Modoki on rainfall in early winter and winter are similar to that in spring. In winter and spring periods, the negative correlation coefficients of rainfall anomaly and EMI index display the results of dry periods by the maximum correlation coefficient of -0.67 at western plain subarea.

For Meiyu, summer, and autumn rain periods, all correlation coefficients are positive and significant (higher than 0.5) except for the eastern plain. The results indicate that Meiyu, summer, and autumn rainfall increase in most of Taiwan during El Niño Modoki episodes, which happens to agree completely with the interpretation of C. Wang and X. Wang [23] that strong southwesterly caused by the anticyclone near the Philippine Sea brings entrained water vapor and enhances the rainfall in Taiwan during El Niño Modoki episodes.

Figure 6 is sketched based on Figure 9 in Feng and Li [19] showing the anomalous wind pattern over the western Pacific associated with El Niño Modoki. The northeasterly reduces moist transportation to Taiwan from SCS, resulting in suppressed rainfall from early winter to spring.

3.3. Influences during Canonical La Niña Episode. La Niña episode is characterized by anomalous cool water in the central-west equatorial Pacific with the negative Niño 3.4 index. It changes the intensity and distribution of rainfall, the patterns of sea level pressure and atmosphere circulation. La Niña episode displays considerable event-to-event variability and the overall effects tend to be less predictable than those for El Niño episodes.

In Figure 7, one can find that the rainfall over Taiwan is affected less obviously by La Niña episodes. Owing to the fact that the correlation coefficient displays the relations between rainfall anomaly and Niño 3.4 index, the positive index indicates less rainfall; however, the negative indicates more rainfall. The rainfall effects by La Niña seem not obvious, except for the summer rain period at northern mountain and autumn rain period at north and east regions. Less summer rainfall at northern mountain subarea is in response to the colder sea surface temperature and less typhoon which brings the major rainfall in Taiwan. Apparently, the summer rainfall brought by typhoon decreases in the windward side at northern mountain subarea; likewise, the rainfall increases in autumn with the coming of stronger northeast monsoon at north and east regions.

3.4. Influences during La Niña Modoki Episode. During La Niña Modoki episode, a cold anomaly arises in the central Pacific flanked by warmer anomalies on both sides of the

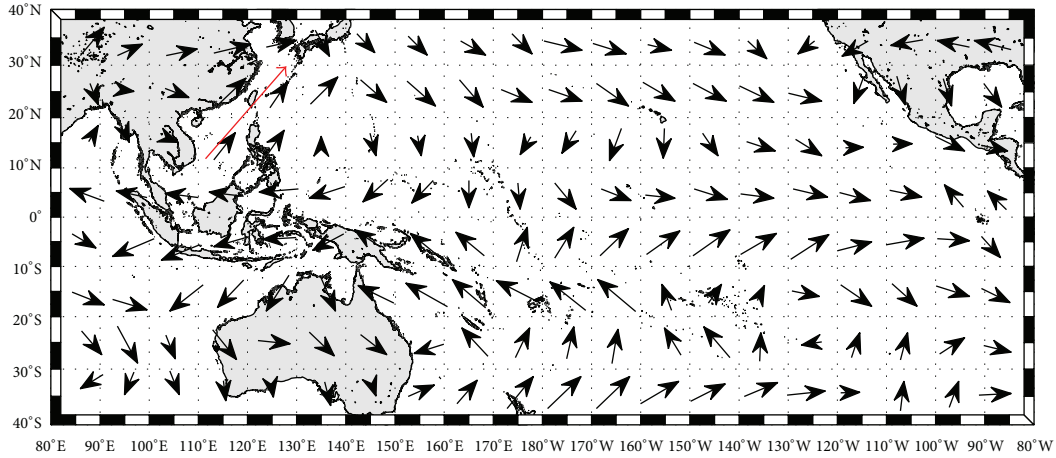


FIGURE 4: Anomalous patterns of wind vector over the Western Pacific during canonical El Niño episodes. The red arrow indicates the wind direction near Taiwan (sketched based on Feng and Li [19]).

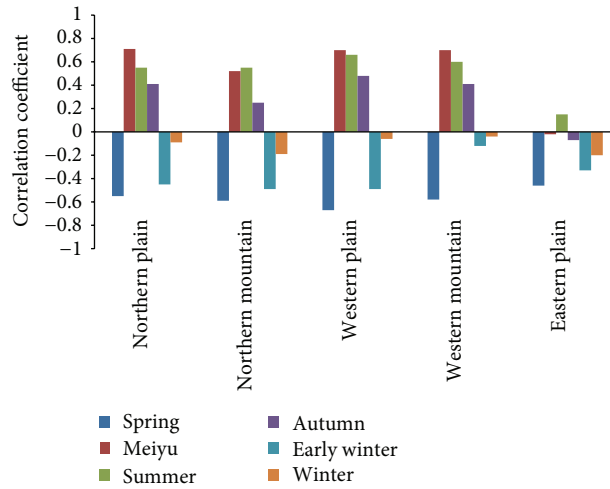


FIGURE 5: Correlation coefficients between rainfall anomaly and EMI at five subareas during El Niño Modoki episode.

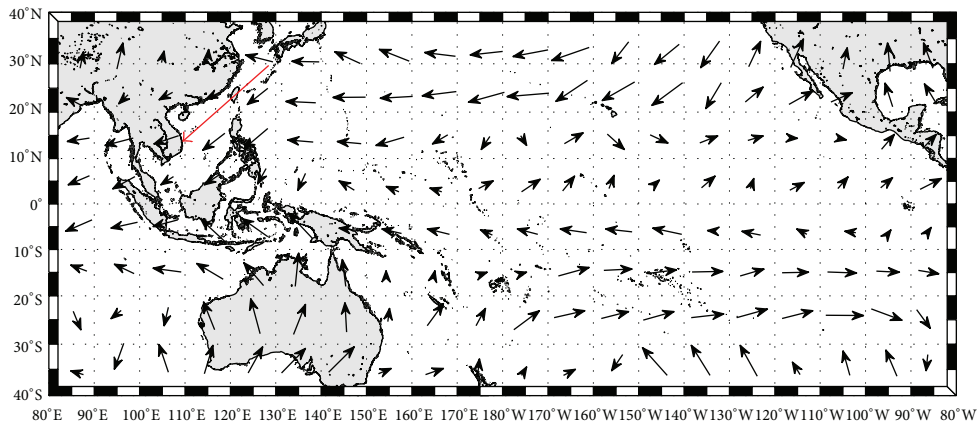


FIGURE 6: Anomalous patterns of wind vector over the Western Pacific during El Niño Modoki episode. The red arrow indicates the wind direction near Taiwan (sketched based on Feng and Li [19]).

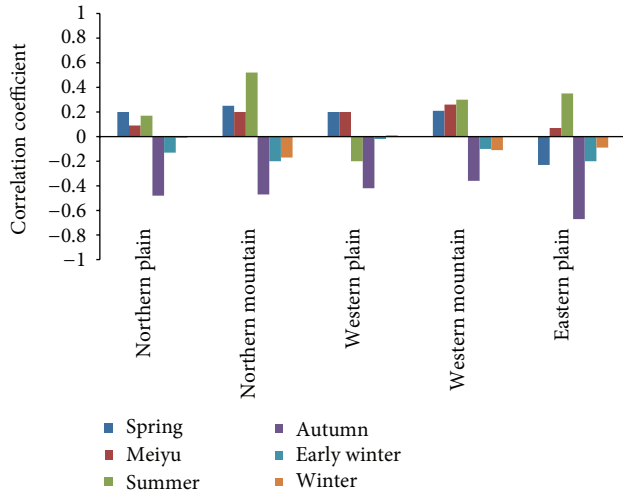


FIGURE 7: Correlation coefficients between rainfall anomaly and Niño 3.4 at five subareas during canonical La Niña episode.

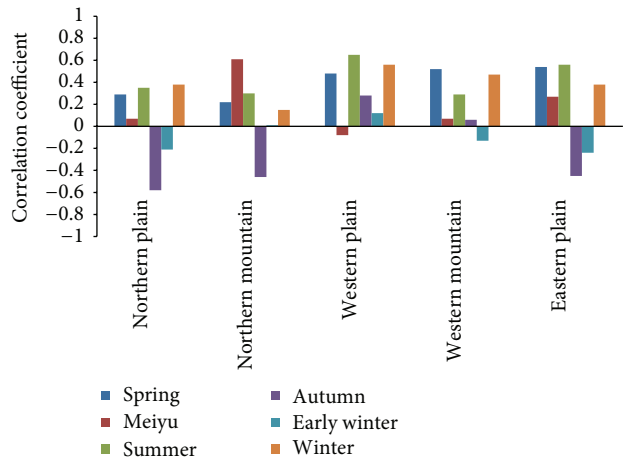


FIGURE 8: Correlation coefficients between rainfall anomaly and EMI at five subareas during La Niña Modoki episode.

basin. The air rises up in both sides of Pacific and sinks in the middle of Pacific, which makes the East Asia locates in a more rainfall condition. However, it is not the case shown in Taiwan.

In Figure 8, the positive correlation coefficient (higher than 0.5) suggests that the rainfall decreases significantly in spring at west and east Taiwan during La Niña Modoki episodes. A similar phenomenon can be also found in summer rain especially at western plain and eastern plain subareas.

For Meiyu period, obvious relationship is only at northern mountain with the correlation coefficient of 0.61. Positive correlation coefficient means Meiyu decreasing during La Niña Modoki. In autumn rain period, significant negative correlation coefficients point out the rainfall increases at north and east regions, which are possibly influenced by the windward side of monsoon.

The rainfall during La Niña Modoki episode mostly looks descending. This is possibly affected by the shift of

Intertropical Convergent Zone (ITCZ). Previous studies have documented that the rainfall in equatorial regions depends on the presence of the ITCZ. A small variation in the position of the ITCZ can have a major effect on rainfall in certain regions [27, 28]. Dai and Wigley [29] used empirical orthogonal function analysis and showed patterns of ENSO induced precipitation. From the amplitude of principal component of precipitation in their study, one can find that there is no big change in both canonical La Niña and La Niña Modoki episodes. Somehow, Yuan and Yan [30] indicated that the changes of sea surface temperature of the two types of La Niña are not obvious. Compared to both, the atmosphere is more active during La Niña Modoki than that in canonical La Niña, which makes the correlation coefficient display apparently.

4. Conclusions

This study focuses on the influences of rainfall over Taiwan during two-type ENSO episodes. The rainfall data at 20 stations in Taiwan from 1980 to 2011 are used in this study. According to the geomorphology of Taiwan, we divide the study area into north, west, and east regions and further separate each region into plain and mountain subareas. The rainfall periods are separated by bimonthly and are defined as spring rain period (March and April), Meiyu period (May and June), summer rain period (July and August), autumn rain period (September and October), early winter rain period (November and December), and winter rain period (January and February). We also apply Niño 3.4 index and EMI to differentiate between canonical ENSO and ENSO Modoki episodes. The different patterns of rainfall distribution are associated with differences in regional sea surface temperature anomalies, regional circulation, and the patterns of ascending or descending air associated with Walker circulation over this region.

The major findings in this study are summarized as follows.

- (1) The rainfall increases in Taiwan in northeast monsoon and Meiyu seasons during the canonical El Niño and the almost opposite feature occurs during the El Niño Modoki but its influence is less than that in canonical El Niño.
- (2) The influence of canonical La Niña on rainfall is not obvious in Taiwan, except for autumn when the rainfall increases. A similar phenomenon is found during La Niña Modoki.
- (3) The impacts of canonical La Niña and ENSO Modoki enhance rainfall obviously in autumn, while the impacts of ENSO Modoki dominate the rainfall in summer period.
- (4) Relative to the two-type ENSO, canonical El Niño event affects rainfall over Taiwan predominately.

Conflict of Interests

The authors declare that there is no conflict of interests regarding the publication of this paper.

Acknowledgments

The authors are grateful to the Data Bank For Atmospheric Project, Taiwan Typhoon and Flood Research Institute, National Applied Research Laboratories for the support of atmospheric research data. This work is partly supported by the Ministry of Science and Technology of Taiwan through grant MOST 103-2611-M019-006.

References

- [1] S. G. H. Philander, "El Niño and La Niña," *Journal of the Atmospheric Sciences*, vol. 42, no. 23, pp. 2652–2662, 1985.
- [2] C. F. Ropelewski and M. S. Halpert, "Precipitation patterns associated with the high index phase of the Southern Oscillation," *Journal of Climate*, vol. 2, no. 3, pp. 268–284, 1989.
- [3] M. S. Halpert and C. F. Ropelewski, "Surface temperature patterns associated with the Southern Oscillation," *Journal of Climate*, vol. 5, no. 6, pp. 577–593, 1992.
- [4] S. G. H. Philander, "El Niño southern oscillation phenomena," *Nature*, vol. 302, no. 5906, pp. 295–301, 1983.
- [5] K. Ashok, S. K. Behera, S. A. Rao, H. Weng, and T. Yamagata, "El Niño Modoki and its possible teleconnection," *Journal of Geophysical Research C: Oceans*, vol. 112, no. 11, Article ID C11007, 2007.
- [6] K. Ashok and T. Yamagata, "Climate change: the El Niño with a difference," *Nature*, vol. 461, no. 7263, pp. 481–484, 2009.
- [7] J.-S. Kug, F.-F. Jin, and S.-I. An, "Two types of El Niño events: cold tongue El Niño and warm pool El Niño," *Journal of Climate*, vol. 22, no. 6, pp. 1499–1515, 2009.
- [8] H.-Y. Kao and J.-Y. Yu, "Contrasting eastern-pacific and central-pacific types of ENSO," *Journal of Climate*, vol. 22, no. 3, pp. 615–632, 2009.
- [9] T. Shinoda, H. E. Hurlbert, and E. J. Metzger, "Anomalous tropical ocean circulation associated with La Niña Modoki," *Journal of Geophysical Research C: Oceans*, vol. 116, Article ID C12001, 2011.
- [10] M. Roxy, N. Patil, K. Aparna, and K. Ashok, "Revisiting the Indian summer monsoon—ENSO links in the IPCC AR4 projections: a cautionary outlook," *Global and Planetary Change*, vol. 104, pp. 51–60, 2013.
- [11] J. V. Ratnam, S. K. Behera, Y. Masumoto, K. Takahashi, and T. Yamagata, "Anomalous climatic conditions associated with the El Niño Modoki during boreal winter of 2009," *Climate Dynamics*, vol. 39, no. 1-2, pp. 227–238, 2012.
- [12] S.-W. Yeh, J.-S. Kug, B. Dewitte, M.-H. Kwon, B. P. Kirtman, and F.-F. Jin, "El Niño in a changing climate," *Nature*, vol. 461, p. 515, 2009.
- [13] J.-Y. Yu and H.-Y. Kao, "Decadal changes of ENSO persistence barrier in SST and ocean heat content indices: 1958–2001," *Journal of Geophysical Research D: Atmospheres*, vol. 112, no. 13, Article ID D13106, 2007.
- [14] K. E. Trenberth and J. M. Caron, "The southern oscillation revisited: sea level pressures, surface temperatures, and precipitation," *Journal of Climate*, vol. 13, no. 24, pp. 4358–4365, 2000.
- [15] R. Zhang and A. Sumi, "Moisture circulation over East Asia during El Niño episode in northern winter, spring and autumn," *Journal of the Meteorological Society of Japan*, vol. 80, no. 2, pp. 213–227, 2002.
- [16] H. Weng, K. Ashok, S. K. Behera, S. A. Rao, and T. Yamagata, "Impacts of recent El Niño Modoki on dry/wet conditions in the Pacific rim during boreal summer," *Climate Dynamics*, vol. 29, no. 2-3, pp. 113–129, 2007.
- [17] A. S. Taschetto, C. C. Ummenhofer, A. S. Gupta, and M. H. England, "Effect of anomalous warming in the central Pacific on the Australian monsoon," *Geophysical Research Letters*, vol. 36, no. 12, Article ID L12704, 2009.
- [18] W. Cai and T. Cowan, "La Niña Modoki impacts Australia autumn rainfall variability," *Geophysical Research Letters*, vol. 36, no. 12, Article ID L12805, 2009.
- [19] J. Feng and J. Li, "Influence of El Niño Modoki on spring rainfall over south China," *Journal of Geophysical Research D: Atmospheres*, vol. 116, no. 13, Article ID D13102, 2011.
- [20] W. Zhang, F.-F. Jin, J. Li, H.-L. Ren, and J.-X. Zhao, "Differences in teleconnection over the North Pacific and rainfall shift over the USA associated with two types of El Niño during boreal autumn," *Journal of the Meteorological Society of Japan*, vol. 90, no. 4, pp. 535–552, 2012.
- [21] M.-C. Yen and T.-C. Chen, "Seasonal variation of the rainfall over Taiwan," *International Journal of Climatology*, vol. 20, no. 7, pp. 803–809, 2000.
- [22] J. Feng, W. Chen, C.-Y. Tam, and W. Zhou, "Different impacts of El Niño and El Niño Modoki on China rainfall in the decaying phases," *International Journal of Climatology*, vol. 31, no. 14, pp. 2091–2101, 2011.
- [23] C. Wang and X. Wang, "El Niño modoki I and II by different impacts on rainfall in southern China and typhoon tracks," *Journal of Climate*, vol. 26, no. 4, pp. 1322–1338, 2013.
- [24] C. H. Wang, L. A. Li, and W. C. Liu, "Some characteristics of the precipitation in Taiwan," in *Biodiversity and Terrestrial Ecosystem*, C. I. Peng and C. H. Chou, Eds., Academia Sinica Monograph Series no. 14, pp. 343–354, Institute of Botany, 1994.
- [25] W. Zhang, F.-F. Jin, J. Li, and H.-L. Ren, "Contrasting impacts of two-type El Niño over the western North Pacific during boreal autumn," *Journal of the Meteorological Society of Japan*, vol. 89, no. 5, pp. 563–569, 2011.
- [26] B. Wang, R. Wu, and X. Fu, "Pacific-East Asian teleconnection: how does ENSO affect East Asian climate?" *Journal of Climate*, vol. 13, no. 9, pp. 1517–1536, 2000.
- [27] Q. Zheng, X.-H. Yan, W. T. Liu, W. Tang, and D. Kurz, "Seasonal and interannual variability of atmospheric convergence zones in the tropical Pacific observed with ERS-1 scatterometer," *Geophysical Research Letters*, vol. 24, no. 3, pp. 261–263, 1997.
- [28] T. Schneider, T. Bischoff, and G. H. Haug, "Migrations and dynamics of the intertropical convergence zone," *Nature*, vol. 513, no. 7516, pp. 45–53, 2014.
- [29] A. Dai and T. M. L. Wigley, "Global patterns of ENSO-induced precipitation," *Geophysical Research Letters*, vol. 27, no. 9, pp. 1283–1286, 2000.
- [30] Y. Yuan and H. M. Yan, "Different types of La Niña events and different responses of the tropical atmosphere," *Chinese Science Bulletin*, vol. 58, no. 3, pp. 406–415, 2013.